University of Mississippi

eGrove

Electronic Theses and Dissertations | Graduate School

1-1-2021

SEARCH FOR CPT AND LORENTZ INVARIANCE VIOLATION IN THE MUON g-2 EXPERIMENT AT FERMILAB

Meghna Bhattacharya
University of Mississippi

Follow this and additional works at: https://egrove.olemiss.edu/etd

 Part of the Physics Commons

Recommended Citation

Bhattacharya, Meghna, "SEARCH FOR CPT AND LORENTZ INVARIANCE VIOLATION IN THE MUON g-2 EXPERIMENT AT FERMILAB" (2021). *Electronic Theses and Dissertations*. 1987.
https://egrove.olemiss.edu/etd/1987

This Dissertation is brought to you for free and open access by the Graduate School at eGrove. It has been accepted for inclusion in Electronic Theses and Dissertations by an authorized administrator of eGrove. For more information, please contact egrove@olemiss.edu.

SEARCH FOR CPT AND LORENTZ INVARIANCE VIOLATION IN THE MUON $g-2$ EXPERIMENT AT FERMILAB

A Dissertation
presented in partial fulfillment of requirements
for the degree of Doctor of Philosophy
in the The Department of Physics and Astronomy,
The University of Mississippi

by

Meghna Bhattacharya

May 2021

Copyright Meghna Bhattacharya 2021
ALL RIGHTS RESERVED

ABSTRACT

The Muon g-2 experiment at Fermilab (E989) aims to measure the anomalous magnetic moment of the muon, $a_\mu = (g-2)/2$, to a groundbreaking precision of 140 ppb, obtaining a near four-fold increase in precision over the previous experiment, E821, at the Brookhaven National Laboratory (BNL). The value of a_μ from BNL currently differs from the Standard Model prediction by ~ 3.7 standard deviations, suggesting the potential for new physics and therefore, motivating a new experiment.Because the theory predicts this number with high precision, testing the g-factor through experiment provides a stringent test of the SM and can suggest physics beyond the Standard Model. The goal of the Fermilab Muon $g-2$ experiment is to increase the statistical precision by more than a factor of 20 and reduce systematic errors by a factor of 3. By measuring anomalous muon precession rate (ω_a) in an external magnetic field, the anomalous magnetic moment will be calculated. This is an incredibly challenging experiment with a unique opportunity to provide new insight into nature.

The $g-2$ data also provides a great opportunity for setting the most stringent limits on some of the Standard Model Extension CPT Lorentz violating (LV) parameters in the muon sector. One of the CPT and Lorentz violating signatures that we can look for using $g-2$ data is a sidereal variation of $\omega_a(t)$. Extensive simulation studies confirm that the sensitivity regarding the sidereal varation roughly scales with ω_a uncertainty. Hence, the $g-2$ experiment at FNAL should be able to reach limits of $\sim 5 \times 10^{-25}$ GeV. Because the CPT and LV analyses are essentially studies of variations in ω_a as a function of time and charge, performing an ω_a analysis sets the stage for the CPT and LV measurement. This dissertation focuses on the methodology of a fully functioning framework and analyzing the Fermilab Muon $g-2$ Run 2 data containing ~ 11 billion events above an energy threshold of 1.7 GeV.

DEDICATION

I dedicate this work to my parents Sangeeta and Pallav, and my younger brother Mainak for your unconditional love and support. I love you.

LIST OF ABBREVIATIONS AND SYMBOLS

FNAL	Fermi National Accelerator Laboratory
BNL	Brookhaven National Laboratory
LV	Lorentz Violation
CPT	Charge, Parity and Time revarsal
LS	Lomb-Scargle
MPF	Multi-parameter fit
EQS	Electrostatic quadrupole system
C.L.	Confidence level

ACKNOWLEDGMENTS

First and foremost, I would like to thank my mentor and advisor Prof. Breese Quinn. It would not have been possible without his continuous support, motivation and encouragement in whatever I chose to participate. Thank you Breese for giving me this unique opportunity to be based at Fermilab and for always being there with me through the ups and downs. I would like to thank my other committee members and readers of this dissertation Kevin Beach, Lucien Cremaldi and Nathan Hammer. Much thanks to Lucien Cremaldi, Luca Bombelli, Kevin Beach, Rob Kroeger and Alakabha Datta for their endless support from the department. I literally grew up watching Hogan Nguyen taking care of the experiment and tackling very challenging situations and I will always cherish that. Thank you Hogan for all your encouragement over these years. Hogan's advice on my 27th birthday - don't lose your sense of humor as you grow old. I would like to thank Brendan Casey and Chris Polly for their support and continuous encouragement. Thank you Brendan Caesy and Adam Lyon for sharing your valuable experience with me and help me finish the journey. I could have never thought of having such an amazing group of peers -fun and passionate - I would like to thank Sudeshna Ganguly, Simon Corrodi, Jason Crncovic, Manolis Kargiantulakis, Esra Yucel Barlas, Suvarna Ramachandran, Jimin George, Tammy Walton for being my family in the past years. Thank you Wanwei Wu for helping me getting up to speed when I first joined the experiment. Much thanks to Kevin Labe for all his inputs on the CPT and Lorentz violation analysis. Many thanks to Simon Corrodi for providing one of key ingredients of the analysis.

People without whom I am incomplete and can not thank enough are my family and my backbone, my parents Sangeeta and Pallav and my younger brother Mainak. Friends who became family these past years and kept me going through the thick and thin, thank you for keeping the spirit high and young always Biswaranjan Behera, Dripta Bhattacharjee, Amrita Ghosh Chatterjee, lil Ishaan

Chatterjee, Sudeshna Ganguly, Simon Corrodi and Animesh Chatterjee.

I would like to thank Fermi National Accelerator Laboratory (Fermilab), and U. S. Department of Energy, Office of Science, HEP User Facility for the resources provided. Fermilab is managed by Fermi Research Alliance, LLC (FRA), acting under Contract No. DE-AC02-07CH11359. The work described in this dissertation was supported by the U.S. Department of Energy.

TABLE OF CONTENTS

ABSTRACT ii

DEDICATION iii

LIST OF ABBREVIATIONS AND SYMBOLS iv

ACKNOWLEDGMENTS v

LIST OF FIGURES xi

LIST OF APPENDICES xxii

CHAPTER 1: INTRODUCTION 1

1.1 Anomalous Magnetic Moments of Particles 1

1.2 Standard Model Predictions of a_μ 2

1.2.1 QED Contribution 2

1.2.2 Electroweak Contribution 3

1.2.3 Hadronic Contribution 4

1.2.4 The Standard Model Prediction 7

1.3 The Long Standing Discrepancy 8

1.4 Hints of Physics Beyond Standard Model 10

1.5 CPT and Lorentz Violation Tests 11

1.5.1 CPT and Lorentz Violation Experimental Signatures 12

CHAPTER 2: 14

2.1 Measurement of a_μ . . . 14
2.2 Muon Beam Production and Journey to the Muon Campus . . . 15
2.3 Muon Beam Injection . . . 17
2.4 Muon Beam Storage and Focusing . . . 18
2.5 Measuring the Magnetic Field . . . 21
2.6 Muon Beam Dynamics . . . 25
2.6.1 Coherent Betatron Oscillation . . . 26
2.6.2 Beam Debunching . . . 27
2.7 The Detectors . . . 28
2.7.1 Auxiliary Detectors . . . 28
2.7.2 Calorimeter Detectors . . . 29
2.8 Measuring ω_a . . . 30
2.8.1 Systematic Effects . . . 35
2.8.2 Electric Filed and Pitch Correction . . . 37
2.8.3 The error budget . . . 38

CHAPTER 3: Measurement of ω_a . . . 40
3.1 Energy and Time Spectra . . . 40
3.2 Pileup Construction . . . 41
3.3 The Five Parameter Fit . . . 48
3.4 Fit Algorithm . . . 48

CHAPTER 4: CPT and Lorentz Violation(LV) Tests . . . 52
4.1 R_μ Instead of ω_a . . . 52
4.2 Ingredients for The Sidereal Search . . . 53

4.3 Time: One of the Key Ingredients . . . 54
4.3.1 The Sidereal Time . . . 56
4.4 Data Selection Criteria . . . 56
4.5 Analysis Techniques . . . 57
4.6 Run-by-Run Data Analysis . . . 59
4.6.1 Lomb Scargle Test . . . 59
4.6.2 Sensitivity of the algorithm . . . 64
4.6.3 Multi Parameter Fit Results . . . 71
4.6.4 Expressing Lomb Power in terms of an Amplitude of Oscillation 72
4.6.5 Summary of the Run-by-Run results . . . 73
4.7 Folded Data Analysis . . . 78
4.7.1 Analysis for Window A . . . 78
4.7.2 Lomb Scargle Test on Folded Data With Window A . . . 79
4.7.3 Multi-parameter Fit on Folded Data with Window A . . . 80
4.7.4 Analyzing Five Different Windows . . . 81
4.7.5 Summary of the Folded Analysis . . . 83
4.8 Summary: Run-by-Run and Folded Data Analysis . . . 85
4.9 Systematic Concerns . . . 87
4.9.1 Benchmarking The Analysis . . . 92
4.10 Conclusion . . . 95

CHAPTER 5: Future Prospect . . . 97
5.1 $g-2$ Operations . . . 97
5.2 Muon $g-2$ Experiment - Here to Where? . . . 99

LIST OF REFERENCES 101

APPENDICES 106

A.1 Upgrades of the EQS in Summer Shutdown 2018 107

A.2 RF Systems Installation and Testing for Reduction of ω_a Systematic Effects 109

B.1 Spectral Analysis Techniques 116

B.2 Lomb-Scargle Test 118

B.2.1 Statistical Properties 118

B.2.2 Independent Frequencies 120

VITA 121

LIST OF FIGURES

1.1 Feynman diagrams for Dirac contribution and Schwinger term respectively representing QED contributions to a_l 3

1.2 Electroweak contributions to a_μ from virtual exchange of Z^0, W bosons and Higgs boson 4

1.3 Hadronic contributions to a_μ from the leading order HVP and HLbL interactions, the hadronic interactions represented by shaded circle above 6

1.4 The figure depicts all the different theoretical contributions to muon g-2 with experimental values for comparison.The value from each storage ring experiment is represented as a vertical line with the projected precision for E989 as a dashed line. The size and uncertainty of various SM corrections grouped by interaction type are depicted as bars extending onto the vertical axis, values taken from the latest white paper from the theory initiative. 7

1.5 A comparison between the various theoretical predictions and the BNL experimental measurements of a_μ 8

1.6 A comparison between the Theory Initiative recommended theoretical prediction and the BNL and Fermilab experimental measurements of a_μ. The experimental average is in tension with the SM prediction at the level of 4.2σ 9

2.1 The schematic of accelerator beam-line components Fermilab uses to provide spin-polarized muon beam to E989. Protons start in the Linac, travel around the Booster and then the Recycler Ring, hit the nickel-based target at AP0, and produce pions. The pions then decay to muons in the Delivery Ring before reaching the muon campus [42]. 16

2.2 The timing structure of the beam sent to the muon campus at Fermilab. Each cycle consists of 16 bunches–10 ms apart–with a repetition rate of 11.4 Hz. 16
2.3 The inflector magnet and its cross section view 18
2.4 A map of the vacuum chambers. K1-K3 show the locations of the kicker magnets, while Q1-Q4 show the locations of the electrostatic quadrupoles. Also shown is the location of the inflector 19
2.5 An illustration of production and injection of the muon beam into the storage ring. accelerated protons hit the Inconel target to produce charged pions which then decay to muons. These high energy muons are then injected into the storage ring through the inflector magnet. A "kick" is then applied by a kicker magnet to store the muons on the design storage orbit. 20
2.6 Figure shows 4 quadrupole plates within the storage region. The top and bottom plates are positively charged while the side plates are negatively charged to provide the vertical focusing for the positive muon beam. 21
2.7 A cross-section of the $g-2$ storage ring. Superconducting coils in yellow excites the main magnet. Top hats, pole pieces, wedges used for subppm level adjustment of the field 22
2.8 A sample FID signal. The pick up coil signals around the proton sample will oscillate as the spins precess around the external magnetic field, and decay as the spins relaxes back. 23
2.9 The position of the fixed NMR probes that monitor the field 24×7 are shown in the left figure. The fixed probes sit above and below the storage region. The trolley that contains 17 NMR probes is shown in the right figure. The trolley goes around the ring every 3 days to provide a detailed map of the magnetic field inside the ring. . . 24

2.10 An example of azimuthally average magnetic field map provided by the trolley in the storage ring. The (x) marks indicate the location of 17 NMR probes within the trolley 24
2.11 A schematic showing the position of the IBMS detectors 29
2.12 The calorimeter detector placed on the inside of the ring. The right figure shows the PbF_2 crystals within a calorimeter 31
2.13 μ^+ will decay through a W^+ boson to two neutrinos and a positron with a branching ratio of 99.98% 32
2.14 A typical wiggle plot from the calorimeter detectors in the Fermilab experiment showing number of detected positrons as a function of time above an energy threshold. The time spectrum is folded into a $100\mu s$ window 33
3.1 Method of pileup construction [**?**] 42
3.2 The original energy spectra and the pileup spectra for calorimeters 1, 12 and 24 . . 44
3.3 Energy spectra for detectors 1, 12 and 24 after pileup subtraction 45
3.4 The ratio of the original pulse and the pileup spectrum for detectors 1, 12 and 24 . . 46
3.5 The energy spectrum of the measured hits and that of the artificially constructed pileup events match very well, indicating good performance of the algorithm. The Pileup time spectrum on the right plot on a log scale is fit to an exponential decay function to verify that the lifetime of these events is half the muon lifetime of $64.4\mu s$. The bottom plot shows the ratio of the measured energy to the pileup energy, again confirming the performance of the algorithm. 47

3.6 Five parameter fit to one of the subsets of Run 2 data. Left plot shows the fit performed $\sim 30\mu s$ and the corresponding pulls of the fit residuals. The pull shows the case where a fit is performed with a start time extending to $10\mu s$, which shows that the current five parameter fit is insufficient to model the beam motion. The right plot shows a Fourier transform (FFT) of the fit residuals. The clear peaks present in the FFT are expected as we did not account for these motions in the fit function. . . 50

3.7 The left plot shows the fit parameter values when a five parameter fit was performed on 1 hour duration of data. The best-fit values of R for Run 2 are still blinded. The right plot shows a 13 parameter fit on a relatively larger subset of Run 2 data where some of the beam frequencies were modeled and hence extending the five parameters to Thirteen. 51

4.1 The schematic of the clock system used in the experiment [36]. 54

4.2 Figure shows the unix timestamps for each run in the Run 2 dataset after applying the data quality cuts. 55

4.3 Time series of ω_a, $\tilde{\omega}'_p$ and R_μ on a run by run basis respectively. 60

4.4 The spectral analysis plots on a run by run basis for Run 2 data. Left plot: the Lomb power, $P_N(\omega)$ over a frequency range shows that there is no significant peak present at the sidereal frequency. Right plot: the distribution of $P_N(\omega)$ over all the frequencies scanned follow an exponential decay confirming the absence of a potential significant oscillation signal 61

4.5 Figure shows spectral analysis plots on preliminary Run 2 data. The top plot shows spectral power as a function of frequencies when the analysis was performed on the full Run-2 dataset. The middle and the lower plot shows the spectral power as a function of frequencies when the analysis was performed on partial subsets of the data in order to investigate the overall structure of various peaks. 63

4.6 Comparison of Lomb power distributions. The left plot shows the Lomb power distribution for an input data with no significant signal. The right plot on the other hand shows the power distribution when we injected a 10 ppm false signal. The Lomb power distribution in the right plot extends to a much higher value, indicating the presence of a strong signal. 64

4.7 The Lomb-Scargle test performed on an ensemble of simulated data with no signal added. The distribution of the maximum Lomb power shows that the range of peak heights stretches out to 15 even when there is no signal present. The frequency positions of the highest peaks are randomly distributed confirming that the algorithm is not biased towards a particular frequency over the other within the search range. . 65

4.8 The Lomb-Scargle test performed on an ensemble of simulated data with 10 ppm signal added at the sidereal frequency. The distribution of the maximum Lomb power shows that the range of peak heights shifts to the right when there is a significant signal present as compared to the no signal scenario. The frequency positions of the highest peaks are no longer randomly distributed rather the distribution now peaks near the frequency of the input signal confirming that the algorithm is able to detect a significant signal 66

4.9 Performance of the Lomb-Scargle test. The left plot shows the power spectrum when we added two 4 ppm signals with the data point uncertainties δR_μ to the average of the data points, hence excluding some of the gaussian noise. The spectral power plot behaves as expected. The right plot shows the corresponding Lomb power distribution, which now deviates completely from an exponential decay, indicating a presence of pure oscillation components in the data. Note that the x-axis is truncated in this plot to emphasize the decay deviating quite a lot from that of an exponential nature. 68

4.10 Sensitivity of Lomb-Scargle test. Left plot: simulated data generated with individual data point uncertainty, and then two signals of amplitude 4 ppm are added simultaneously at the sidereal frequency and at $0.0012s^{-1}$. Right plot: simulated data generated with individual data point uncertainty as $\delta R_\mu/2$, with false signals of 4 ppm injected at the same frequencies as before. The right plot shows clear huge peaks at both the frequencies as the SNR improves quite a lot. We see that the sensitivity of the algorithm scales with the uncertainties on R_μ. The more statistics we accumulate as we move forward with the $g-2$ experiment the smaller the uncertainties on individual data points and hence the more sensitive the algorithm will be. 69

4.11 Lomb-Scargle test on simulated data generated with individual data point uncertainties set to $\delta R_\mu/2$, with two artificial signals added at the sidereal frequency and at a randomly chosen frequency of $0.0012s^{-1}$. The left plot shows the power spectrum when the false signal amplitudes are 2 ppm. The right plot shows the spectrum when two 1 ppm signals are added. The peak amplitudes are much more significant for the 2 ppm signals compared to the 1 ppm case. The peak from the signal injected at $0.0012s^{-1}$ is almost smeared by the noise in the right plot and the spectral leakage is much more prominent in this case. 70

4.12 Figure shows an oscillation period scan of the 2019 Run 2 data, where we step through A_0 in the fit keeping the rest of the parameters floating. Top plot: Oscillation amplitude A_0 from the MPF fit. Bottom plot: unnormalized χ^2 of the fit. Absence of a global minimum in the bottom plot indicates no signal. 71

4.13 Figure shows an oscillation period scan of the 2019 Run 2 data, where we step through A_0 in the fit keeping the rest of the parameters floating. Top plot: Oscillation amplitude A_0 from the MPF fit. Bottom plot: unnormalized χ^2 of the fit. Absence of a global minimum in the bottom plot indicates no signal. 73

4.14 Figure depicts the distribution of the amplitude of artificial signals added to simulated data resulting in the same Lomb power at the sidereal frequency as seen from Run 2 data. The artificial signal amplitude from the corresponding Lomb power comes out to be 0.68 ± 0.48 ppm which agrees quite well with the amplitude predicted by the multi-parameter fit results, 0.94 ± 0.63. 74

4.15 Distribution of Lomb power at the sidereal frequency for 10000 simulated data groups.The x-axis is the Lomb power at the sidereal frequency for each data group. We conclude from the above plots that the amplitude of oscillation in the real data is less than 2 ppm with 95% confidence level. 76
4.16 Distribution of the oscillation amplitudes at the sidereal frequency for 10000 simulated data groups are shown. The x-axis here is the oscillation amplitude, A_0 obtained from the multi-parameter fit. We conclude from the above plots that the amplitude of oscillation in the real data is less than 1.7 ppm with $\sim$ 95% confidence level. 77
4.17 The folded time series of R_μ for Run 2. The time window chosen here is four times the sidereal period. 79
4.18 The Lomb-Scargle power spectrm for folded time of window A. 80
4.19 The multi-parameter fit for folded time of window A. 80
4.20 Oscillation period scan for folded time of window A. 81
4.21 The Lomb-Scargle power spectrm for five different windows. 82
4.22 Oscillation period scans on data folded in window C and D respectively. The oscillation amplitude on the y-axis of the top plot actually is the fit parameter A in ppm. The y-axis of the bottom plot is the unnormalized χ^2 of the multi-parameter fit for each value of the oscillation period, T_0. The vertical line corresponds to the sidereal period. 84

4.23 Distribution of best-fit values of the fit parameter A_0, the oscillation amplitude on simulated folded data of window size A. The vertical line corresponds to the value of A_0 from real data. The bottom right plot shows that the amplitude of oscillation is bigger than that of the real data $\sim$ 94 % of the time when an artificial signal of amplitude 2 ppm is present. Hence, setting a limit of 2 ppm with confidence 94%. . 85

4.24 Distribution of the Lomb power at the sidereal frequency for simulated folded data of window size A. The vertical line corresponds to Lomb power obtained from real data. The bottom right plot shows that the Lomb power is bigger than that of the real data $\sim$ 93 % of the time when an artificial signal of amplitude 2 ppm is present. Hence, setting a limit of 2 ppm with confidence 93%. 86

4.25 The time series of the magnetic field measurements for Run 2. 88

4.26 Figure shows the spectral analysis performed on the field measurements. The top plot shows the spectral power as a function of frequencies within the search range along with a zoomed in version to focus on the peaks near the sidereal frequency. The middle and bottom plots show the spectral power analysis when only partial data were used for the analysis in order to investigate the presence of various peaks over the search range. 89

4.27 Figure shows an oscillation period scan of the 2019 Run 2 data, where we step through A_0 in the fit keeping the rest of the parameters floating. Top plot: Oscillation amplitude A_0 from the MPF fit. Bottom plot: unnormalized χ^2 of the fit. Absence of a global minimum in the bottom plot indicates no signal. 91

4.28 The time series of the magnetic field measurements for Run 2. 92

4.29 Figure shows the distribution of the widths of the highest peak for 1000 simulated data groups with two artificial signals of same amplitude added at the sidereal frequency and the solar day frequency, with 1 ppm to 4 ppm. There is a small shoulder that arises for higher amplitude signals. 93
4.30 Figure shows the distribution of the widths of the highest peak for 1000 simulated data groups with artificial signals of 1 ppm to 4 ppm injected at the sidereal frequency. 94
4.31 Figure shows the comparison of the distribution of the position of the highest peak for 1000 simulated data groups with artificial signals of 1 ppm to 4 ppm injected at the sidereal frequency and that at the solar day frequency. 95
5.1 The first figure shows a spark at the quadrupoles recorded by a camera. The second figure shows one of the mitigation strategies used in the 2018 summer shutdown. . . 98
A.1 The first figure shows small bends introduced in the shutdown period for mitigating the high spark rates. The second figure shows another mitigation strategy of adding ceramic plates, known as "batman" to reduce vibration of long leads. 108
A.2 The first figure shows the two kinds of high voltage resistors that were used. The HVR resistors were found to have a resistance of $2M\Omega$ whereas the requirement was $\sim 39k\Omega$. The second plot shows that the quad plates with the damaged HVR resistors take $\sim 100\mu s$ to reach full voltage and hence affects the ω_a data 109
A.3 The piezoelectric accelerometer was used to measure the quad plate vibrations. . . . 110
A.4 The laser setup used to measure the quad plate vibrations by capturing the reflected laser from a mirror attached to the quad plates by a photo diode. 111
A.5 Figure shows a schematic of the interface that is currently used between the RF electronics and the quadrupoles. 112
A.6 RF extension boxes once assembled at MC-1 113

A.7 Potted RF resistors that are now installed in all of the eight quadrupole systems . . . 114
A.8 Potted RF resistors after being installed in all of the eight quadrupole systems, the white cables connect the resistors to the transformers that are used to provide more power and hence more CBO reduction 115

LIST OF APPENDICES

A. Electrostatic Quadrupole Systems 107

B. Lomb-Scargle Method 116

CHAPTER 1

INTRODUCTION

1.1 Anomalous Magnetic Moments of Particles

When placed in an external magnetic field, a fermion's internal magnet tends to align with the external magnetic field. For fermions, the magnetic dipole moment ($\boldsymbol{\mu}$) is related to the spin ($\mathbf{S}$) by

$$\boldsymbol{\mu} = g\frac{Qe}{2m}\mathbf{S}, \tag{1.1}$$

where $Q = \pm 1$ and $e > 0$, m is the mass and g, the Lande-g factor is a proportionality constant characterizing the relation between the magnetic moment of the particle and the spin.

The torque on a particle in a magnetic field $\mathbf{B}$ is

$$\mathbf{N} = \boldsymbol{\mu} \times \mathbf{B} \tag{1.2}$$

hence the spin precession rate of the particle will depend on g, one of the key physics principles for the Fermilab experiment. One of the great successes of Dirac's relativistic theory was the prediction that $g = 2$ for spin-1/2 particles with no internal structure [1]. A derivation of this result can be found in [2]. However, in 1947, motivated by measurements of the hyperfine structure in hydrogen, Schwinger showed that from a theoretical viewpoint contributions to the electron spin magnetic moment arise from the lowest order radiative correction [3]. Eq. 1.1 therefore becomes

$$\boldsymbol{\mu} = 2(1 + a_l)\frac{Qe}{2m}\mathbf{S}, \qquad \text{where} \qquad a_l = \frac{g_l - 2}{2}, \tag{1.3}$$

The first term is the Dirac moment and the second term is the anomalous moment, where the dimensionless quantity a_l is often referred to as the anomalous magnetic moment. The anomalous

magnetic moment leads to the anomalous precession, ω_a of the muons, which is a measure of how fast the spin precesses in presence of an external magnetic field. This precession can be measured very precisely. Parallely, Kusch and Foley measured the electron g factor to be $g_e = 2.00238(10)$ [[4], [5]], supporting the need for introducing radiative corrections in a more complete theory. From a quantum field theory point of view, any interaction of a muon or electron with virtual particles will contribute to the g-factor. The value of a_l can be measured experimentally very precisely, and hence can be probed to test the theoretical predictions.

1.2 Standard Model Predictions of a_μ

The theoretical contributions to a_μ come from the QED, EW and Hadronic sectors:

$$a_\mu^{\mathrm{SM}} = a_\mu^{\mathrm{QED}} + a_\mu^{\mathrm{EW}} + a_\mu^{\mathrm{Had}} \tag{1.4}$$

where the QED contributions are from interactions involving virtual leptons and photons, EW contributions from interactions with the massive bosons and the Hadronic contributions from strongly interacting hadrons. The Muon $g-2$ Theory Initiative consists of over hundred theorists from various institutions working on a full re-evaluation of the SM prediction [6].

1.2.1 QED Contribution

The QED correction is well understood and the uncertainty on the correction is small. The contribution has been calculated to five-loops through analytical and numerical approaches. The famous one-loop contribution was calculated by Schwinger as shown in Fig. 1.1. The current QED contributions calculated by Aoyama et al. [7], [6], [8] is

$$\begin{aligned} a_\mu^{\mathrm{QED}} &= \sum_n^\infty C_n \left(\frac{\alpha}{2\pi}\right)^n \\ &= 11658471.8971(0.0007)(0.0017)(0.0006)(0.0072) \times 10^{-10} \end{aligned} \tag{1.5}$$

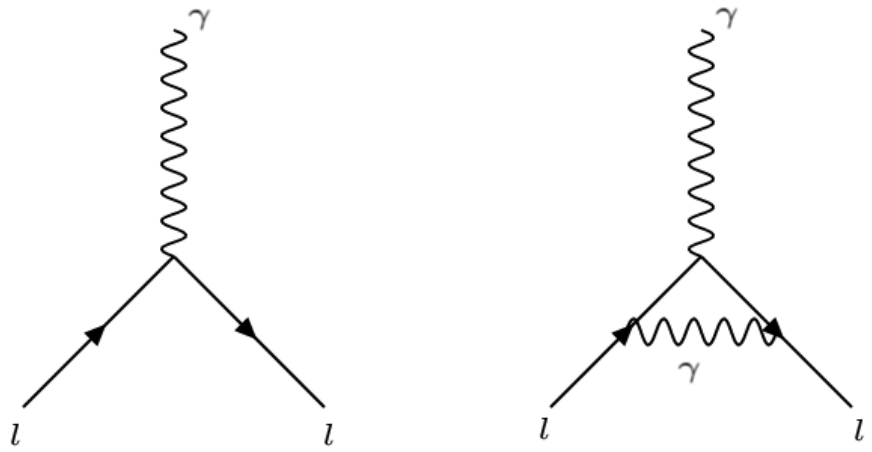


Figure 1.1: Feynman diagrams for Dirac contribution and Schwinger term respectively representing QED contributions to a_l

where the uncertainties arise from the lepton masses, the four-loop contributions, the five-loop contributions and the determination of α using measurements of ^{87}Rb , respectively. Although over 99% of the contribution to a_μ comes from the QED sector the error is much smaller than from the EW and hadronic contributions.

1.2.2 Electroweak Contribution

The EW contribution, shown in Fig. 1.2, is calculated through two-loops. The different one-loop diagrams are shown in Fig. 1.2. The total electroweak contribution, given by Ishikawa et al. [9] is

$$a_\mu^{\mathrm{EW}} = (15.36 \pm 0.10) \times 10^{-10} \tag{1.6}$$

The uncertainty from the EW is much smaller than the hadronic sector and comes from virtual exchange of $W^\pm$, Z^0 and H^0. The EW contributions to a_μ are much smaller than the QED contributions as the EW processes are suppressed by $(\frac{m_l}{m_{Z_0,H,W^\pm}})^2$, where the masses of the gauge bosons are much larger than that of the muon. EW contributions are much smaller when compared to the QED effects but the uncertainty on these contributions is not negligible if we consider the experimental accuracy.

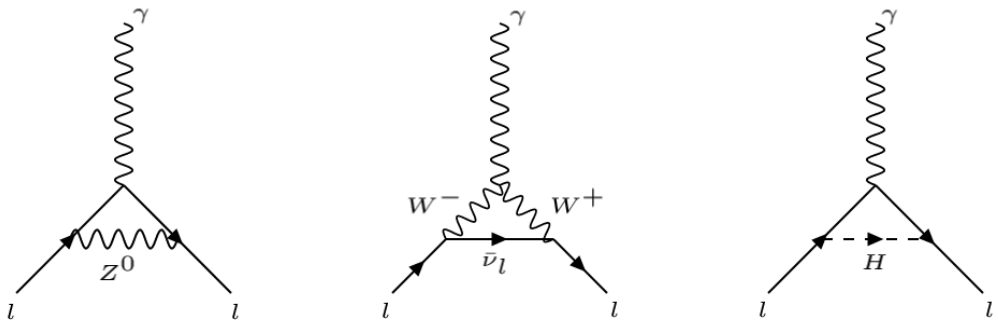


Figure 1.2: Electroweak contributions to a_μ from virtual exchange of Z^0, W bosons and Higgs boson

1.2.3 Hadronic Contribution

The hadronic contributions to a_μ come from interactions with virtual hadrons. The amplitudes for these processes can't be calculated using perturbative methods due to the large coupling at low energies. The uncertainty in the hadronic sector is dominated by the low energy non perturbative processes which then dominates the overall uncertainty in the SM calculation. The hadronic contributions consists of two major components, hadronic vacuum polarization (HVP) and hadronic light by light (HLbL) contribution:

$$a_\mu^{\text{had}} = a_\mu^{\text{HVP}} + a_\mu^{\text{HLbL}} \tag{1.7}$$

.

The goal of the Muon $g-2$ Theory Initiative is to make improvements in the hadronic calculations, and has a future prospect of a factor of 2 improvement in dispersive hadronic vacuum polarization (HVP) error. A lot of ongoing effort in the theoretical community is dedicated in determining the hadronic contributions.

Hadronic Vacuum Polarization:

In Eq. 1.7, a_μ^{HVP} stands for contributions from hadronic vacuum polarization and the first order diagrams are shown in Fig. 1.3. This can be calculated using two techniques. One of them is to express the virtual hadron bubble into the loop integrals for the photon propagator using a

dispersive approach [10], [11]. The cross section of the electron-positron annihilation can be used to estimate the imaginary part of the photon propagator [6],[8],[11]. This could be solved using a perturbative approach for a lepton bubble, instead a data driven approach is followed for a hadron bubble. The dispersion integral to the leading order (LO) can be expressed as [12]

$$a_\mu^{\mathrm{HVP(LO)}} = \frac{\alpha m_\mu}{3\pi} \int_{m_\pi^2}^{\infty} \frac{ds}{s^2} K(s) R(s) \tag{1.8}$$

where the kernel function, $K(s)$ can be calculated in terms of combinations of m_μ and $R(s)$ is the ratio of cross sections,

$$R(s) = \frac{\sigma(e^+e^- \rightarrow \text{hadrons})}{\sigma(e^+e^- \rightarrow \mu^+\mu^-)} \tag{1.9}$$

A brief overview of the cross-section measurements in different energy ranges for calculating eq 1.9 is discussed in Keshavarzi et al. [13], [14].

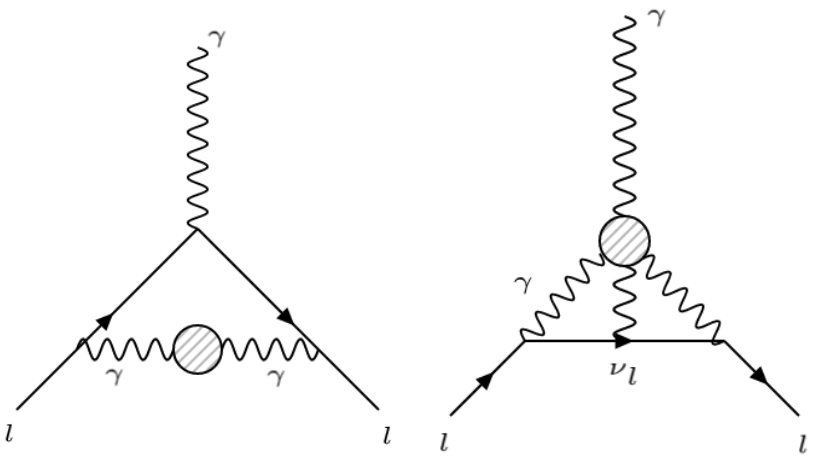
The cross-section data can be measured in two ways: operating at fixed center of mass energies in the collider experiment, initial state radiation tagging for the calculation of the differential cross-section while considering a wider range of energies. The uncertainty in the HVP sector can be reduced by acquiring more data and comparing different cross-section experiments. The number from Aoyama et al. as of November 2020 is

$$a_\mu^{\mathrm{HVP(LO)}} = 693.1(4.0)_{\mathrm{tot}} \times 10^{-10} \tag{1.10}$$

The other technique for calculating a_μ^{HVP} is to use lattice QCD for estimating the HVP contributions. The behavior from a continuous theory can be recovered in the limit of the ensemble being infinitely large and described over a very fine grid. The lattice caculation results are consistent with that from the dispersive approach with larger uncertainties [12].

Hadronic Light by Light Contributions

The other hadronic term, hadronic light-by-light contribution comes from four photon



(a) The leading order HVP Feynman diagram

(b) Light-by-light hadronic contributions

Figure 1.3: Hadronic contributions to a_μ from the leading order HVP and HLbL interactions, the hadronic interactions represented by shaded circle above

interaction and the diagrams are shown in Fig. 1.3. Because the evaluation of these diagrams are model dependent, there have been constant tension while calculating the contribution. The HLbL contribution to a_μ is [15], [16], [17]

$$a_\mu^{\text{HLbL}} = 10.5(2.6) \times 10^{-10} \tag{1.11}$$

There has been huge interest and efforts in evaluating the contribution using dispersive approach [18], [19], [20] and lattice QCD [21], [22]. The excellent agreement between phenomenology and lattice QCD leads to taking a weighted average for the final SM calculation [6].

$$a_\mu^{\text{HLbL}}(\text{phenomenology + latticeQCD}) = 9.0(1.7) \times 10^{-10} \tag{1.12}$$

The current errors in lattice calculation are too large to take a weighted average in a similar manner to the HVP sector, and future advancements in the calculation of HLbL are heavily dependent on further lattice QCD studies.

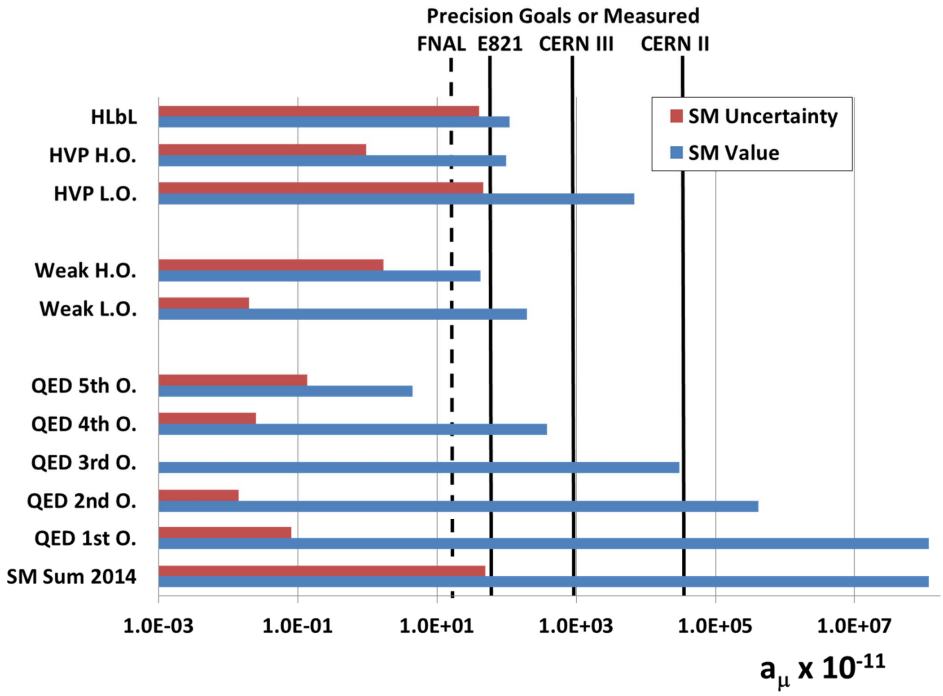


Figure 1.4: The figure depicts all the different theoretical contributions to muon g-2 with experimental values for comparison.The value from each storage ring experiment is represented as a vertical line with the projected precision for E989 as a dashed line. The size and uncertainty of various SM corrections grouped by interaction type are depicted as bars extending onto the vertical axis, values taken from the latest white paper from the theory initiative.

1.2.4 The Standard Model Prediction

The final SM contribution is expressed in terms of QED and EW contributions combined with the hadronic sector [6]

$$\begin{aligned} a_\mu^{\mathrm{SM}} &= a_\mu^{\mathrm{QED}} + a_\mu^{\mathrm{HVP,LO}} + a_\mu^{\mathrm{HVP,NLO}} + a_\mu^{\mathrm{HVP,NNLO}} + a_\mu^{\mathrm{HLbL,LO}} + a_\mu^{\mathrm{HLbL,NLO}} \\ &= 11659181(4.3) \times 10^{-10} \end{aligned} \tag{1.13}$$

This result has a relative uncertainty of 368 parts per billion (ppb). The theoretical predictions have been consistent over the years and the discrepancy between theory and experimental measurement is between 3σ and 4σ depending on the SM prediction considered while the current experimental measurements come from BNL and now Fermilab experiments. Fig. 1.5 shows the discrepancy

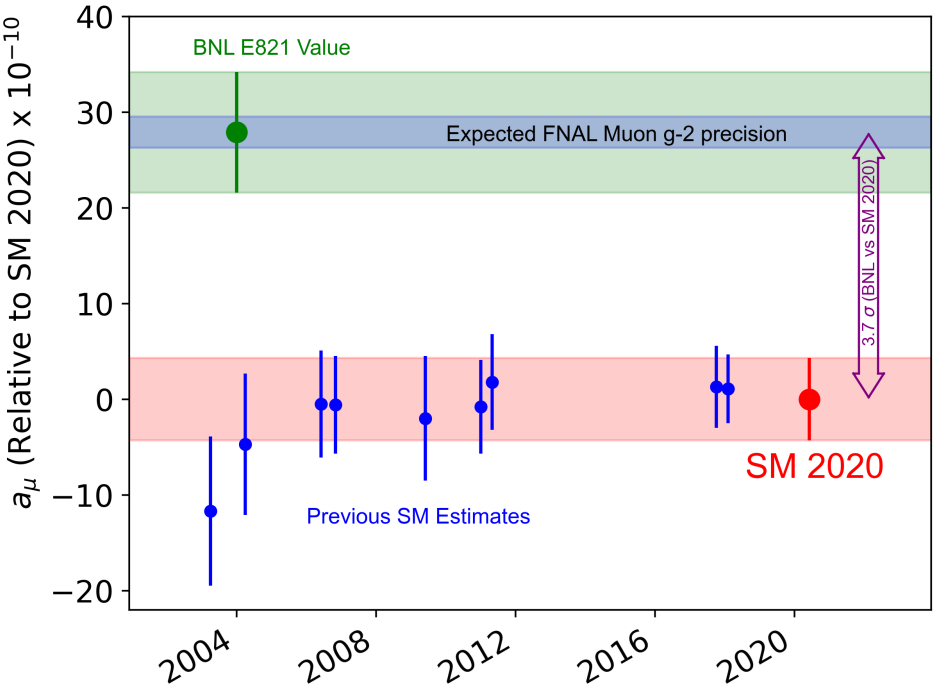


Figure 1.5: A comparison between the various theoretical predictions and the BNL experimental measurements of a_μ

between the SM prediction and the BNL experimental result. Fig.1.4 depicts all the different theoretical contributions to muon g-2 with experimental values for comparison. The most important point highlighted by the figure is that theory needs to improve in the hadronic light-by-light and hadronic vacuum polarization sectors.

1.3 The Long Standing Discrepancy

With improved methods and more statistics for the data driven approaches, the SM prediction of a_μ have improved and the latest number as of November 2020 is used here [6]. The experimental measurement of a_μ comes from the recent Fermilab Muon $g-2$ experiment. The Run-1 results of the Fermilab Muon g-2 experiment confirms the findings of the BNL Muon $g-2$ experiment. The Fermilab Muon $g-2$ experiment measured a_μ to be [23]

$$a_\mu^{\text{Exp}}(\text{FNAL}) = 116592040(54) \times 10^{-11} \tag{1.14}$$

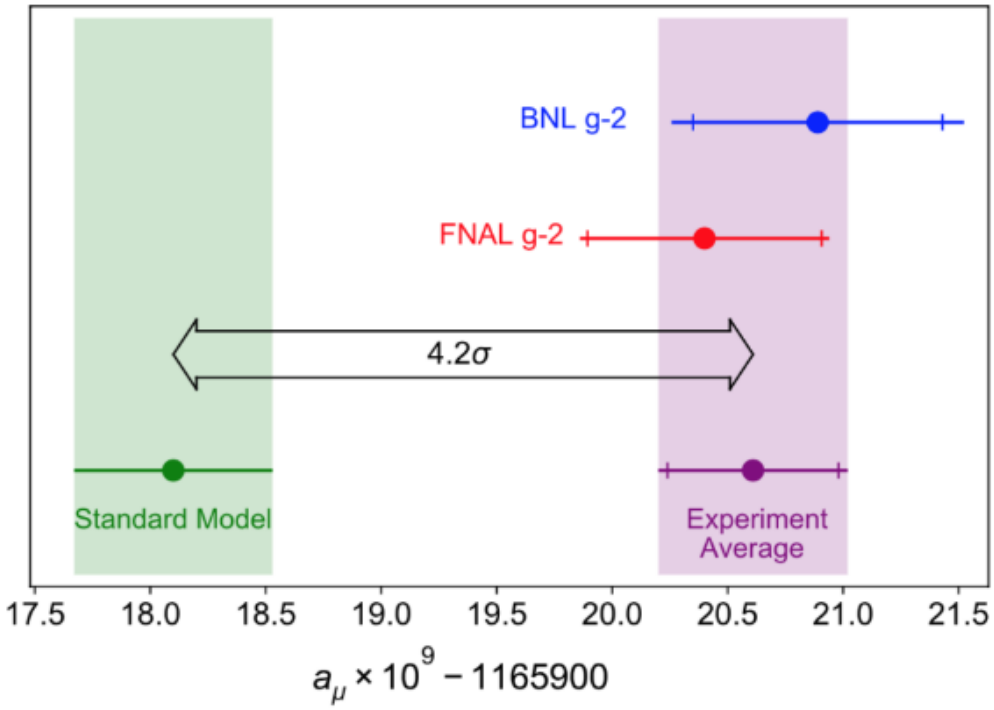


Figure 1.6: A comparison between the Theory Initiative recommended theoretical prediction and the BNL and Fermilab experimental measurements of a_μ. The experimental average is in tension with the SM prediction at the level of 4.2σ

which corresponds to a 460 ppb uncertainty. Fig. 1.6 depicts the current status of the SM prediction and the experimental measurement. The Fermilab experimental goal is to reduce the uncertainty on the measurement by a factor of 4. The SM prediction and the experimental measurement uncertainties are of the same order. The deviation of the experimental average value from the theoretical prediction is expressed

$$a_\mu^{\text{Exp}} - a_\mu^{\text{SM}} = 25.1(5.9) \times 10^{-10} \tag{1.15}$$

which corresponds to a 4.2 standard deviations.

1.4 Hints of Physics Beyond Standard Model

Although the electron $g-2$ has already been measured with around 2000 times more precision relative to that of the muons [24], [25], higher order interactions with particles of larger masses contribute with mass suppression terms, $\propto (\frac{m_l}{M})^2$. Since the sensitivity to new physics grows quadratically with the mass of the lepton, the interesting effects are magnified in a_μ relative to a_e by a factor of $(\frac{m_\mu}{m_e})^2 \approx 43,000$. Although τ is a better candidate than μ in this respect, measuring a_τ is beyond current experimental possibilities, because of the very short lifetime of the τ.

The discrepancy between SM and experiment could be due to a statistical fluctuation, miscalculation of SM or systematic uncertainties in the experiment. There have been many efforts in both the theory and the experimental fronts and no errors found so far. There is a future experiment at JPARC that will measure a_μ independently using a new approach [26]. The Fermilab and JPARC experiment's motivation is to measure the same quantity again. If these experiments confirm the long standing discrepancy then next puzzle to solve is to what causes this deviation; The most exciting possibility would be hint of physics beyond the standard model. All particles that can couple to muon through virtual loops add to the value of a_μ. So the possibility remains that still undiscovered particles cause this discrepancy. The heavy virtual particle contribution to a_μ is expressed in terms of the mass m of the lepton, the mass scale of new physics $\mathcal{M}$, above the electroweak scale and the coupling constant C

$$a_\mu \sim C\frac{m^2}{\mathcal{M}} \tag{1.16}$$

The supersymmetry models supports the existence of such heavy particles, which are yet to be discovered [27]. Although based on the LHC experiments these supersymmetry models lost their grounds increasingly, but there are potential regions within the parameter space that could explain the $g-2$ deviation [28]. Another potential source could be from the radiative mass mechanisms in the energy range of $1-2$ TeV. Radiative mass mechanisms in that same energy range can also for the smaller mass of muons compared to electroweak gauge bosons [29]. Scalar doublet

models, two-Higgs-doublets among the others can also describe the discrepancy [30]. Although the dark photon model has been ruled out with 99% confidence level, the low energy BSM models can be a possible explanation of the discrepancy [30]. Future energy frontier experiments such as upgraded LHC experiments will be able to constrain the potential models. The Fermilab and the JPARC experiments probe indirect search of new physics, and are designed with a goal of measuring a_μ with improved precision. The Fermilab experiment aims to measure a_μ with a goal of 4-fold improvement on the uncertainty over the BNL experiment; by increasing the statistical precision by more than a factor of 20 and reducing the systematic uncertainty by a factor of 3. In the hypotheical situation where the central value remains the same, the Fermilab measurement will push the statistical significance of the deviation to $\sim 7\sigma$, shown in Fig. 1.6. The $g-2$ data also provides a great opportunity for setting the most stringent limits on some of the Standard Model Extension CPT Lorentz invariance violation parameters in the muon sector. This dissertation focuses on the Fermilab Muon $g-2$ Run 2 experimental data, collected in 2019, to probe CPT and Lorentz invariance violation signals. The Fermilab experimental result has potential to provide strong evidence for new physics, depending on its a_μ measurement.

1.5 CPT and Lorentz Violation Tests

The invariance of the combined transformation of C(charge cojugation)P(parity transformation)T(time reversal) and Lorentz transformation holds for the minimal standard model(SM) of particle physics. The SM is anticipated to be the low energy case of a more fundamental theory, such as string theory, grand unified theory (GUT) [31]. The high-precision feature of the Fermilab $g-2$ experiment can be exploited to probe CPT and LV signals, which are expected to be small in the energy scale of the experiment. In parallel, there have been extensive work in the theoretical front to describe CPT and LV within the framework of the standard model extension by Kostelecký et al. [32], [33]. The CPT and LV effects can be described quantitatively in the SME framework, where the source of such violations stems from spontaneous symmetry breaking. This is particularly a great approach of symmetry breaking because the underlying theory can still be CPT and

Lorentz symmetric, hence preserving the desirable features of the symmetry while the vacuum solution of the theory could violate these symmetries spontaneously [34]. The difference in SME from SM is that the vacuum is filled with vector quantities oriented in 4D and hence triggering spontaneous symmetry breaking by interactions that destabilizes the vacuum. The Lorentz and CPT symmetry are knotted by the CPT theorem which states that certain theories(local quantum field theory) obeying Lorentz symmetry must also abide by the CPT symmetry. CPT violation implies Lorentz violation but the reverse doesn't hold. The CPT theorem is automatically bypassed when Lorentz symmetry is broken. CPT violation is not a requirement for Lorentz symmetry to be broken; but allows for CPT breaking (in some cases). Phenomenological descriptions of CPT and Lorentz violation are easier to construct but in order justify the plausibility an underlying theoretical framework is needed. In this dissertation we adopt an approach for parameterizing the violation effects based on an effective field theory.

1.5.1 CPT and Lorentz Violation Experimental Signatures

The SME has the properties of SM and General Relativity with an exception of CPT and Lorentz violation. The observer Lorentz transformations; i.e, rotations or boosts along spatial directions in the observer's inertial frame, still remains invariant while the particle Lorentz transformations(rotations or boosts in particle fields) are violated in the SME framework. For the muon sector, the SME Lagrangian consists of 5 Lorentz and CPT violating terms in the QED limit, given as [32]

$$\begin{aligned}\mathcal{L}' = &-a_\kappa\overline{\psi}\gamma^\kappa\psi - b_\kappa\overline{\psi}\gamma_5\gamma^\kappa\psi - \frac{1}{2}H_{\kappa\lambda}\overline{\psi}\sigma^{\kappa\lambda}\psi \\ &+\frac{1}{2}ic_{\kappa\lambda}\overline{\psi}\gamma^\kappa\overleftrightarrow{D}^\lambda\psi + \frac{1}{2}id_{\kappa\lambda}\overline{\psi}\gamma_5\gamma^\kappa\overleftrightarrow{D}^\lambda\psi\end{aligned} \tag{1.17}$$

where all terms violate Lorentz invariance and CPT is broken for terms involving a_κ and b_κ coefficients, and $iD_\lambda \equiv i\delta\lambda - qA\lambda$. Each of these 5 terms are, by construction, a product of a coefficient with a LV operator, where the product is coordinate independent. Therefore the coefficients control the physics associated with any of the above operators, and allows for expressing

experimental signatures for LV in terms of the coefficients. These coefficients are anticipated to be suppressed by a factor of 10^{-20}, coming from the ratio of the muon mass to that of the Planck scale $\frac{m_\mu}{M_P}$. A non-rotating frame is considered for comparing different experimental results. The standard celestial equatorial frame $\{\hat{X}, \hat{Y}, \hat{Z}\}$ is chosen, where $\hat{Z}$ is along the Earth's rotational north pole. $\hat{X}$ and $\hat{Y}$ are along the equatorial plane of the earth. The earth's precession period is 26000 years and hence can be safely ignored in Lorentz and CPT violation tests. In the non-rotating equatorial frame the corrections to ω_a is calculated to be

$$\delta\omega_a^{\mu^\pm} \approx 2\check{b}_Z^{\mu^\pm} \cos\chi + 2(\check{b}_X^{\mu^\pm} \cos\Omega t + \check{b}_Y^{\mu^\pm} \sin\Omega t) \sin\chi \tag{1.18}$$

where

$$\check{b}_J^{\mu^\pm} \equiv \pm\frac{b_J}{\gamma} + m_\mu d_{J0} + \frac{1}{2}\varepsilon_{JKL}H_{KL} \tag{1.19}$$

with $J = X, Y, Z$ and χ is the colatitude of the experiment. Ω in the above equation represents the sidereal angular frquency and is expressed as $\Omega = 2\pi/T_s$, with $T_s \approx 23$ hours 56 minutes. For the Fermilab Muon $g-2$ experiment $\chi \sim 48.16°$ whereas for BNL it is 49.1°. Because of the earth's rotation there is a component in Eq. 1.18 that varies cyclically with a period of sidereal variation, $T_s = 23$ hours 56 minutes. Eq. 1.18 predicts two Lorentz and CPT violation signatures: a sidereal oscillation in $\omega_a(t)$, and a difference between time averages of $< \omega_a^{\mu^+} >$ and $< \omega_a^{\mu^-} >$. The signature stemming from μ^+/μ^- difference requires a μ^- run and hence falls under the future prospects of the $g-2$ experiment at Fermilab. This dissertation focuses on a sidereal signal search using the Fermilab Muon $g-2$ Run 2 data. The sidereal oscillation search provides information about the transverse component of the b_κ coefficients in Eq. 1.17 and can be calculated as

$$\check{b}_\perp^{\mu^\pm} = \sqrt{(\check{b}_X^{\mu^\pm})^2 + (\check{b}_Y^{\mu^\pm})^2} = \frac{\hat{\omega}_a^{\mu^\pm}}{2 \mid \sin\chi \mid} \tag{1.20}$$

with $\hat{\omega}_a^{\mu^\pm}$ being the sidereal oscillation amplitude of $\omega_a(t)$. A dimensionless figure of merit, $r_{\hat{\omega}_a} \equiv \frac{\hat{\omega}_a}{m_\mu}$, can be used for interpreting the observations as suggested by Kostelecky et al. [35].

CHAPTER 2

The Fermilab Muon $g-2$ experiment

The Fermilab Muon $g-2$ experiment aims to measure a_μ with a combined uncertainty of 140 ppb [36]. To support this groundbreaking precision, the experiment receives an intense muon beam from the Fermilab accelerator complex and aims to acquire more than 20 times the BNL dataset with a statistical uncertainty goal of 100 ppb. The systematic uncertainties come from the dynamics of the beam and detector effects. This chapter focuses on measurement principles and design choices to meet the uncertainty goal.

2.1 Measurement of a_μ

A particle with mass m, charge e and non-zero spin in an external magnetic field will experience a torque that tries to align the magnetic dipole moment along the magnetic field. Therefore in the presence of an external dipole field the spin of the particle will precess with spin precession frequency, $\boldsymbol{\omega_s}$ [37]. At the same time the particle will have an orbital cyclotron frequency, $\boldsymbol{\omega_c}$. In the scenario of a uniform magnetic field and particle velocity completely perpendicular to the external magnetic field, the equations of motion become

$$\boldsymbol{\omega_s} = -g\frac{Qe}{2m}\mathbf{B} - (1-\gamma)\frac{Qe}{\gamma m}\mathbf{B}, \tag{2.1}$$

$$\boldsymbol{\omega_c} = -\frac{Qe}{\gamma m}\mathbf{B}, \tag{2.2}$$

and the difference between $\boldsymbol{\omega_s}$ and $\boldsymbol{\omega_c}$ gives $\boldsymbol{\omega_a}$, the anomalous precession frequency,

$$\boldsymbol{\omega_a} = \boldsymbol{\omega_s} - \boldsymbol{\omega_c} = -\left(\frac{g-2}{2}\right)\frac{Qe}{m}\mathbf{B} = -a_\mu\frac{Qe}{m}\mathbf{B}. \tag{2.3}$$

where $\boldsymbol{\omega_a}$ is basically the rate of change of the angle between the momentum and the spin of the muon. The spin would remain parallel to the momentum vector if g were equal to 2. From Eq. 2.3 it is clearly seen that $\boldsymbol{\omega_a}$ is proportional to a_μ. Hence we are able to determine a_μ with a precise measurement of ω_a, provided we have an equally precise measurement of the external magnetic field. The magnetic field is measured using Nuclear Magnetic Resonance (NMR) techniques in terms of the Larmor precession frequency of the shielded protons in spherical sample of water

$$\hbar\tilde{\boldsymbol{\omega}}'_{\boldsymbol{p}} = 2\mu'_p\mathbf{B} \tag{2.4}$$

Therefore, the anomalous magnetic moment of the muon can be determined from

$$a_\mu = \frac{\omega_a}{\tilde{\omega}'_p(T_r)}\frac{\mu'_p(T_r)}{\mu_e(H)}\frac{\mu_e(H)}{\mu_e}\frac{m_\mu}{m_e}\frac{g_e}{2} \tag{2.5}$$

The total error on a_μ comes from the quadrature sum of the errors of each of the quantities in Eq. (2.5). High precision measurement of g_e has an uncertainty of 0.28 ppt [38]. $\mu'_p(T_r)/\mu_e(H)$ represents the ratio of the electron magnetic moment while bound in hydrogen to that of a shielded proton in a spherical water sample, measured to 10.5 ppb at a reference water temperature of T_r = 34.7°C [39]. The ratio of $\mu_e(H)/\mu_e$is determined by the bound-state QED corrections, and is considered exact [40]. The ratio of m_μ/m_e, has been measured by the hyperfine splitting of the muonium and bound state QED with an uncertainty of 22 ppb [41], [40]. These contributions to the total uncertainty are negligible compared to the Fermilab uncertainty goal of 100 ppb statistical error and systematic errors on ω_a and ω_p of 70 ppb individually.

2.2 Muon Beam Production and Journey to the Muon Campus

Muons are produced at the Fermilab accelerator complex in a number of stages. Fig.2.1 shows various components in the accelerator complex. Protons are produced by accelerating H^- ions in a linear accelerator. Protons are then sent to the "booster", a storage ring of radius 75 m, which then accelerates the proton beam to 8 GeV/c and batches them. One such booster batch

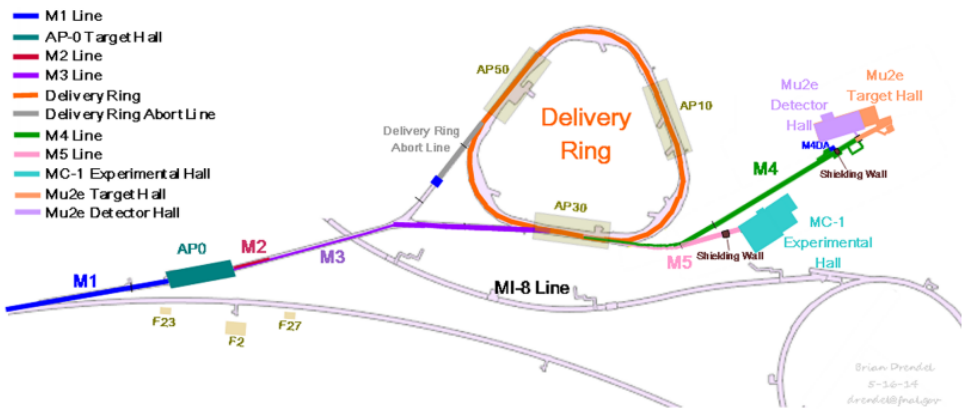


Figure 2.1: The schematic of accelerator beam-line components Fermilab uses to provide spin-polarized muon beam to E989. Protons start in the Linac, travel around the Booster and then the Recycler Ring, hit the nickel-based target at AP0, and produce pions. The pions then decay to muons in the Delivery Ring before reaching the muon campus [42].

consists of 4×10^{12} protons. These protons are then sent to the "recycler", where the proton beam gets separated into bunches containing 1×10^{12} protons, with a temporal width of $\approx$ 120 ns. The temporal width of the proton beam is less than 149 ns, the cyclotron period of the $g-2$ storage ring which is a requirement for the a_μ measurement. The re-bunching stems from the need to manipulate the flux rate at the detectors used for the $g-2$ experiment. In one accelerator supercycle of 1.4 s, 4 booster batches are delivered which correspond to 16 recycler bunches at an average rate of 11.4 Hz. Fig. 2.2 shows the timing structure crucial for recording the data from the detector.

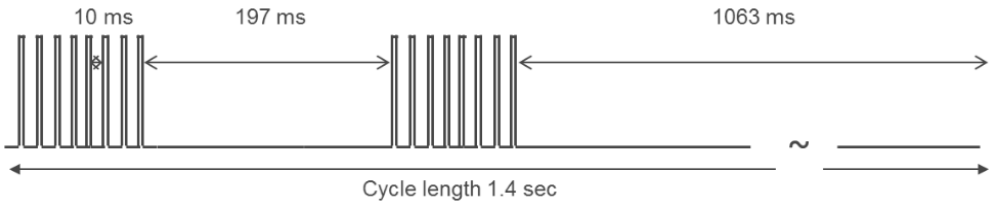


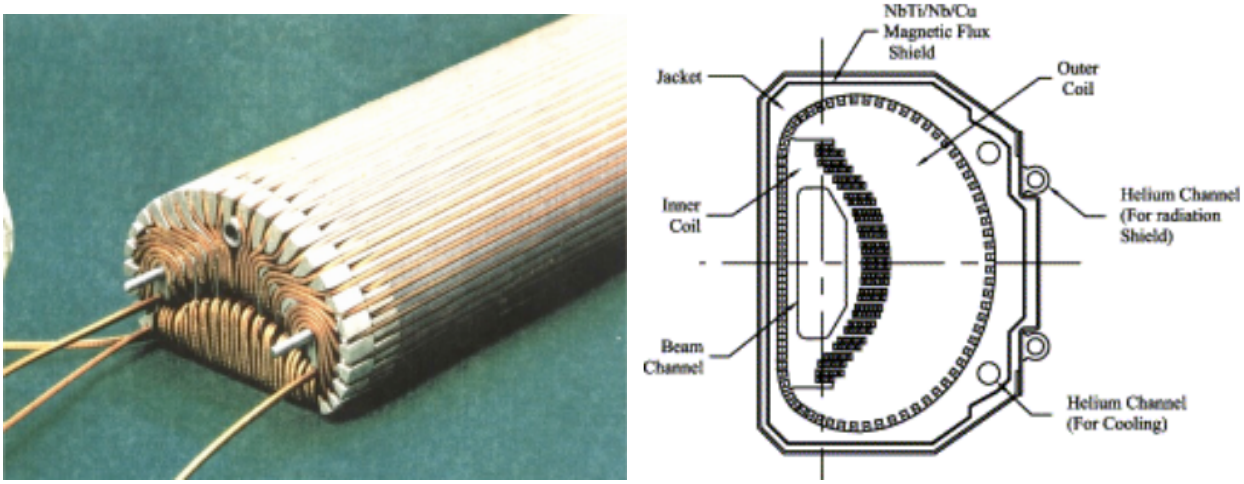
Figure 2.2: The timing structure of the beam sent to the muon campus at Fermilab. Each cycle consists of 16 bunches–10 ms apart–with a repetition rate of 11.4 Hz.

The proton beam hits the nickel-iron alloy target and positively charged particles are then directed through a lithium lens and a bending magnet. The energy of the secondary beam is selected to be around 3.11 GeV. This beam of pions, muons and protons then goes through a long transfer beamline to produce a pure muon beam. The secondary beam mostly has pions that decay into

muons with a branching ratio of 99.98%. To observe ω_a signal we need a highly spin polarized muon beam. That is achieved due to the parity violating nature of weak interactions. For the conservation of momentum, the ν and μ must travel in opposite directions in the rest frame of pion. Since pions are spin-0 and neutrinos are always left handed (LH), muons must as well be LH to conserve momentum. In the lab frame, this translates into a correlation between the muon spin and the direction of momentum. Accordingly, 95% of the beam is polarized by highest-momentum muon selection, with spin and momentum anti parallel. Around 80% of the pions decay into muons by the time the beam reaches the end of the transfer beamline. To obtain a pure muon beam, this secondary beam is then circulated around the delivery ring, shown in Fig. 2.1. All of the pions decay by the time the beam completes four turns around the delivery ring, and protons fall behind by $\sim$ 200 ns due to their small Lorentz boost. A pulsed electromagnetic magnet takes care those protons, and the final product is a highly intense and pure 3.09 GeV muon bunch. There are four quadrupole magnets for extracting and focusing the muon bunch, that then enters the $g-2$ storage ring through the inflector magnet.

2.3 Muon Beam Injection

The inflector, a superconducting magnet, is used to cancel the fringe field of the main storage ring magnet. We need the inflector magnet in order to maintain uniformity of the continuous storage ring magnetic field for effective muon beam storage. However, there must be a field-free injection tunnel through the storage ring magnet iron or else the injected beam would be deflected into the magnet mass. There is a superconducting shield outside the inflector to trap the fringe field in order to ensure the uniformity of the storage ring magnetic field. The inflector is placed 77 mm radially outward from the storage orbit in order to make sure that the muons don't hit the inflector on their way while orbiting the storage ring at the cyclotron frequency.



(a) Superconducting inflector magnet

(b) The inflector cross section

Figure 2.3: The inflector magnet and its cross section view

This necessitates a kicker magnet, providing a transverse impulse to "kick" the beam from the injection orbit to the storage orbit. The kicker magnet consists of three pulsed magnets located at 90° from the injection point. The placement is shown in Fig. 2.4. Since the kicker needs to be within the main magnetic field it must not have any magnetic elements. Each of the three magnets consists of two 1.27 m long thin aluminum plates, separated by 10cm, carrying the current needed to create the "kick". The required field is around $200 - 280$ G to provide a 10.8 mrad kick to the incoming muon beam. The kicker magnets reduce the 1.45 T magnetic field locally by 22 mT to provide the "kick". This field must be zero well before the bunch starts its second turn, so the kicker pulse must be greater than 120 ns to contain the entire muon bunch, but less than the 149 ns cyclotron period.

2.4 Muon Beam Storage and Focusing

The uniform dipole magnetic field in the storage region comes from the magnetic storage ring itself, which is inherited from the BNL experiment.

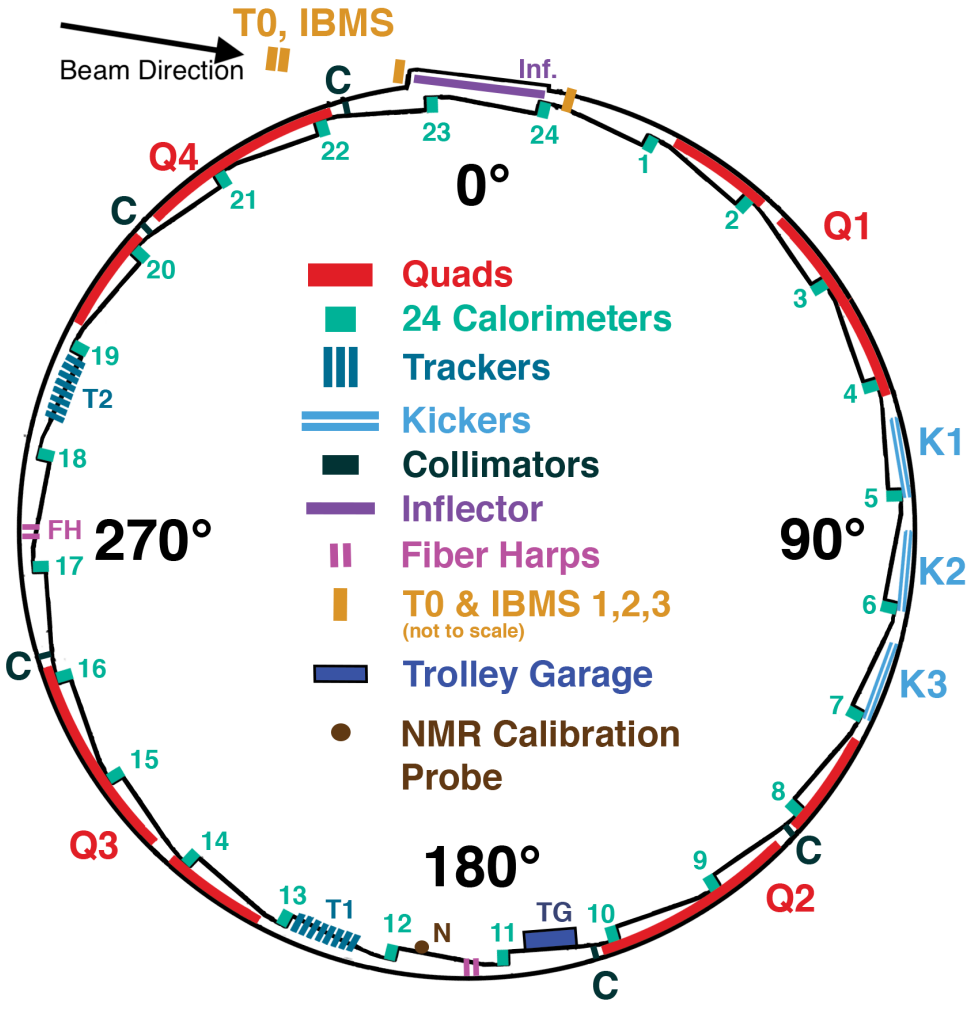


Figure 2.4: A map of the vacuum chambers. K1-K3 show the locations of the kicker magnets, while Q1-Q4 show the locations of the electrostatic quadrupoles. Also shown is the location of the inflector

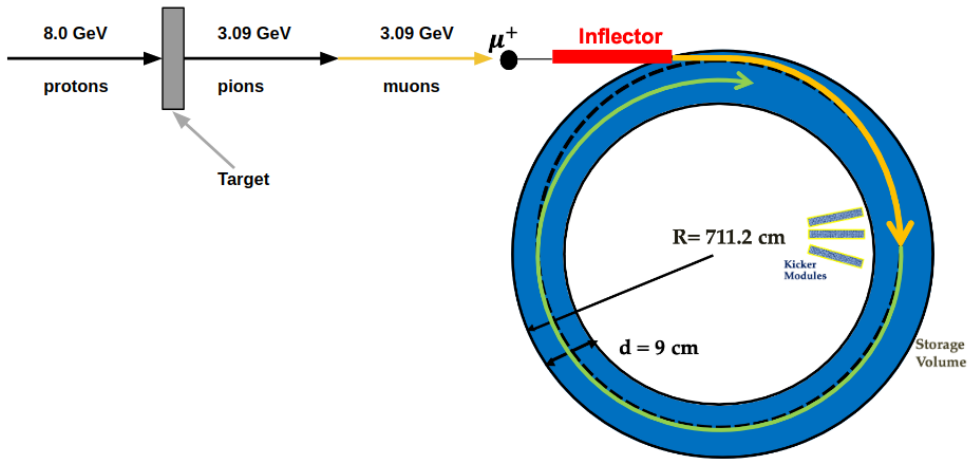


Figure 2.5: An illustration of production and injection of the muon beam into the storage ring. accelerated protons hit the Inconel target to produce charged pions which then decay to muons. These high energy muons are then injected into the storage ring through the inflector magnet. A "kick" is then applied by a kicker magnet to store the muons on the design storage orbit.

Since the main magnetic field is vertical, the force exerted by it will be in the horizontal direction only. Therefore the magnetic field alone is insufficient to store the muons, as a muon with a velocity component parallel to the magnetic field will leave the storage ring. Four pairs of short and long electrostatic quadrupole (ESQ) plates are used to focus the beam vertically and are placed inside the vacuum chambers. The short plates span 13° of the storage ring while the long plates span 26°. A four fold asymmetry is achieved by using the combination of the short and long quadrupole plates. The quadrupole system is turned on during a measurement period, but is otherwise turned off so as to reduce the rate of high voltage electrical sparking. The quadrupole plates are shown in Fig. 2.6. The high voltage system consists of resistors that sit outside the vacuum, and combined with the plate capacitance, determine the RC time constant of the system to be $5\mu s$. A DC power supply could have been used instead of the pulsed system but that would increase the rate of the high voltage breakdown of the system. The top and bottom plates are charged with positive voltage while the side plates of the quadrupole are charged with negative voltage in order to create a restoring force in the vertical direction. The quadrupoles only occupy 43% of the storage ring circumference due to accommodate the other systems discussed above

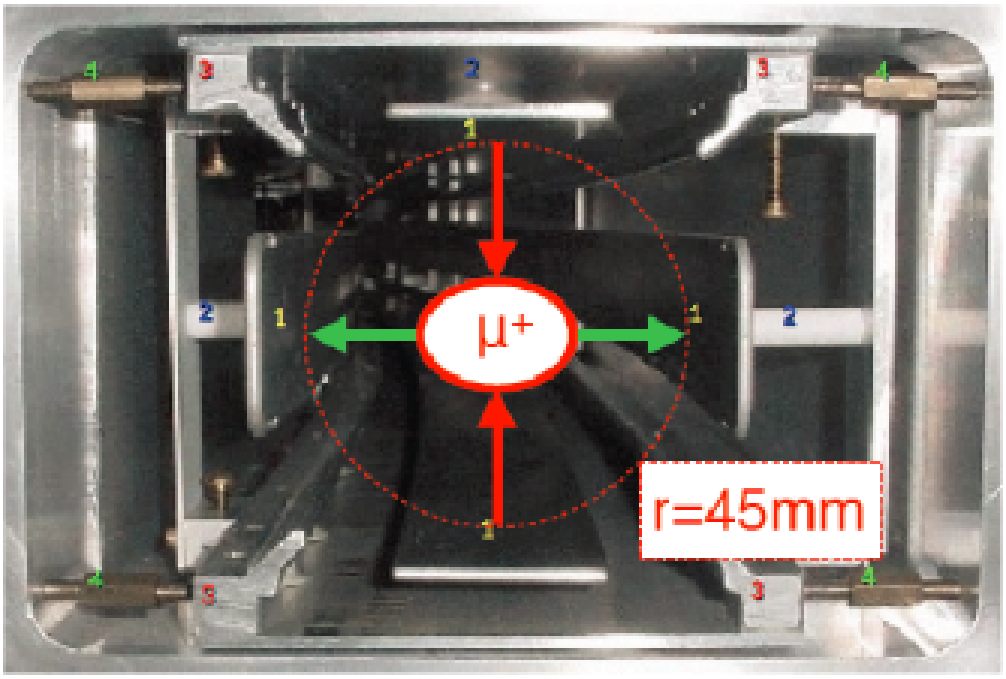


Figure 2.6: Figure shows 4 quadrupole plates within the storage region. The top and bottom plates are positively charged while the side plates are negatively charged to provide the vertical focusing for the positive muon beam.

along with tracker detectors placed azimuthally at 180° and 270°, causing a larger vertical spread at some places around the ring. The plates are charged by high voltage pulses, and then held at a constant voltage during the measurement period. The quadrupole plates were held at 18.3 kV during Run-2 data taking period. The quadrupole plates are discharged to zero at the end of every muon fill and are charged back up before the next fill arrives from the accelerator complex. The presence of the ESQ system affects ω_a measurement, and hence must be taken into account before reporting the final ω_a measurement.

2.5 Measuring the Magnetic Field

Fig. 2.7 shows a cross-section of the C-shaped 14 m diameter magnet, providing 1.45 T magnetic field. The uniformity of the magnetic field is crucial to ω_a measurement, as seen from Eq. 2.3 , and is manipulated by many built in "knobs". The main magnet current, wedges, pole pieces and top hats along with small shims are parameters used for fine tuning and stabilizing

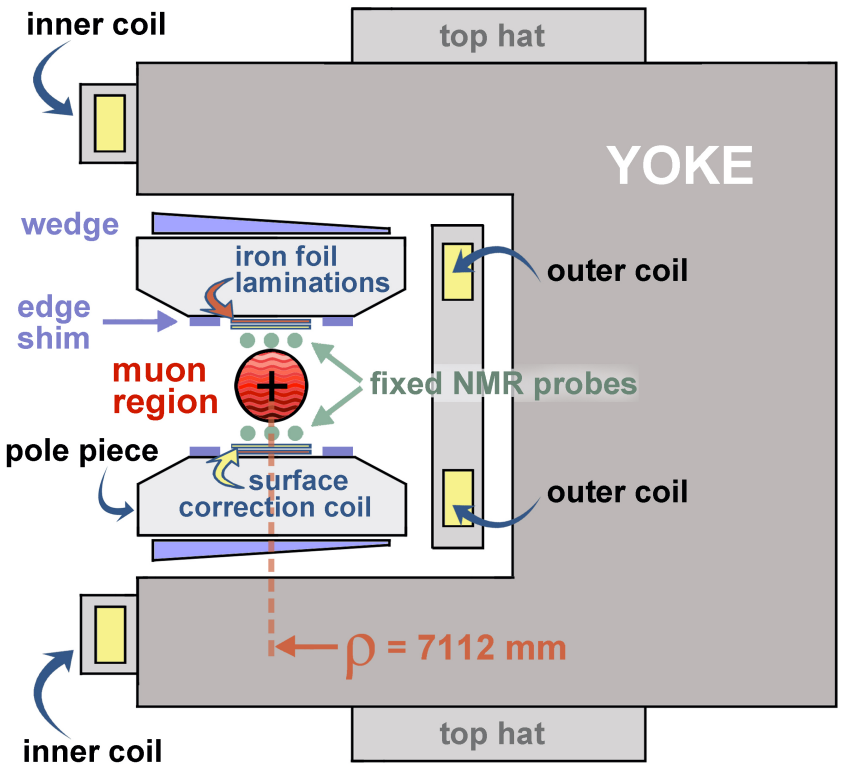


Figure 2.7: A cross-section of the $g-2$ storage ring. Superconducting coils in yellow excites the main magnet. Top hats, pole pieces, wedges used for subppm level adjustment of the field

the field seen by the muons. The pulsed nuclear magnetic resonance (NMR) technique is used to measure the magnetic field. NMR provides high precision measurements of the field, around 10ppb with negligible statistical uncertainty, and hence was chosen for the measurement [43]. NMR probes contain pickup coils around a proton sample within a fluid. The proton spin will precess at Larmor frequency in presence of an external magnetic field. The magnetization of the proton sample is rotated by 90 deg with respect to the external magnetic field from equilibrium by a radio frequency(RF) pulse, called '$\pi/2$ pulse', generated by the pickup coils. Since the spins interact with the external field gradients and inhomogeneities, the proton sample's magnetization will be in equilibrium with the external magnetic field. This is known as the free induction decay (FID) signal, as shown in Fig. 2.8 , and is meausred by the same pickup coils that were used to deliver the '$\pi/2$' pulse, connected to waveform digitizers recording the current induced in the coils by the

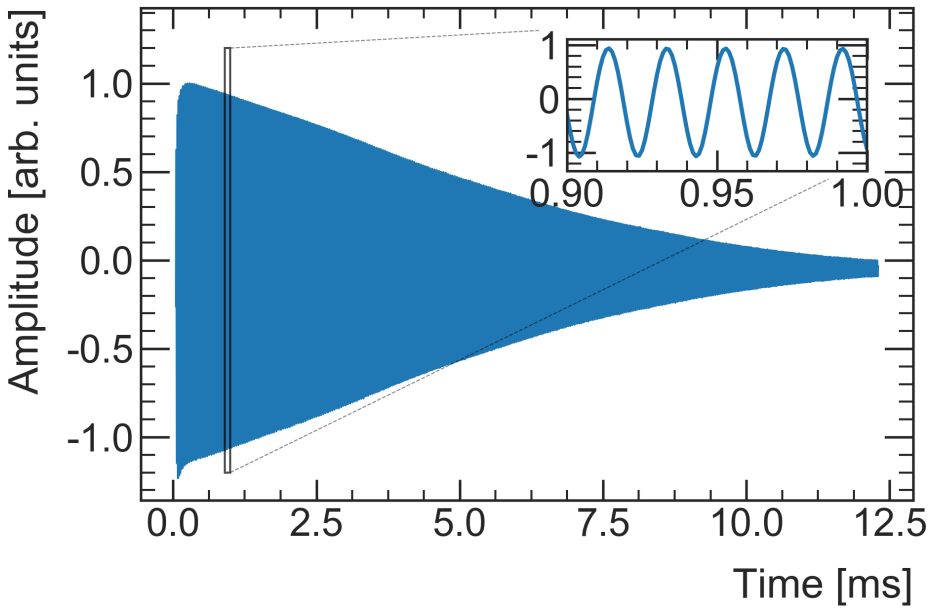
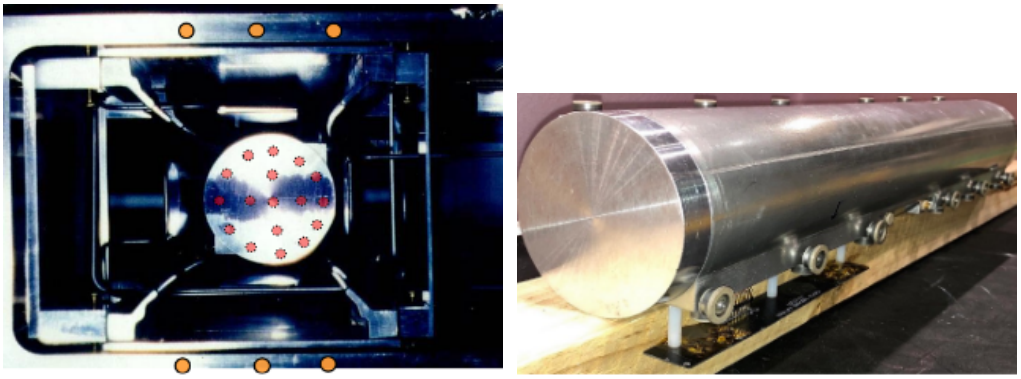


Figure 2.8: A sample FID signal. The pick up coil signals around the proton sample will oscillate as the spins precess around the external magnetic field, and decay as the spins relaxes back.

precessing protons. In order to map the magnetic field precisely around the storage ring, a trolley moves around the ring inside the storage region. The trolley has 17 NMR probes measuring the field at ~ 9000 azimuthal locations. Since the trolley cannot be in the storage region while muons are present, another set of 378 fixed NMR probes is used to monitor the field. The fixed probes are located outside the storage region on the vacuum chambers. Since a trolley run around the ring interrupts storing the muons and hence data taking, the detailed mapping is performed every three days, while the field in between is interpolated using the fixed probes data. Fig. 2.9 shows the position of the fixed probes relative to the storage region, and the trolley probe. This way the magnetic field can be mapped spatially as well as temporally. The precession frequency measured by the trolley probes or the fixed probes are not accurately the free proton precession frequency since it depends on parameters such as, molecular properties of the proton sample, shape of the probe sample etc. The expression for a probe sample with water

$$\omega_{p,\text{probe}} = \omega_{p,\text{free}} \left(1 - \sigma(\text{H}_2\text{O}, \text{T}) + \delta_\text{b} + \delta_\text{p} + \delta_\text{s}\right) \omega_p \tag{2.6}$$



(a) Fixed NMR probes (b) The trolley consisting of 17 NMR probes

Figure 2.9: The position of the fixed NMR probes that monitor the field 24×7 are shown in the left figure. The fixed probes sit above and below the storage region. The trolley that contains 17 NMR probes is shown in the right figure. The trolley goes around the ring every 3 days to provide a detailed map of the magnetic field inside the ring.

where $\sigma(H_2O, T)$ is the temperature dependent diamagnetic shielding, and δ's represent the susceptibility of water sample, magnetic effects of the probe, water sample's paramagnetic impurities.

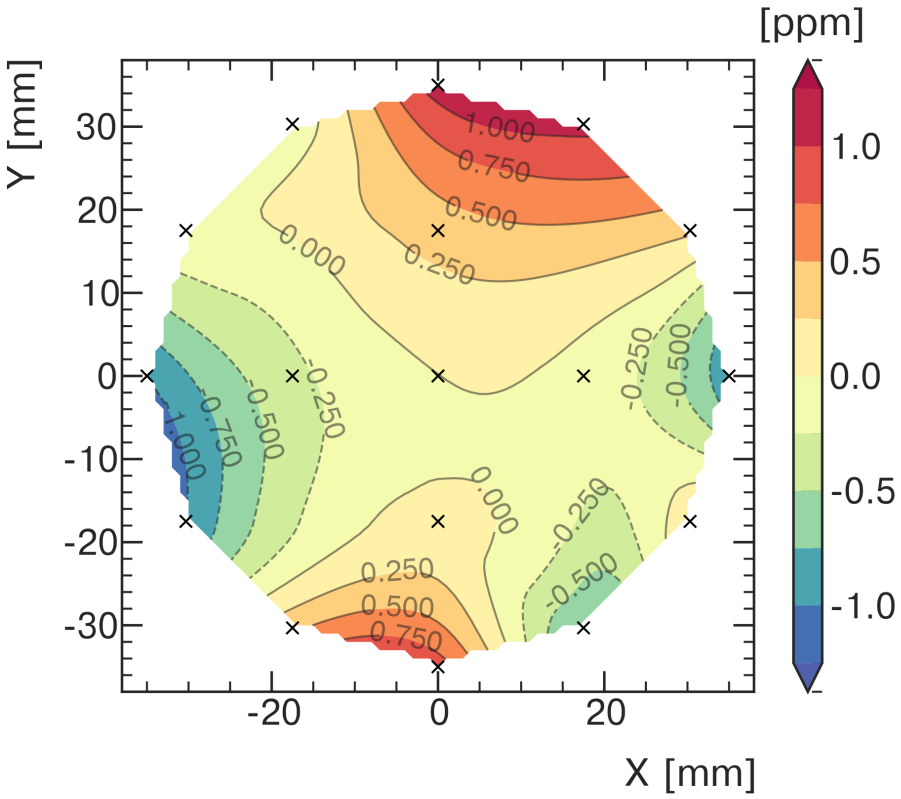


Figure 2.10: An example of azimuthally average magnetic field map provided by the trolley in the storage ring. The (x) marks indicate the location of 17 NMR probes within the trolley

A "plunging probe" is used in order to correct for these effects. It is placed inside the storage region so that the field can be measured at the same positions as the trolley probe. This probe can provide an absolute scale for the measurements within the storage region by calibrating the free proton precession frequency to each of the trolley probes. There is a 35 ppb uncertainty on the calibration process, which is nearly half total uncertainty goal of 70 ppb. Some of the other systematic uncertainties come from the errors in the trolley measurements, probe calibrations, interpolation of the field between trolley runs by the fixed probes etc.

2.6 Muon Beam Dynamics

Muons injected into the storage ring, in practice, have a finite momentum and position spread as they enter the ring with a spread of angles relative to the storage orbit and then are kicked imperfectly to occupy a non zero radial distribution. Thus, other than exhibiting a cyclotron motion around the ring, the muons also undergo betatron oscillation in the radial ($x = r - R_0$) as well as vertical (y) directions.

In order to predict the equation of motion of the muons, consider a muon with momentum 3.09 GeV, which is also the design momentum for the experiment (discussed in 2.8.2). Additionally, the magnetic field provided by the storage ring and the electric field due to the quadrupole systems can be expressed as

$$\mathbf{B} = B_0\hat{y} \tag{2.7}$$

$$\mathbf{E} = kx\hat{x} + ky\hat{y} \tag{2.8}$$

where k indicates the quadrupole field strength. The equations of motion along these two directions can be written as

$$\ddot{x} = -\omega_c^2(1-n)\cdot x \tag{2.9}$$

$$\ddot{y} = -\omega_c^2 n\cdot y \tag{2.10}$$

where n, the field index, is related to k by $n \equiv \frac{kR_0}{v_0 B_0}$ and $\omega_c (= QeB_0/m_\mu\gamma)$ is the cyclotron frequency.

The solutions to Eqs. (2.9) and (2.10) considering the discrete quadrupole effects are

$$x(t) = x_e + A_x \cos(\omega_x t + \phi_x) \tag{2.11}$$

$$y(t) = A_y \cos(\omega_y t + \phi_y) \tag{2.12}$$

where x_e is the equilibrium radius,

$$x_e \approx \frac{R_0}{1-n}\frac{p-p_0}{p_0} \tag{2.13}$$

A_x and A_y are the amplitudes of the motion with quadrupole effects included and ω_x and ω_y are related to the field index n by

$$\omega_x = \omega_c\sqrt{1-n} \tag{2.14}$$

$$\omega_y = \omega_c\sqrt{n} \tag{2.15}$$

Eqs. (2.11) and (2.12) show that a radial or vertical displacement from R_0 causes a simple harmonic motion of the muon, also known as the betatron oscillation.

The muons will encounter local field gradients and higher order perturbations several times on their way around the storage ring. To prevent the potential resonant oscillations it is important to make sure that muons do not have the same betatron oscillation phases while passing through the perturbations. The beam is "tuned"accordingly to spread the beam equally around the entire azimuth in order to miss the resonances and store the beam.

2.6.1 Coherent Betatron Oscillation

As discussed above in 2.6, each muon in the beam undergoes betatron oscillations. If the phases of these betatron motion were randomly distributed, then the beam could be treated as a constant entity in time. However, in reality, the beam has a particular phase space distribution induced by the inflector and the kicker. The 77 mm radial offset at the injection and afterwards an imperfect kick will leave the beam with a width and mean, dependent on the phase and stregth of the kicker pulse as well as the injection process, causing an oscillation of the mean position. The

calorimeter detectors are sensitive to register the betatron oscillations. The detector acceptance, which is given by the probability of a positron hitting the detector, will depend on the mean and width of the muon distribution at a particular time. A mismatch is introduced by design between the wavelength of the betatron oscillation and the circumference of the ring to avoid sitting on the resonances. The radial betatron frequency, ω_x is larger than half the cyclotron frequency for the design choice of the Fermilab experiment, and hence introducing an aliasing effect. The detector instead observes the beam with a slower oscillation than the original betatron motion because of the aliased frequency. This detector measurable effect is known as the coherent betatron oscillation (CBO).

$$f_{CBO} = f_c - f_{x_{BO}} \tag{2.16}$$

The effects stemming from the coherent betatron oscillations must be taken into account before extracting ω_a. Hence the five parameter fit model needs modification in order to include the CBO effects. The CBO oscillations will end up modulating the asymmetry and phase information because of the modulation in detector acceptance.

2.6.2 Beam Debunching

The muon beam in the Fermilab experiment has a temporal width of 120 ns and upon injection only covers a fraction of the ring as it is narrower than one cyclotron period, $\sim$ 149 ns. Because of this spatial confinement of the beam at initial injection only detectors near the bunch will observe a high intensity and the detectors on the other side at the same time will observe a low intensity; hence the event rates vary with the cyclotron frequency at each detector. As the muon beam has a momentum distribution, not all the muons are at the "magic "-momentum. Higher momentum muons will sit at a larger equilibrium radii and hence will traverse a larger distance, therefore taking longer to go around the ring compared to the lower momentum muons. Eventually the low momentum muons that are at the inner radii catch up with the high momentum muons, and the bunch structure fades away. By $30\mu s$ after injection the beam has completed two hundred turns and the intensity of the beam is mostly uniform. The debunching effect at early times can be

observed in the data, a common practice is to bin the data in periods of the cyclotron frequency, and randomize each event by $\pm 149/2$, where the cyclotron period is 149ns. The initial spatial distribution of the beam can be estimated from the detector respnses at early times, which then can be used to estimate the electric field correction (discussed in 2.8.2).

2.7 The Detectors

There is a wide range of detectors used in the Fermilab Muon $g-2$ Experiment. The primary detectors are the calorimeter detectors, which provide the information needed to extract the precession frequency of the muons. There are many auxiliary detectors that are used for monitoring the beam. There are two stations of straw tracking detectors at 180° and 270° around the ring, which measure the positrons and hence we can extrapolate the decay position.

2.7.1 Auxiliary Detectors

There is a "T0" counter right before the inflector that provides the timing and intensity information of the muon beam. In order to time-align various detectors a reference time must be chosen, otherwise comparing the data from different detectors would not be possible. Furthermore, there must be phase alignment within the positron spectra from one to fill to another. The "T0" counter which is made up of scintillating paddle with photo-multiplier tubes (PMTs) provide the time information of the injected muon beam profile.

The inflector beam monitoring system (IBMS) sit before the inflector and measures the beam position [44]. The IBMS system provides inputs that are used to match the phase space between the last accelerator component that the muons pass through and the storage ring, and hence helping in optimizing the stored muons. The IBMS is also made up of scintillating fiber detectors. Currently there are two IBMS systems placed before the inflector, as shown in Fig. 2.11. In future, there are plans to install another device near the downstream of the inflector.

Another auxiliary detector known as "fiber harp" is used to provide a handle on the beam intensity as a function of position and time inside the storage region [45]. This detector, made up of

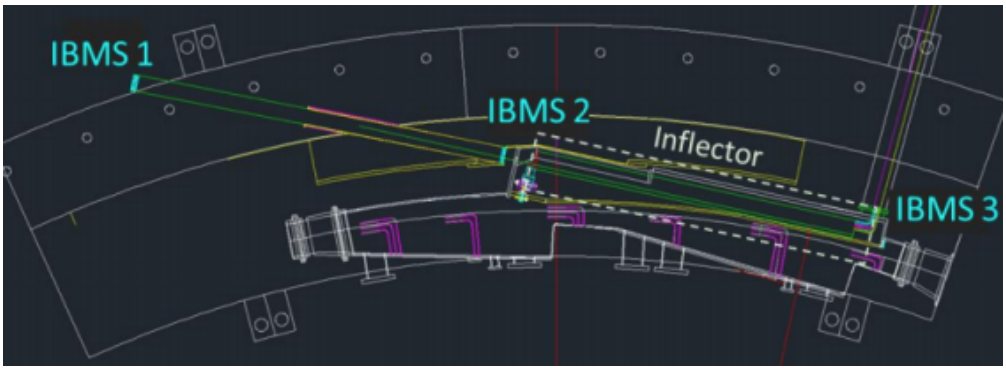


Figure 2.11: A schematic showing the position of the IBMS detectors

four scintillating fiber detectors is usually retracted in the measurement period due to its destructive nature of causing multiple scattering.

2.7.2 Calorimeter Detectors

The primary detectors used in the experiment are the electromagnetic calorimeters. The calorimeter detectors provide the energy and time information of the positrons that curl inward and hit the detectors.

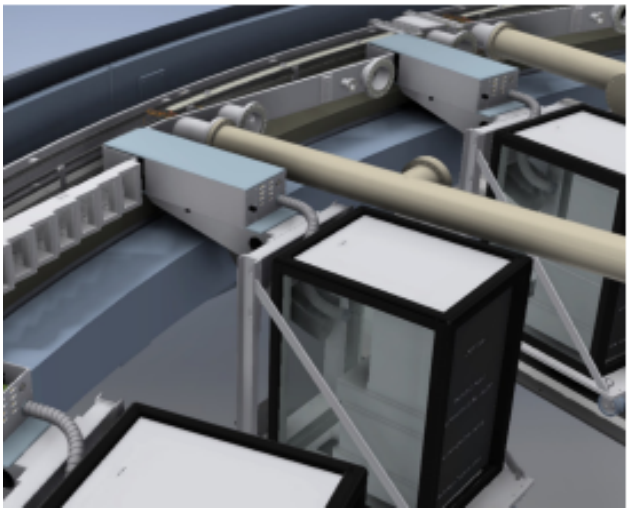
The precision of the ω_a measurement depends on the performance of the calorimeter detectors. Hence, there are specific requirements on the timing and the energy resolution of the detector. The detectors must distinguish multiple events with an efficiency of 100% when the temporal separation between two events are more than 5 ns. The requirements on the time resolution also helps to the "pileup" effects. Pileup refers to multiple overlapping events that are too close in time and space to be resolved. The detectors are required to have an energy resolution of more than 5% at 2 GeV [46]. The detectors used in the experiment also satisfy the requirement of having a timing resolution of 100 ps for events that have energy greater than 100 MeV. Another important requirement for the measurement of the precession frequency is that the response of the detectors be stable over the measurement period of $700\mu s$. The energy response is often referred to as the gain of the calorimeter; the gain is basically the current per hit. Gain of the detector is controlled by the rate at which the detector is hit and the temperature stability. If the pixels in the detector are fired by two consecutive hits that are very close to each other in time, then the detector

would not be able to fire for the second hit within a short time frame as there would be charge depletion in the capacitive components of the detector's electronics, and there must be corrections applied before using the information of the second hit. A laser calibration system is used in order to correct the gain of the calorimeters.

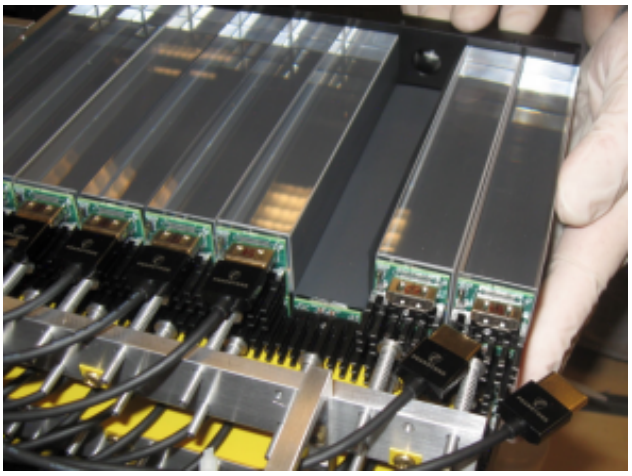
24 calorimeters are placed around the inside of the storage ring in order to detect the positron events. The calorimeter detector is placed on a board attached to a cart that contains the power and read out electronics, as shown in Fig. 2.12a. The movable carts are used to keep the magnetic materials away from the high magnetic field region so that any potential field perturbations can be avoided. Each of the 24 calorimeters consists of 9×6 PbF_2 crystals with 1296 channels. These $2.5 \times 2.5 \times 14$ cm^3 crystals are wrapped in black Tedlar foils in order to prevent inter crystal leakage of the signals. Fig. 2.12b shows a close view of the PbF_2 crystals. Due to the high density of PbF_2 crystals, almost 100% of the positron energy is deposited within the length of the crystal [47]. Cerenkov light is emitted upon a positron hit with energy 100 keV, which is then detected by the silicon photo-multiplier (SiPM) sensors. High photo-detection efficiency of the SiPMs make them an ideal choice for Cerenkov light detection. SiPM channels are then sampled by waveform digitizers, and finally are sent to GPU processors for on-line processing and monitoring.

2.8 Measuring ω_a

Muons trapped in the storage ring decay to two neutrinos and a positron with a branching ratio of 99.98%, as shown in Fig. 2.13. The muon's spin direction is correlated with the daughter particle's energy and directionality. Hence enabling us to measure the average direction of the muon's spin over time from the detection of the positrons. The decay positron will be emitted with its spin parallel to its momentum, i.e. right handed, due to the parity violating nature of weak interactions [] while the angular momentum must be conserved in the decay. The correlation between muon's spin and decay positron's energy can be understood by considering the extreme cases. ν_e and $\bar{\nu}_\mu$ both will be emitted in the opposite direction in the muon's rest frame when the decay positron is emitted with the maximum energy, as shown in Fig.. The spins of ν_e and $\bar{\nu}_\mu$ will



(a) A schematic of the calorimeter detectors placed in the movable carts



(b) A close view of the PbF_2 crystals connected to SiPMs at the end in order to collect the Cerenkov light from the positron hits

Figure 2.12: The calorimeter detector placed on the inside of the ring. The right figure shows the PbF_2 crystals within a calorimeter

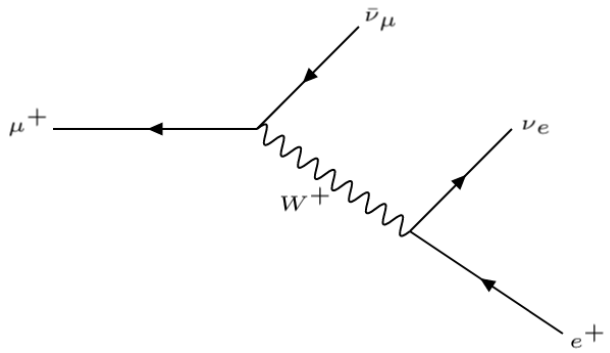


Figure 2.13: μ^+ will decay through a W^+ boson to two neutrinos and a positron with a branching ratio of 99.98%

cancel each other since neutrinos and anti-neutrinos are always LH and RH respectively. Therefore, the e^+ must carry the spin information of the muon at the time of its decay due to conservation of angular momentum. As mentioned earlier, the parity violating nature enables a correlation that can now be exploited, high energy positrons will be preferentially emitted parallel to the muon's spin direction. On the other hand if we consider the minimum energy scenario, the neutrinos are emitted in opposite direction and the minimum energy e^+s emitted with spin anti-parallel to that of the muon. Hence it is evident that the high energy positrons is emitted parallel to the muon spin when it decays, whereas relatively lower energy e^+s will be emitted with a spin anti-parallel to the spin of the muon. Therefore, the correlation between the directionality of a high energy e^+ and muon's spin encrypts the ω_a signature. The differential decay in muon's rest frame can be written in terms of the decay positron's energy E and the decay angle θ relative to the spin direction of the muon

$$\frac{d^2P}{dEd\cos(\theta)} = \mathrm{N(E)}\,[1 + \mathrm{A(E)}\cos\theta] \tag{2.17}$$

where

$$\mathrm{N(E)} = 2\mathrm{y}^2(3 - 2\mathrm{y}) \tag{2.18}$$

$$A(E) = \frac{2y - 1}{3 - 2y} \tag{2.19}$$

with $y = E/E_{max}$. N(y) refers to the number distribution of the decay positrons and A(y), the asymmetry, encrypts how strongly the muon spin direction is correlated to the positron's momentum.

Almost all of the high energy decay positrons will be emitted parallel to the momentum direction of the muon in the lab frame. This makes it difficult to measure the positron's average angle θ over time. On the other hand we know that the highest energy decay positrons in the rest frame is emitted along the muon spin when it decayed. The high energy positrons' energy distribution is modulated by ω_a, where $\theta = \omega_a t + \phi$. The number of positrons detected at time t in the lab frame can be expressed in terms of an initial number N_0

$$\mathrm{N(t, E)} = \mathrm{N_0(E)e^{(-t/\gamma\tau_\mu)}}\left[1 + \mathrm{A(E)}\cos(\omega_\mathrm{a}\mathrm{t} + \phi(\mathrm{E}))\right] \tag{2.20}$$

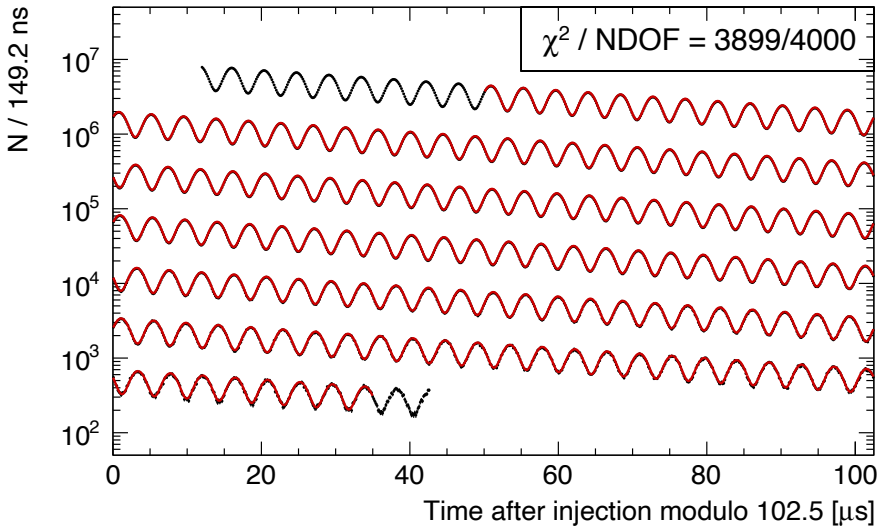


Figure 2.14: A typical wiggle plot from the calorimeter detectors in the Fermilab experiment showing number of detected positrons as a function of time above an energy threshold. The time spectrum is folded into a 100μs window

After transforming from rest frame to lab frame Eq. (2.18) and Eq. (2.19)

$$\mathrm{N_0(E)} \propto (\mathrm{y} - 1)(4\mathrm{y}^2 - 5\mathrm{y} - 5) \tag{2.21}$$

$$\mathrm{A(E)} = \frac{-8\mathrm{y}^2 + \mathrm{y} + 1}{4\mathrm{y}^2 - 5\mathrm{y} - 5} \tag{2.22}$$

The polarization of the muons was considered to be unity. For observing the muon spin precession,

positrons above a certain energy threshold can be considered,

$$N(t, E_{th}) = N_0(E_{th})e^{-t/\gamma\tau_\mu}\left[1 + A(E_{th})\cos(\omega_a t + \phi(E_{th}))\right] \tag{2.23}$$

where N_0 and A(y) can re-written by taking the integral of Eq. (2.21) and Eq. (2.22)

$$N_0(E_{th}) \propto (y_{th} - 1)^2(-y_{th}^2 + y_{th} + 3) \tag{2.24}$$

$$A(E_{th}) = \frac{y_{th}(2y_{th} + 1)}{-y_{th}^2 + y_{th} + 3} \tag{2.25}$$

Now the precession frequency, ω_a can be extracted by fitting time spectrum that arises from counting the number of positrons above an energy threshold. For this, a typical fit function has the form same as Eq.(2.20). Fig.() shows the positron time spectrum above a threshold as seen by the detectors.

With an assumption of Gaussian bin errors and performing a χ^2 minimization for the fit in order to extract ω_a, the statistical error is given by

$$\frac{\sigma_{\omega_a}}{\omega_a} = \frac{\sqrt{2}}{\sqrt{N_{total}}A\gamma\tau_\mu\omega_a} \tag{2.26}$$

where N_{total} is the total number of events in the time spectrum above a certain threshold. From Eq. (2.26) it is evident that ω_a measurement has maximum statistical precision when $N_{total}A^2$ in the denominator is maximized. Eq. (2.26) is valid for a weighting sceme of one for every count in the time spectrum, as used in this dissertation. The optimal energy threshold was found to be 1.7 GeV, including detector acceptance effects and an asymmetry of 0.37 for the Fermilab experiment. For a 100ppb statistical goal of the Fermilab experiment, Eq. (2.26) shows that the number of positrons to be fitted for the final ω_a extraction should be $\sim 170 \times 10^9$, where $A = 0.37$, $\gamma = 29.3$, $\tau_\mu = 2.2\mu s$ and $\omega_a = 1.44 rad/\mu s$. This statistical error is finally combined with the systematic error on the ω_a measurement.

2.8.1 Systematic Effects

The ω_a measurement is robust and straightforward in a sense that it depends on the time oscillation in the number of positrons that hit the detector, and knowledge of accurate energy dependence of the detector acceptance or exact calibration of the detectors is not necessary. Differing detector response or decay distributions may end up affecting the normalization, phase or asymmetry in Eq. (2.20), while the frequency ω_a remains unaffected by these effects. The fit parameters in the precession frequency fit as described by Eq. (2.20) however is not sufficient for ω_a extraction as there are effects that modify the frequency and are not being taken into account by Eq. (2.20). Time dependent effects may bias the ω_a measurement, and hence must be estimated and considered as systematic uncertainties on the ω_a measurement. The sources of systematic uncertainties can either be due to beam dynamics effects or detector effects. Some of the beam dynamics effects are taken in to account by applying a correction to the final ω_a after performing the fit. The beam dynamics effects are primarily from the behavior of the stored muons in presence of various systems, such as electrostatic quadrupoles. On the other hand, the detector effects are caused by the imperfections of the calorimeter, such as, finite time and spatial resolution. The experiment is designed to limit the combined systematic uncertainty to 70 ppb after four years of running.

The quantities, energy (E) and time (t), in the differential decay equation are not exactly what the detectors measure. The energy and time information provided by the detectors differ from those information at the time of the decay. Now if the effects that are responsible for this transformation are time dependent within a muon fill, that can modify ω_a. This can be easily understood by considering a scenario of a drift time that is energy dependent. Now replacing t by $t + t_drift$ in (2.20) only results in a constant phase offset which does not affect the best-fit ω_a. A time dependent phase on the other hand, would introduce a systematic bias in the ω_a measurement by pulling the best-fit ω_a value from the actual ω_a value if not modelled correctly within the fit function. The betatron motion of the muons, is an example of such an effect, which modifies the detector acceptance and the average drift time and hence introduces a time dependent phase.

Considering a time dependent ϕ the oscillation in time spectrum will be modified as

$$\cos(\omega_a t + \phi(t)) \approx \cos(\omega_a t + \phi_0 + \frac{d\phi}{dt}) = \cos((\omega_a + \frac{d\phi}{dt})t + \phi_0) \tag{2.27}$$

where ϕ is expressed in terms of a power series of $\phi_0 + \frac{d\phi}{dt} + ...$ It is therefore evident from Eq. (2.27) that any effect that modifies the observed phase qualifies as a potential source of systematic error to the best-fit value of ω_a.

To achieve the 70 ppb systematic uncertainty goal, one of the significant improvements were in the design of the calorimeter detectors to provide excellent energy resolution and time information. Therefore reducing the systematic uncertainty coming from the so-called pileup events. The pileup events refer to two or more overlapping events hitting the detector too close in space and time. In that case the overlapping pulses cannot be separated from each other and are treated as a single pulse of higher energy, and hence alter the number of positrons contributing to the histogram for ω_a extraction. Pileup can either add events (two lower energy pulses add up to mimic a single higher energy pulse above threshold) or subtract events (two pulses above the energy threshold add up to form a single pulse) from the time spectrum of the decay positrons above an energy threshold. Since pileup events are pulses with a different $g-2$ phase,[1], the phase of the pileup events differs from that of the single decay positron events. Therefore, pileup events distort the decay pobsitron time as well as energy spectra and we must apply pileup corrections before extracting the ω_a value. This incorrect energy will encrypt wrong asymmetry, normalization and phase information but does not cause an ω_a bias as long as the distortions are not time dependent. However, the total rate of events hitting the calorimeter detectors decreases within a fill as the muons decay and the two positron pileup rate is proportional to the total rate of positron events squared. Hence the pileup perturbation decays with time as well. Because of the time dependence of the perturbation there will be a bias in precession frequency measurement if not corrected. The

[1]The spin precession phase depends on the energy of the positrons as higher-energy positrons traverse a longer path from the decay vertex to the calorimeter and arrive later than lower-energy positrons. Pileup pulses carry the phase information of the lower-energy positrons rather than the phase of the high energy positron that they imitate

algorithm used to correct for pileup will be discussed in the next chapter.

2.8.2 Electric Filed and Pitch Correction

The expression used for the anomalous precession frequency in Eq. (2.3) is modified in the presence of various systems such as, the electrostatic quadrupoles. The muons enter the storage ring with a range of vertical angles, and hence a vertical focusing by the electrostatic quadrupoles is needed. Introduction of such an external electric field ends up modifying Eq. (2.3). Further correction comes from the fact that not all the muons have zero velocity component parallel to the direction of the magnetic field. Hence a more complete depiction of the scenario observed experimentally is given by

$$\boldsymbol{\omega_a} = \boldsymbol{\omega_s} - \boldsymbol{\omega_c} = -\frac{Qe}{m}\left[a_\mu \mathbf{B} - a_\mu\left(\frac{\gamma}{\gamma+1}\right)(\boldsymbol{\beta}\cdot\boldsymbol{B})\,\boldsymbol{\beta} - \left(a_\mu - \frac{1}{\gamma^2-1}\right)\frac{\boldsymbol{\beta}\times\mathbf{E}}{c}\right] \tag{2.28}$$

The second term arises from the vertical component of muon's motion which is parallel to the external magnetic field. Therefore a correction, also known as pitch correction must be applied to ω_a after extraction from the time histogram. Now if we consider the muon beam entering the storage ring to have no vertical component at all, i.e, $\boldsymbol{\beta}\cdot\boldsymbol{B} = 0$, then the contribution to ω comes the third term alone. The third term is zero if $\frac{1}{\gamma^2-1} = a_\mu$, which motivates the design choice of 'magic' muon momentum to be 3.094GeV. The electric field correction in this case comes from the off-magic momentum muons with $p \neq p_m$, where p_m is the magic momentum. The fractional shift in $\boldsymbol{\omega_a}$ is expressed as

$$\frac{\Delta\omega_a}{\omega_a} = -\frac{\beta E_x}{cB_0}\left(1 - \frac{1}{a_\mu\beta^2\gamma^2}\right) \approx -2\frac{\beta E_x}{cB_0}\frac{p-p_m}{p_m} \tag{2.29}$$

where β is almost constant, and E_x is the radial component of the electric field. The fractional shift further, can be written in terms of $< x_e^2 >$, as discussed in the previous section

$$\frac{\Delta\omega_a}{\omega_a} = -2\frac{n(1-n)\beta^2}{R_0} < x_e^2 > \tag{2.30}$$

where the radial position of the muons is x, and x_e is the equilibrium radius relative to R_0. $< x_e^2 >$ is evaluated from the event information of the detected positrons by calorimeter detectors for each dataset. The systematic uncertainty on this correction primarily arises from $< x_e^2 >$.

Now, to focus on the second term of Eq. (2.28), we assume that the electric field correction term is zero, i.e., $p = p_m$ for all muons and that they are injected with a small vertical angle, indicating $\beta \cdot \mathbf{B}$. Because of the betatron oscillations of the muons, the sign of the radial and vertical components of β will alternate. The vertical betatron frequency is modulated by the 'pitch' angle,

$$\psi(t) = \psi_{\max} \cos(\omega_y t) \tag{2.31}$$

The fractional shift in ω_a can be expressed as

$$\frac{\Delta\omega_a}{\omega_a} = -\frac{< \psi^2 >}{2} = -\frac{n}{2R_0^2} < y^2 > \tag{2.32}$$

considering small angle approximation and taking average over spin precession period[]. The relation between the pitch angle ψ and the vertical position y in Eq. (2.32) is expressed in terms of $\psi \approx \tan\psi = y\sqrt{n}/R_0$. As the pitch correction can directly be evaluated from the vertical distribution of the beam, which can be measured using the tracking detectors. A source of systematic uncertainty for the pitch correction stems from the measurement of $< y^2 >$. Combining these two corrections with the best-fit ω_a, the reported value of unbiased ω_a, that then goes into a_μ evaluation is slightly higher.

2.8.3 The error budget

The Fermilab g-2 experiment design aims to reach a four-fold improvement in experimental precision compared with the BNL g-2 experiment (E821), which would reduce the error on the measurement of a_μ to the 140 parts-per-billion (ppb) level. The targeted statistical uncertainty of E989 is at the 100 ppb level. E989 must obtain twenty one times the amount of data collected for E821. This means that we need about 1.5×10^{11} decay positrons in the final fitted histogram. The

systematic errors of a_μ are derived from those on the anomalous spin precession frequency ω_a and the magnetic field normalized to the proton Larmor frequency ω_p, each of which is targeted to reach a 70 ppb level. Compared to E821, there will be a three-fold improvement on ω_a uncertainties and a two-fold improvement on ω_p.

ω_a Error budget			
Category	E821 [ppb]	E989 Improvements	E989 Goal [ppb]
Gain changes	120	Better laser calibration	20
Pileup	80	Calorimeter segmentation	40
Lost muons	90	Better collimation in the ring	20
CBO	70	Better match of the beamline to ring	< 30
E and pitch	50	Improved tracker	30
Total	180	Quadrature sum	70

Table 2.1: Systematic errors estimated for the anomalous spin precession frequency(ω_a) [**?**]

CHAPTER 3

Measurement of ω_a

The measurement of ω_a frequency is done by analyzing the time spectra from the calorimeter detectors. The time spectra from the detectors is basically the number of positrons above an energy threshold as a function of time, and this is modulated by the precession frequency, ω_a. Before the data is available in terms of the units of energy as MeV and time as μs, a huge effort goes into reconstructing the data from raw units.

Because the CPT and Lorentz violation analyses are essentially studies of variations in ω_a as a function of time and charge, the first step in the measurement is performance of the ω_a analysis. The details of this analysis, from constructing the so-called wiggle plot to considering some of the systematic effects is discussed in this chapter. Note that, any systematic effect that does not have a time varying effect is not particularly of interest from the Lorentz violation analysis point of view.

3.1 Energy and Time Spectra

From the reconstructed data of all the calorimeters the histograms for energy and time spectra are constructed. The information, such as energy, time, and hit positions of each event detected by the calorimeters are stored in ROOT TTree formats [48] and is made available to the analyzers. These data files are usually of the order $20000 - 140000$ data files for each dataset, which then is further processed, and for this dissertation analysis, a C++ based code in Fermilab's well known art framework was written [49]. This finally produces histograms defined by the TH1F class; the ω_a analysis is largely a cut based analysis and all the energy and time cuts were applied based on inputs from the simulation and suggestions from the collaboration to maintain a standard among various analyses. This dissertation includes plots from Run 2 datasets; Run 2 data contains

Common Parameter	Value
Energy threshold	1700 MeV
width of time bins	149.2 ns
Pileup scale factor	1
Pileup shadow time offset	10 ns
Pileup shadow window	1.5 ns

Table 3.1: Parameters used for Run 2 analysis among different datasets.

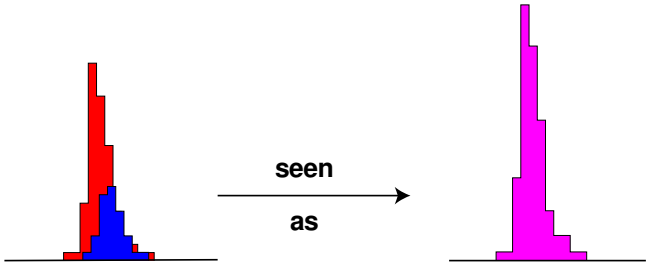
$\sim$ 11 billion events, after applying the required time and energy cuts; these events are used for the ω_a extraction. The parameters mentioned in the table were identical among different datasets.

Energy and time histograms are constructed for each calorimeter detector and then are added for the final ω_a extraction. The energy threshold chosen for this analysis is 1700 MeV; events with energy greater than the threshold are used for extracting ω_a. This is found to be the optimal threshold from studies performed based on concepts discussed in Chapter 2. The optimal energy threshold can be determined by performing a scan over energy thresholds and each time fitting the time spectra with a five parameter fit function. The bin widths in the time spectra were chosen to be 149.2 ns, which is the cyclotron period. The typical approach is to smear the bins by randomizing each event time by $\pm T_c/2$, where T_c is the cyclotron period. This is a known approach to smear frequencies from the data. ROOT's TRandom3 class was used for this randomization. The range chosen for the time histograms is $0 - 699.8972\mu s$ with a total of 4691 bins.

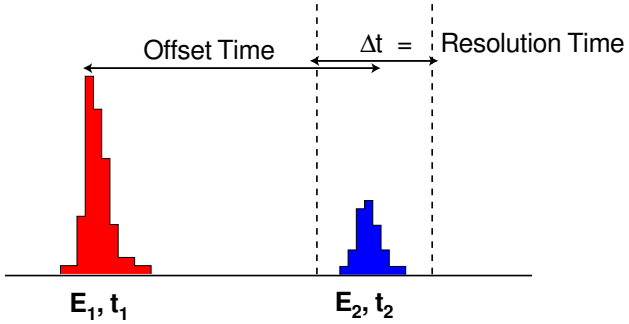
3.2 Pileup Construction

We must consider the case when two (or more) decay positrons hit a calorimeter (close in space and time) within the pulse reconstruction algorithm's time resolution. In that case the overlapping pulses cannot be separated from each other and are treated as a single pulse of higher energy. This effect is called pileup. Pileup can either add events (two lower energy pulses add up to mimic a single higher energy pulse above threshold) or subtract events (two pulses above the energy threshold add up to form a single pulse) from the time spectrum of the decay positrons

above an energy threshold. Since pileup events are pulses with a different g-2 phase,[1], the phase of the pileup events differs from that of the single decay positron events. Therefore, pileup events distort the decay positron time as well as energy spectra and we must apply pileup corrections before extracting the ω_a value.



Pileup: Overlapping pulses cannot be resolved



Probrability of having overlapping pulses is the same as having pulses separated by a small offset time (~10 ns)

Figure 3.1: Method of pileup construction [**?**]

A technique of pileup event construction and thereby pileup subtraction from the time and

[1]The spin precession phase depends on the energy of the positrons as higher-energy positrons traverse a longer path from the decay vertex to the calorimeter and arrive later than lower-energy positrons. Pileup pulses carry the phase information of the lower-energy positrons rather than the phase of the high energy positron that they imitate

energy spectra of the single decay positron events, was developed by Y.Semertzidis, C. Ozben and others [50], [51]. The method is based on the assumption that the probability that two pulses may overlap is the same as the probability that two pulses will be separated by a small time offset (10 ns). The time and energy spectra of the pileup events is constructed by looking at pulses in a "shadow" window[2] (Fig.3.1). If there is a shadow pulse detected within a shadow window, the energies and times of the two pulses are used to construct a pileup spectrum. In this report, we use the pileup construction algorithm derived in [50]. Doubles are basically composed of two decay positron events and events with only one decay positron are called singles. The energies and times of the two singles (trigger pulse and shadow pulse) are used to construct an artificial doubles spectrum whose energy and time is determined by

$$E_D = C(E_1, E_2) \times (E_1 + E_2) \tag{3.1}$$

and

$$t_D = \frac{t_1 + t_2}{2}, \tag{3.2}$$

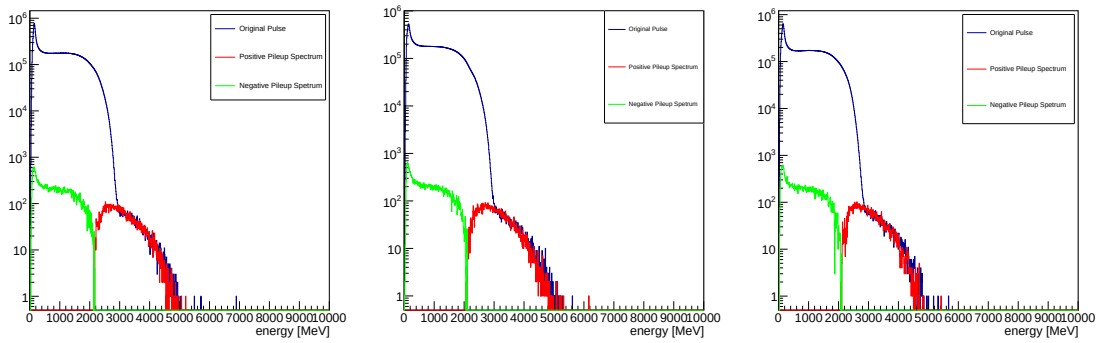
where E_1,t_1 are the energy and time of the trigger pulse respectively and E_2,t_2 are the energy and time of the shadow pulse respectively. $C(E_1, E_2)$ is an energy dependent scale-factor for combining the energies of two single pulses. So far, a ±3ns shadow window around a 10 ns time offset have been used and the value of $C(E_1, E_2) = 1$. After all of the above considerations, four different spectra are constructed OP(Original Pulse), D, S_1, S_2. OP contains all of the events from the calorimeters. The doubles spectrum D(E,t) is constructed by adding the energies of trigger pulses and the shadow pulses. In addition, each of the individual pulses that comprise the pileup events in $D(E,t)$ are separately entered into two histograms of singles S_1 and S_2. A pileup spectrum is constructed as $D - S_1 - S_2$ and a pileup subtracted spectrum is then construted as

$$N(E,t) = OP(E,t) - D(E,t) + S_1(E,t) + S_2(E,t) \tag{3.3}$$

[2]A shadow window is basically a ∼ 1 ns time window around a 10 ns time offset from the initial trigger pulse.

Statistically, Equation 3.3 is equivalent to first completely removing the pileup events from OP by subtracting D, and then adding the events in S_1, S_2 back to the ensemble. The pileup spectra construction is done by following procedures described below:

- Store time, energy and spatial positions of each event in a vector for each muon fill for each calorimeter detector.
- Loop through the vector; look for a second hit within the shadow window (1 ns here) which is 10 ns apart from the first registered hit.
- If there is a shadow pulse found, these two events qualify for a pileup candidate.
- Fill the artificially created pileup energy and time spectra using the information of the above qualified hits.

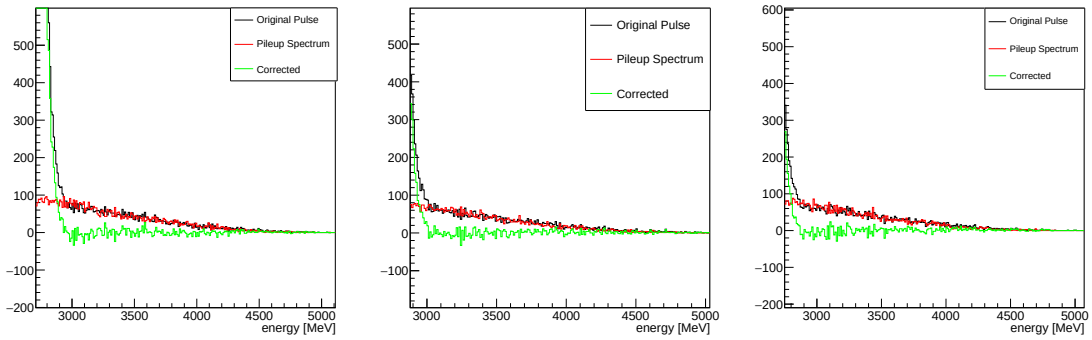


(a) Calorimeter 1 (b) Calorimeter 12 (c) Calorimeter 24

Figure 3.2: The original energy spectra and the pileup spectra for calorimeters 1, 12 and 24

Figure 3.2 shows the energy spectra of calorimeters 1, 12 and 24 before pileup subtraction and the energy spectra of the constructed pileup events (absolute), where only times ranging from 30 to 600 μs after injection have been used. The highest energy that a decay positron can have is 3.1 GeV. The logarithmic scale is used to illustrate the shoulder in OP that starts at about 3.1 GeV and occurs as a result of pileup events. All of the events in OP above 3.1 GeV are mostly from doubles and a few from higher order pileup. Pileup subtraction removes high-energy samples

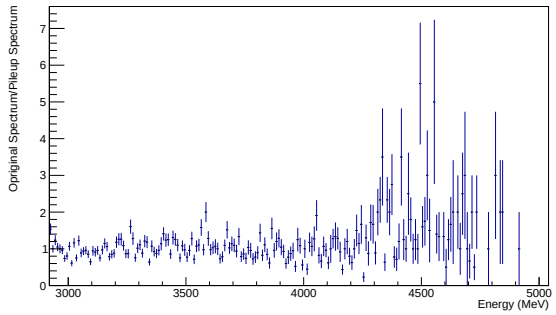
and adds them back at lower-energies. Therefore, at some energy the total pileup contribution is identically zero. We define the pileup spectra as $D(E) - S_1(E) - S_2(E)$, and the absolute of the pileup spectrum is shown in Fig. 3.2



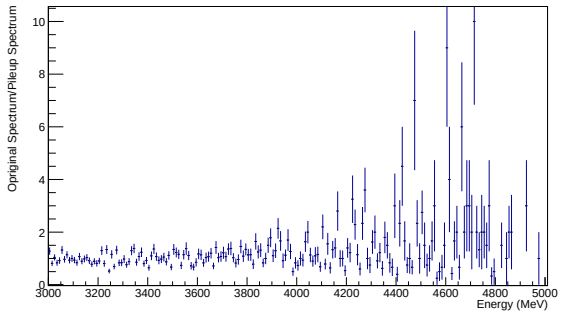
(a) Calorimeter 1 (b) Calorimeter 12 (c) Calorimeter 24

Figure 3.3: Energy spectra for detectors 1, 12 and 24 after pileup subtraction

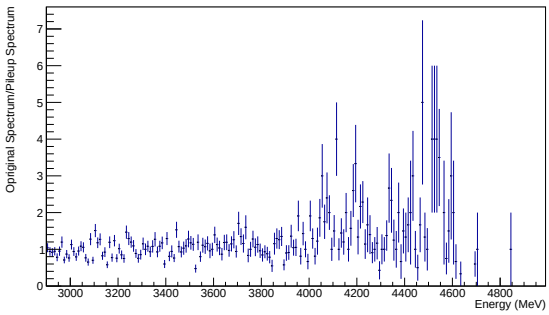
Fig. 3.3 compares the energy spectrum of the original pulse and the energy spectra after pileup subtraction. We can see that there is a slight overcount in the pileup spectrum for calorimeter 1, resulting in a small dip around 3 GeV. In calorimeters 12 and 24 this effect is vanishingly small.



(a) Calorimeter 1



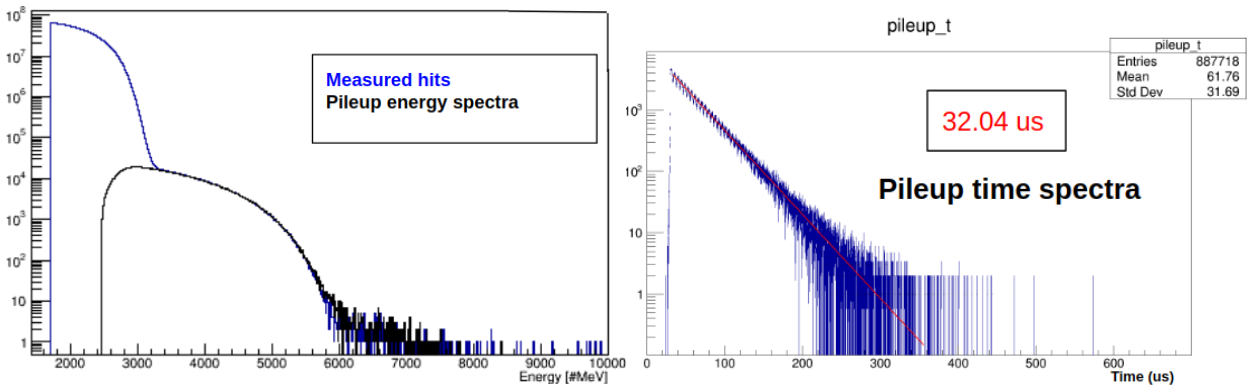
(b) Calorimeter 12



(c) Calorimeter 24

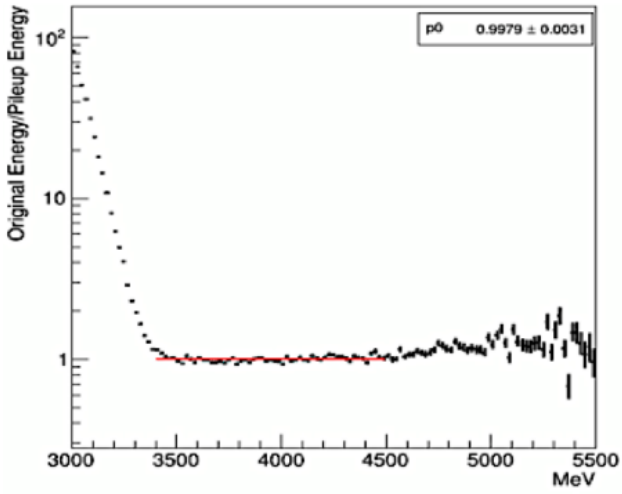
Figure 3.4: The ratio of the original pulse and the pileup spectrum for detectors 1, 12 and 24

Fig. 3.4 shows the ratio of the energy of original pulse and the pileup spectrum. If the pileup spectrum for the doubles match the original pulse in the higher energy region then the ratio of the two should be unity. In Fig. 3.4, we see that the ratio is roughly 1 around 3 GeV to 4 GeV, but above 4 GeV it differs from 1 which indicates a higher order pileup contamination. The pileup energy and time spectra is shown in Fig. 3.5, when we add the events from all the detectors for a subset of Run 2 data agree quite well with our expectation.



(a) Energy spectra for all calorimeters added

(b) Time spectra



(c) Ratio of the measured energy to the constructed pileup energy

Figure 3.5: The energy spectrum of the measured hits and that of the artificially constructed pileup events match very well, indicating good performance of the algorithm. The Pileup time spectrum on the right plot on a log scale is fit to an exponential decay function to verify that the lifetime of these events is half the muon lifetime of 64.4μs. The bottom plot shows the ratio of the measured energy to the pileup energy, again confirming the performance of the algorithm.

Regardless of the consideration of higher order pileup contamination, the systematic error coming from the procedure of pileup correction is well within the error budget of Run 2.

3.3 The Five Parameter Fit

The five parameter fit function used for the ω_a extraction is expressed as

$$N(t) = \boldsymbol{N_0} \cdot e^{-t/\tau} \cdot (1 + \mathbf{A} \cdot \cos(\omega_a(\mathbf{R})t + \boldsymbol{\phi})) \tag{3.4}$$

The bold symbols in Eq. 3.4 are to be extracted from the data. Parameter $\boldsymbol{N_0}$ represents the initial beam intensity, $\boldsymbol{\tau}$ stands for the boosted muon lifetime, the parameter $\mathbf{A}$ depends on the threshold energy and governs the amplitude of the oscillation. The parameter $\boldsymbol{\phi}$ is not physically important, and represents the initial angle of the muon spins with respect to the beam direction.

In order to avoid any bias towards preferring an expected measurement we perform a blind analysis and the value of ω_a is shifted by an offset in ppm level. What we extract from the fit is actually R and not ω_a directly.

$$\omega_a = 2\pi \cdot 0.2291\text{MHz} \cdot (1 + (\text{R} - \Delta\text{R}) \times 10^{-6}) \tag{3.5}$$

The parameter R is blinded in hardware as well as software levels by a C++ blinding library. 0.2291 MHz is used as the reference frequency. a 1 ppm shift in R implies $1 \times 10^{-6} \times 0.2291$ MHz shift in ω_a. ΔR, a secret offset is fixed by the blinding library by each analyzer. ΔR is chosen randomly for each independent analysis from a range of ±25 ppm. There is another layer of blinding protection in the hardware level, that is removed after finalizing all the collaboration wide approved analyses.

3.4 Fit Algorithm

A χ^2 minimization is performed in order to extract the fit parameters in Eq. 3.4. The χ^2 fits are done using the ROOT software package with standard TH1F fit procedures, setting the strategy level to 2. By choosing the strategy level of two, the uncertainties on the fit parameters from the MnMigrad routine are returned by MnHesse, where the uncertainties are calculated by finite difference methods. The data used for the fits are the pileup corrected time spectra. The fits are largely performed in iterations where a set of initial guess values are supplied and the parameters

Parameter	specifications
Fit start time	$30.2\mu s$
Fit end time (data collectedd in 1 hour)	$450\mu s$
Fit end time(whole Run 2 dataset)	$650\mu s$
Fit strategy level	2
Number of fit parameters	5
Blinding Phrase	same for all Run 2 subsets

Table 3.2: Fit specifications used for Run 2 ω_a fits.

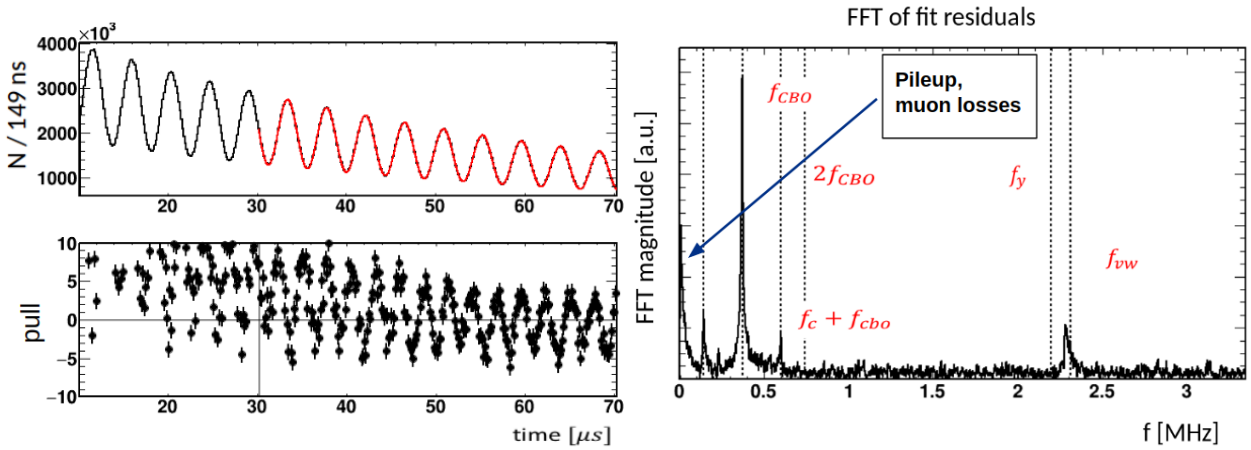
are then allowed to float based on the initial guess; in these iterations sets of parameters are freed, fit and then fixed to the best fit values before pinning down the next group of parameters. The final iteration will have all the parameters freed. The fit start time was chosen to be $\sim 30\mu s$ in order to allow the muon beam to stabilize after injection to the storage ring from the accelerator complex. The exact start time was chosen based on where the time spectra pass through a $g-2$ zero crossing, for the fits shown in this dissertation it was found to be $30.28\mu s$, the BNL measurements showed that some of the systematic errors can be avoided by setting the fit start time to align with the $g-2$ zero crossing.

The parameters used to perform the fit are listed in table 3.3. We choose the same blinding phrase among different subsets of the Run 2 data so that the blinded ω_a are shifted by the same offset and we can use a series of ω_a values for the CPT and Lorentz violation analysis as described in the next chpater without worrying about different offsets causing artifacts or faking a Lorentz violation signal.

The names of the Sequential Access via Metadata (SAM) datasets used for the analyses in this dissertation are listed in table 3.3. SAM is a data handling system used at Fermilab for efficient storage of huge datasets among all the experiments.

Dataset	SAM Name
B	gm2pro_ daq_ offline_ dqc_ run2B
C	gm2pro_ daq_ offline_ dqc_ run2C
D	gm2pro_ daq_ offline_ dqc_ run2D
E	gm2pro_ daq_ offline_ dqc_ run2E
F	gm2pro_ daq_ offline_ dqc_ run2F
G	gm2pro_ daq_ offline_ dqc_ run2G
H	gm2pro_ daq_ offline_ dqc_ run2H

Table 3.3: SAM dataset names used for Run 2 ω_a fits are included for future references of the results presented in this dissertation.

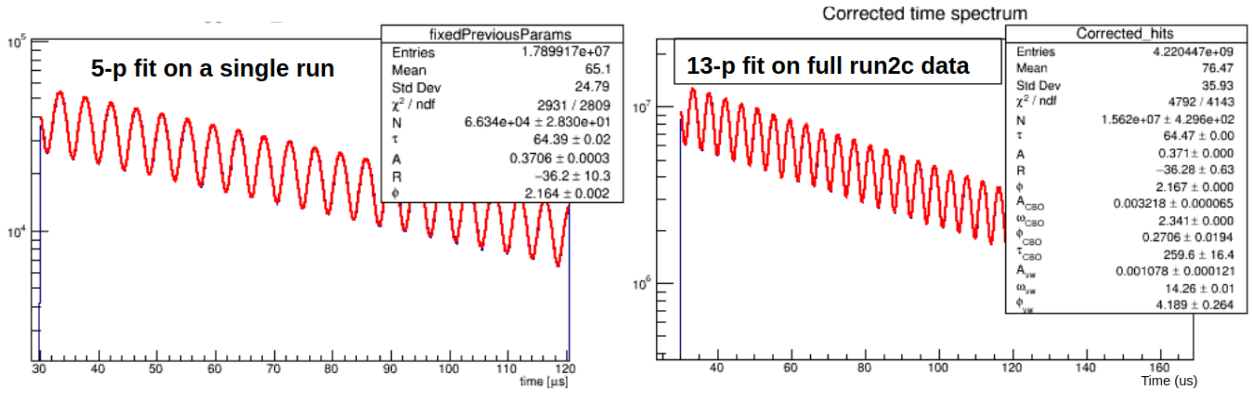


(a) (b)

Figure 3.6: Five parameter fit to one of the subsets of Run 2 data. Left plot shows the fit performed $\sim 30\mu s$ and the corresponding pulls of the fit residuals. The pull shows the case where a fit is performed with a start time extending to $10\mu s$, which shows that the current five parameter fit is insufficient to model the beam motion. The right plot shows a Fourier transform (FFT) of the fit residuals. The clear peaks present in the FFT are expected as we did not account for these motions in the fit function.

Fig. 3.6 shows the fit results from a five-parameter fit to one of the subsets of Run 2 data. There is a clear oscillation present when we plot the pull of the fit residuals. The pull is given by the fit residuals divided by the errors from corresponding bins. As discussed in the previous chapter, the five parameter fit function alone is not sufficient to consider all the beam motions as seen by the detectors. From the FFT of the fit residuals several oscillation frequencies are found, some of which were discussed in the previous chapter. All of the peaks in the FFT are at expected locations,

which makes it easier to include more fit parameters and extend the five parameter model in order to account for all of these beam motions. The dominant oscillation frequency comes from the CBO effects. The presence of a peak at the zero frequency comes from the slow effects, such as pileup effects. Since the primary motivation behind extraction of ω_a is to use the time series of ω_a for the CPT and Lorentz violation search, it is sufficient to consider only the five parameter fit function. We do not lose sensitivity by doing this as the effects not modeled by the five parameter fit do not vary from one subset of data to another. Technically the fit will fail to converge if we try to model all the beam frequencies while extracting ω_a from only 1 hour duration of data taking due to low statistics, as these effects are hardly visible for such a small duration of data taking.



(a) 5 parameter fit on 1 hour duration of data

(b) 13 parameter fit on a larger subset of Run 2 data

Figure 3.7: The left plot shows the fit parameter values when a five parameter fit was performed on 1 hour duration of data. The best-fit values of R for Run 2 are still blinded. The right plot shows a 13 parameter fit on a relatively larger subset of Run 2 data where some of the beam frequencies were modeled and hence extending the five parameters to Thirteen.

Fig. 3.7 shows that the χ^2/ndf of the fit for a single run, i.e., extracting ω_a from just 1 hour duration of data is $\sim$ 1.04. The blinded precession frequency extracted from the five parameter fit functions for each run will be used in the next chapter for a CPT and Lorentz violation search.

CHAPTER 4

CPT AND Lorentz Invariance Violation Tests

The $g-2$ data also provides a great opportunity for setting the most stringent limits on some of the Standard Model Extension CPT LV parameters in the muon sector. The current best limits on some of the CPT and LV signatures in the muon sector come from the BNL Muon $g-2$ Experiment [52], reaching limits of $\sim 1.4 \times 10^{-24}$ GeV on coefficients of SME Lagrangian terms. The CPT and Lorentz violating signatures that we can look for using $g-2$ data are: a sidereal variation of $\omega_a(t)$ and a μ^+/μ^- ω_a difference, $\Delta\omega_a =< \omega_a^{\mu+} > - < \omega_a^{\mu-} >$. Extensive simulation studies confirm that the sensitivity regarding the sidereal varation roughly scales with ω_a uncertainty. Hence, the $g-2$ experiment at FNAL should be able to reach limits of $\sim 5 \times 10^{-25}$ GeV. Two analysis techniques are used in the framework for a sidereal oscillation signal search in the $g-2$ data: the Lomb-Scargle (LS) test, a unique spectral analysis technique for unequally spaced data, a direct multi-parameter fit (MPF) to the data. The two approaches give results in agreement. There is no significant signal found in this search. This chapter includes a detailed discussion of the sidereal search using the Fermilab g-2 Run 2 data.

4.1 R_μ Instead of ω_a

The frequency ω_a is proportional to the magnetic field and therefore to $\tilde{\omega}_p'$, so the sidereal variation of $R_\mu = \omega_a/\tilde{\omega}_p'$ is analyzed, rather than ω_a directly. The variations of the magnetic field affects ω_a measurements as well since we measure ω_a in presence of the external magnetic field. The main magnet is powered by a low-voltage power supply providing $\approx$ 5200 A which can be regulated to 0.3 ppm, and an NMR feedback provides 0.1 ppm stability. So the magnetic field used in the $g-2$ experiment is not exactly a constant depending on how small a CPT and LV signal we

are looking for. Hence, the magnetic field is taken into account in the analysis by using R_μ. The other factors that could cause a variation in the magnetic field are, for example, thermal expansion of the steel in response to temperature changes in the experimental hall. The day-night temperature change could fake a sidereal variation signal in $\omega_a(t)$. Therefore by taking the ratio of the two measured frequencies we can avoid many artifacts of the data that could otherwise cause potential backgrounds in the analysis. An upgraded hall temperature control system, with a precision of $\pm 1°$C was installed in 2019 to provide a stable thermal bath for the experiment.

One of the concerns while considering R_μ to search for the signal is the possibility of cancelling the potential sidereal oscillations present in both the frequencies with similar amplitudes. However the clock-comparison experiments set a limit on $\tilde{\omega}'_p$ that is negligible, and hence any potential sidereal oscillation in R_μ will stem from a potential signal in ω_a. This dissertation confirms that the amplitude of a potential sidereal signal in $\tilde{\omega}'_p$ is negligible compared to that in the ω_a data. The field measurements used in this analysis are provided by S. Corrodi. This chapter provides the first limits from the Fermilab Muon $g-2$ experiment on both the precession frequencies and the ratio.

4.2 Ingredients for The Sidereal Search

The Fermilab $g-2$ experiment uses GPS systems that provide unix time-stamps for each event unlike the previous experiment at BNL. Several atomic clocks in GPS satellites provide very precise time data to the GPS signals. These signals are decoded by GPS receivers and each receiver is synchronized to the atomic clocks. The hyperfine transition between the ground states of ^{87}Rb can be attributed for atomic clocks. The $0 \rightarrow 0$ transitions between F = 2 and F = 0 of the ground state are insensitive to the orientation of the clock, and hence to any potential Lorentz violation effects, where F corresponds to the total angular momentum quantum number.

The Muon $g-2$ clock system is driven by two GPS antennas, mounted to the roof of the experimental hall, one manufactured by Stanford Research Systems (SRS), the other by Meridian. The GPS antennas send 1 pulse per second (PPS) signals over two independent cables to two

separate receivers. The antennas and the receivers are connected to two sets of clocks, that contain internal Rubidium Oscillators, which ensure short-period stability, while the GPS signal ensures long-period stability [53].

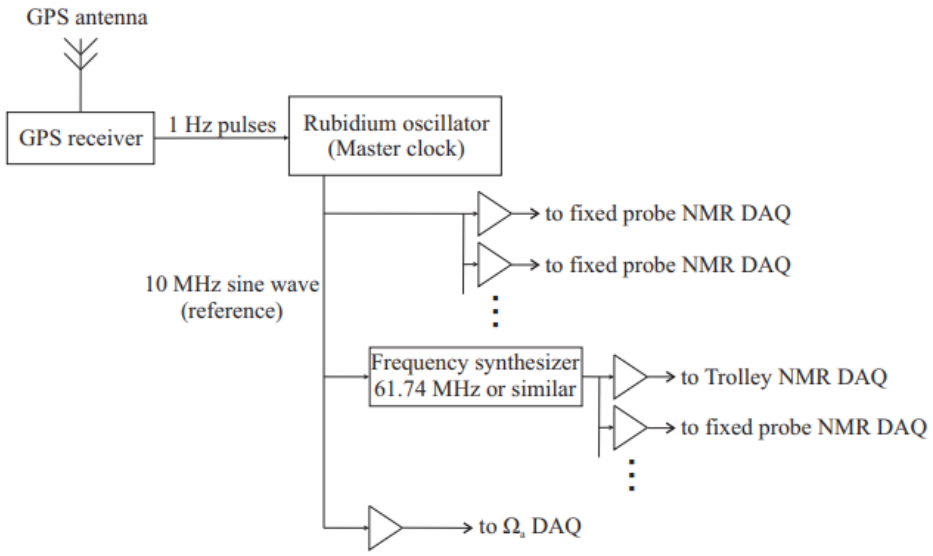


Figure 4.1: The schematic of the clock system used in the experiment [36].

The knowledge of time stamps of all events provides a lot of opportunity to test the data using various other methods. The data are binned in two ways in time: evenly sampled and unevenly sampled. Even sampling refers to the data folded over equally spaced time bins, whereas the "Unevenly" sampled data refers to binning the data on a run-by-run basis, where the time bins are of different sizes. For each time bin, ω_a and $\tilde{\omega}'_p$ are calculated. We apply two methods on the time series of $R_\mu (= \omega_a/\tilde{\omega}'_p)$ for a sidereal search: the multi-parameter fit (MPF) and the Lomb-Scargle (LS) test. A detailed analysis on 2019 Run 2 data, both evenly sampled, folded and unevenly sampled, run-by-run data are included in the following sections.

4.3 Time: One of the Key Ingredients

The basic periods of data collection are called "runs" which last approximately 1 hour. The runs consist of several subruns, which contains seven seconds of data collection each. The median of the time stamps of all the subruns within a run was assigned as the unix time stamp of that run

for a run-by-run data analysis. In order to sample the data in evenly spaced time bins we need to determine the time stamp of each event; where an event qualifies for each positron hit in the calorimeter above a threshold energy. For each positron event the unix time stamp is given by,

$$t = t_{subrun} + t_{fill} + t_{g-2} \tag{4.1}$$

where t_{subrun} is the unix time stamp at the beginning of a given subrun, t_{fill} is the fractional time of each muon fill (discussed in chapter 2) within that subrun relative to t_{subrun}, and t_{g-2} is the time of the positron usually used in the ω_a analysis within each $700\mu s$ muon fill. The time stamps for the run-by-run analysis used in this dissertation are shown in Fig. 4.2.

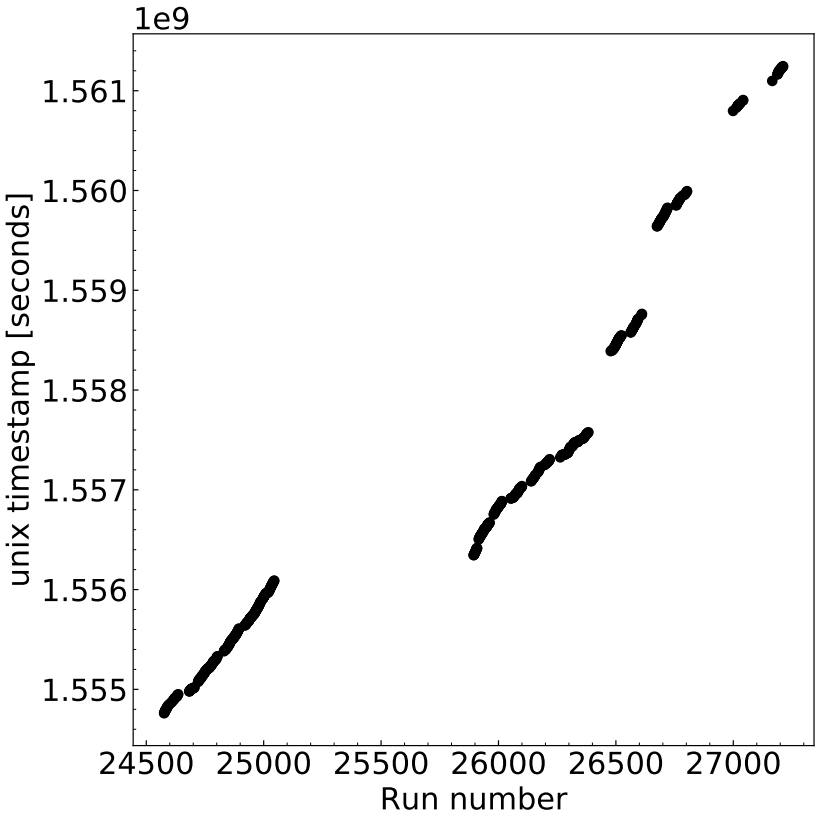


Figure 4.2: Figure shows the unix timestamps for each run in the Run 2 dataset after applying the data quality cuts.

4.3.1 The Sidereal Time

The signal that we are looking for in the data is an oscillation with a period of sidereal time. The sidereal time, widely used by astronomers for locating celestial objects, is the period of the earth's rotation about its axis relative to the fixed stars, rather than relative to the sun. By the time the Earth spins once about its axis, it has already moved along its orbit by over 2.5 million kilometers. Hence the sun will not appear in the same part of the sky at the end of that rotation. The earth has to rotate for another four minutes in order to return to the same position in the sky. So the actual period of rotation of the Earth relative to the distant stars, i.e. the time for the Earth to spin 360 degrees, is less than one solar day. So one sidereal day is,

$$T_s = 24 \times 60 \times 60 \times \frac{360}{360 \times (1 + \frac{1}{365.25})} = 86164.09 \text{ seconds} \tag{4.2}$$

One solar day is,

$$T_d = 24 \times 60 \times 60 \times 60 = 86400.00 \text{ seconds} \tag{4.3}$$

The experiment records unix time to denote the time of each positron event detected by the calorimeters. Unix time is the number of seconds advanced since the Unix epoch, minus leap seconds; the Unix epoch was set at 00:00:00 UTC on 1st January 1970.

4.4 Data Selection Criteria

The 2019 Run 2 dataset was used for this analysis. While the pulsed systems, the ESQs and the kickers, were held stable throughout Run 2 unlike Run 1, there were 5 day beam on 9 day beam off periods that affected the stability of the storage ring magnet. Also, the temperature control of the experimental hall was lost towards the end of Run 2 and this in turn caused some spurious peaks in the spectral analysis, that will be discussed later in this chapter. The full dataset was divided into smaller subsets and labeled as 2B to 2H chronologically.

The pulsed HV systems experienced frequent disruptions from dielectric breakdown due to the non ideal storage ring vacuum conditions that caused the HV systems to spark. Furthermore,

Dataset Name	Date	High energy e^+
B	April 4 - April 9	0.8×10^9
C	April 11 - April 24	4.19×10^9
D	April 27 - May 11	3.41×10^9
E	May 20 - May 25	1.045×10^9
F	June 4 - June 8	1.22×10^9
G	June 17 - June 19	0.134×10^9
H	June 21 - June 22	0.348×10^9

Table 4.1: Number of high energy positron events in each of the Run 2 subsets that qualified for the analysis.

muon bunches with irregular profile measured by the T0 counter were sometimes delivered by the accelerator complex. These were taken into account by applying data-quality cuts to each data set's muon fills to select only the most stable ones for analysis. This avoids introducing possible systematic ω_a-biases. The energy cut applied to select the high energy e^+s was 1.7 GeV and the data used for this analysis are pileup corrected and gain shifted.

4.5 Analysis Techniques

A sidereal variation in ω_a can be expressed as $\omega_a(\omega_{pi}, t_i) = K\omega_p(t_i) + A_\Omega cos(\Omega t_i + \phi)$. In terms of the ratio $\mathcal{R}$,

$$\mathcal{R} = K + \frac{A_\Omega}{\omega_p(t_i)} cos(\Omega t_i + \phi) \tag{4.4}$$

where K is a combination of μ_p and μ_m, and A_Ω represents the amplitude of the sidereal variation. Two analysis techniques were used to extract oscillation signal from the the g-2 data: a direct multi-parameter fit to Eq.(4.4), and the Lomb-Scargle test, a unique spectral analysis technique for unequally spaced data.

The Multi-parameter Fit Method

The oscillation amplitude can be obtained by performing a multi parameter fit to the time series of $\mathcal{R}$. The amplitude of a possible oscillation is minuscule as the ratio $\mathcal{R}$ is known to be

essentially constant with respect to time. The 4-parameter function used for the least square fit to the data is:

$$\mathcal{R}(t) = C_0 + A_0 cos\left(\frac{2\pi t}{T_0} + \phi_0\right) \tag{4.5}$$

The oscillation amplitude is given by A_0. The four-parameter fit will be used to find the oscillation amplitudes.

The Lomb-Scargle test

The Lomb-Scargle test is a spectral analysis technique, uniquely designed for detecting signals when the data are unequally spaced [54], [55]. This method is widely used for astronomical observations. With evenly sampled data it reduces to the usual Fourier analysis. For the time series y_i with $i = 0, ...N-1$, the normalized Lomb power P_N at frequency ω within a search range is given by,

$$P_N(\omega) \equiv \frac{1}{2\sigma^2}\left\{\frac{[\sum_i (y_i - \bar{y}) cos[\omega(t_i - \tau)]]^2}{\sum_i cos^2[\omega(t_i - \tau)]} + \frac{[\sum_i (y_i - \bar{y}) sin[\omega(t_i - \tau)]]^2}{\sum_i sin^2[\omega(t_i - \tau)]}\right\} \tag{4.6}$$

where $\bar{y}$, σ and τ are given as,

$$\begin{aligned} \bar{y} \equiv \frac{\sum_i y_i}{N}, \sigma^2 \equiv \frac{1}{N-1}\sum_i (y_i - \bar{y})^2 \\ tan(2\omega\tau) \equiv \frac{\sum_i sin(2\omega t_i)}{\sum_i cos(2\omega t_i)} \end{aligned} \tag{4.7}$$

The frequency range for the Lomb-Scargle test is $[0, F_c]$, where F_c is the nyquist frequency, and is given by $F_c = \frac{N}{2T}$ (T being the observational baseline for the analysis). The frequency range used for the run-by-run data in this report is $[0, 5F_c]$. The higher the value of P_N, the Lomb power, the more significant the periodic signal will be at ω. Hence, the Lomb-Scargle test provides the frequency information of a potential oscillation signal within the search range. The uncertainty in the estimated frequency of the LS periodogram is a very important aspect of the measurement and the uncertainty can be expressed in terms of the height of the peak w.r.t the background peaks that

appear in the periodogram. The significance of a peak in the spectral analysis is interpreted in terms of the False Alarm Probability (FAP), which is a measure of the probability that the data consisting of Gaussian noise with no periodic signal would lead to similar peak amplitude (or higher) due to the noise in the data. Hence, a small FAP value is indicative of the presence of a significant periodic signal in the data. For M independent frequencies within the search range, the FAP for a Lomb power, P_N is given by,

$$1 - (1 - e^{-P_N})^M \tag{4.8}$$

The number of independent frequencies within the search range can be obtained by Monte Carlo simulations. The standard approach only considers the highest peak for FAP estimation; I have incorporated a generalized statistical approach by which we can estimate the significance of any peak of any amplitude appearing in the LS spectra.

4.6 Run-by-Run Data Analysis

The first step in the CPT analysis is extracting the precession frequency for each run by performing a 5 parameter fit on the pileup corrected time spectra from the calorimeter detectors along with calculating the average magnetic field, $\tilde{\omega}_p'$. The combination of ω_a and $\tilde{\omega}_p'$ then gives R_μ as a function of time; where each run is assigned to a unix timestamp as described in 4.3. Some of the runs were excluded because of their low statistics even though they passed the usual data quality cuts. 640 runs from the Run 2 data were available for this analysis. Figure 4.3 shows the time series of the precession frequency, the shielded proton frequency and the ratio R_μ on a run by run basis.

4.6.1 Lomb Scargle Test

From Fig. 4.3 the unequal spacing of the data points can be clearly seen. So, in order to switch from the time domain to the frequency domain we applied a sophisticated spectral analysis technique, known as Lomb-Scargle test, that is widely used in astronomical observations. Fig. 4.4a shows the spectral power, P_N over a frequency range, where we scan frequencies and calculate

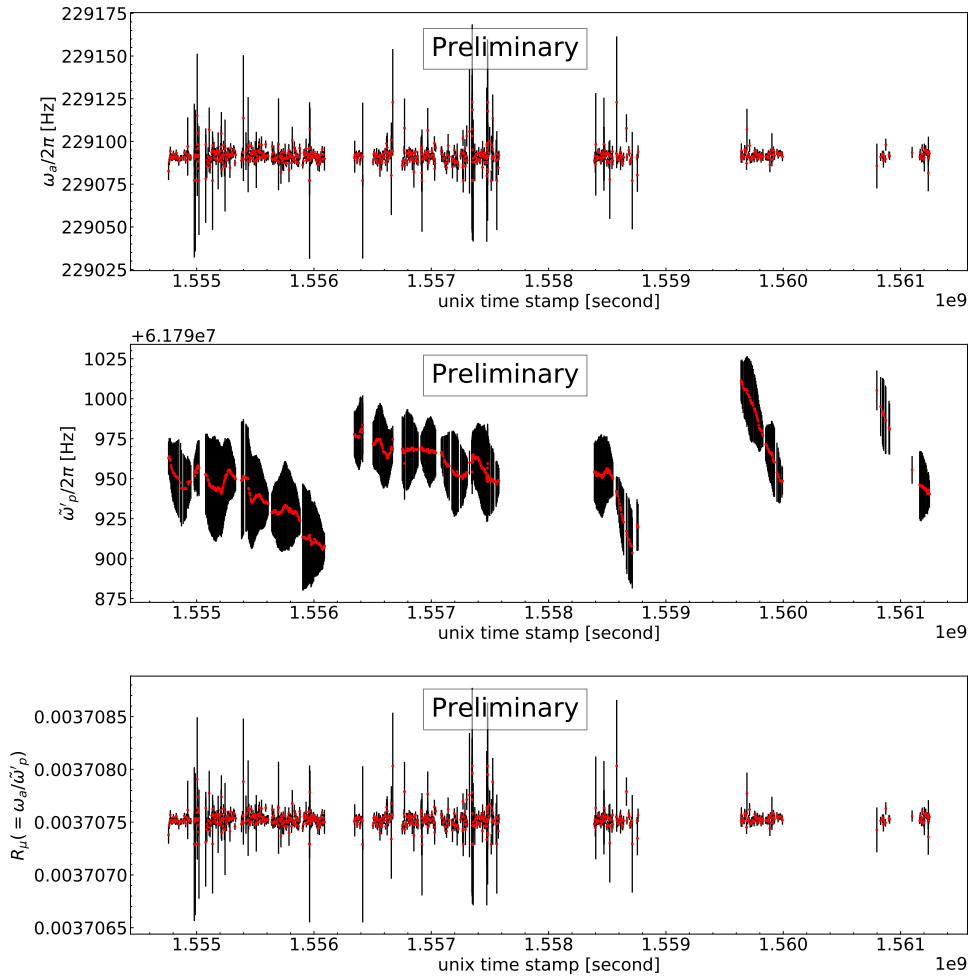
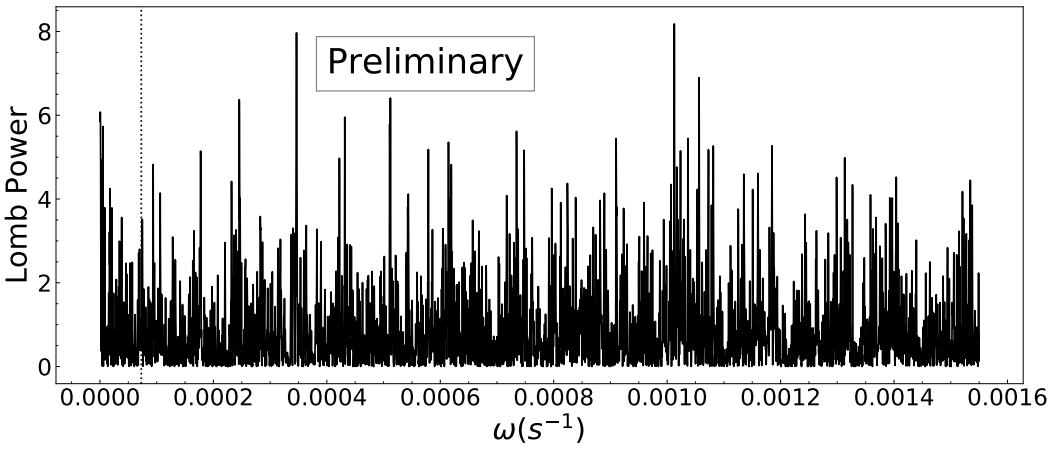
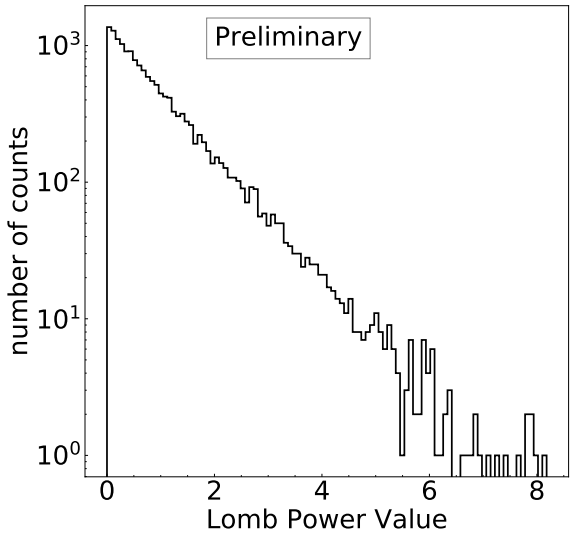


Figure 4.3: Time series of ω_a, $\tilde{\omega}'_p$ and R_μ on a run by run basis respectively.



(a) Spectral power plot for run by run data



(b) Distribution of Lomb power

Figure 4.4: The spectral analysis plots on a run by run basis for Run 2 data. Left plot: the Lomb power, $P_N(\omega)$ over a frequency range shows that there is no significant peak present at the sidereal frequency. Right plot: the distribution of $P_N(\omega)$ over all the frequencies scanned follow an exponential decay confirming the absence of a potential significant oscillation signal

$P_N(\omega)$ at each frequency, ω. The peaks in Fig. 4.4a represent $P_N(\omega)$, which is a measure of the statistical significance of a potential signal with frequency of oscillation ω. The higher the peak the more significant the oscillation signal at that ω is. Here the frequency range is chosen to be $[0, 5\mathrm{F_C}]$, where $\mathrm{F_C}$ is the average nyquist frequency. The nyquist frequency depends on the observational baseline, i.e, the duration of the data taking period and the number of data points. For instance the Run 2 data was taken over a period of 3.5 months and 640 runs qualified for the analysis, making $F_C = N/2T = 4.93 \times 10^{-5}$ Hz. The frequency grid for the analysis was optimized based on the average nyquist frequency and an over sampling factor set by the analyzer. With the over sampling factor to be 10, 16000 frequencies were scanned for the Run 2 data set. Although the search is for a potential signal at the sidereal frequency, we search over a broad frequency grid to ensure that the analysis method is robust and free of any artifacts or biases that could mimic or compromise a signal measurement at our region of interest. The highest peak arises at $0.0010s^{-1}$ with a peak height ~ 8. The Lomb power at the sidereal frequency is 0.86, and the probability of this value arising from a potential oscillation signal is negligible. Moreover, the Lomb power distribution in Fig. 4.4b follows an exponential decay which is indicative of the absence of a significant signal, discussed in more detail in appendix. For further investigation, the 640 data points are divided into two slices; the first half consists of the first 300 data points and the second half has the rest 340 data points. Lomb Scargle test is then applied on these subsets. Fig. 4.5 shows the spectral power for each of the above three cases. The position and height of the highest peak while analyzing the whole dataset changes when only a subset is considered. Additionally, a peak at the sidereal frequency also pops in and out of existence depending on which part of the whole dataset we choose for the analysis. This confirms that the peak at ω_s is due to statistical fluctuation. We do not see a consistent appearance of a significant peak at any of the scanned frequencies suggesting that there is no significant oscillation present at any of the frequencies scanned.

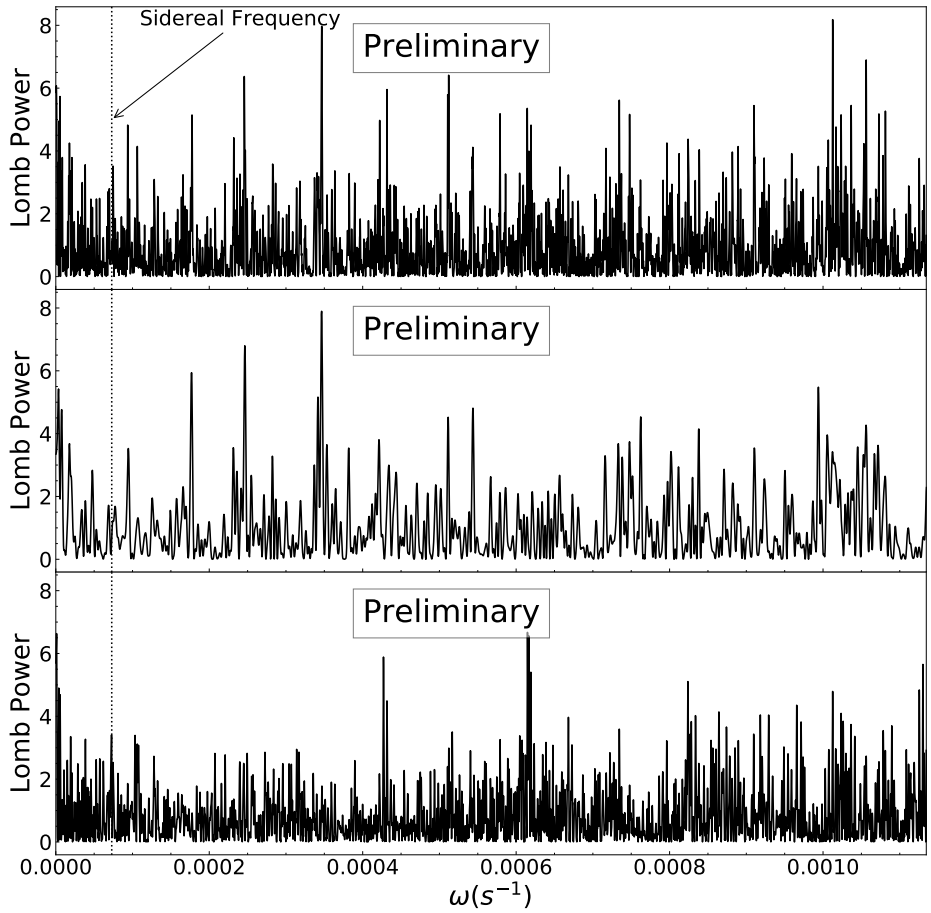
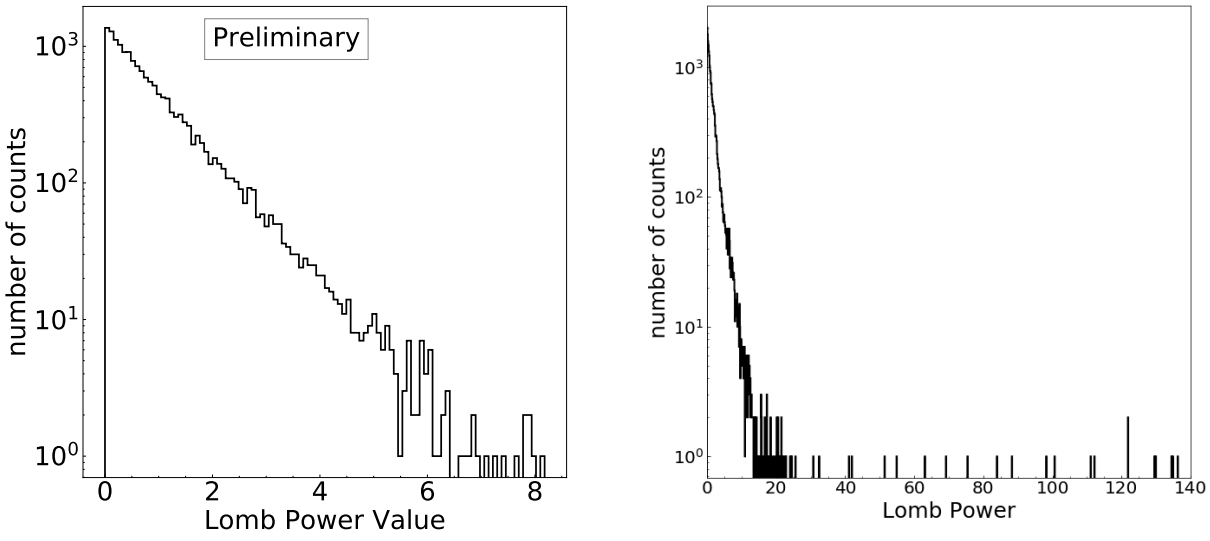


Figure 4.5: Figure shows spectral analysis plots on preliminary Run 2 data. The top plot shows spectral power as a function of frequencies when the analysis was performed on the full Run-2 dataset. The middle and the lower plot shows the spectral power as a function of frequencies when the analysis was performed on partial subsets of the data in order to investigate the overall structure of various peaks.



(a) (b)

Figure 4.6: Comparison of Lomb power distributions. The left plot shows the Lomb power distribution for an input data with no significant signal. The right plot on the other hand shows the power distribution when we injected a 10 ppm false signal. The Lomb power distribution in the right plot extends to a much higher value, indicating the presence of a strong signal.

4.6.2 Sensitivity of the algorithm

In order to gauge the sensitivity of the Lomb-Scargle test for a given observational baseline, the performance of the algorithm is studied over an ensemble of simulated datasets. The simulated data are generated based on the inputs from the real data; the unix timestamps of the Run 2 data are used and the data points for each of these timestamps are generated randomly from a normal distribution with the central value to be the average R_μ from Run 2 and the standard deviation of the each individual data points. The range of the maximum Lomb power that we would expect for a given dataset with no signal can be determined by applying the Lomb-Scargle test on an ensemble of simulated data groups. For instance, Fig. 4.6a shows a maximum Lomb power of about 10 for one dataset; now by performing the analysis on 10000 such cases and storing the maximum Lomb power each time, we get the distribution shown in the top plot of Fig. 4.7. This plot gives a handle on the range of maximum values extending to a spectral power of 15; meaning that with

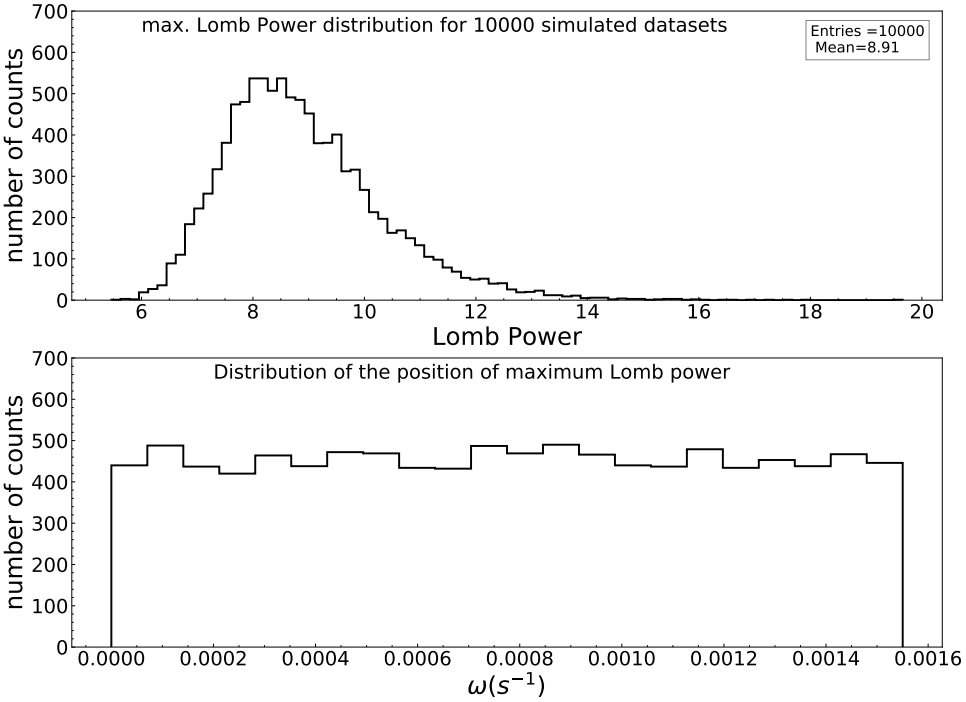


Figure 4.7: The Lomb-Scargle test performed on an ensemble of simulated data with no signal added. The distribution of the maximum Lomb power shows that the range of peak heights stretches out to 15 even when there is no signal present. The frequency positions of the highest peaks are randomly distributed confirming that the algorithm is not biased towards a particular frequency over the other within the search range.

the Run 2 data spacings we can expect a peak as high as 15 even when there is no significant signal present in the data. The Lomb power distribution has a long tail stretching out to a much higher value when we add an artificial signal of 10 ppm to the simulated data, and no longer follows an exponential decay indicating the presence of a potential signal, as shown in Fig. 4.6b. The mean of the distributuion of maximum Lomb power also shifts to the right as anticipated when we add an artificial signal at the sidereal frequency. The bottom plot of Fig. 4.7 shows the distribution of the corresponding frequency positions of the maximum Lomb power for each data group; a flat distribution for the cases with no artificial signal reinforces that the algorithm is not biased towards a particular frequency within the frequency grid, whereas the distribution is peaked around

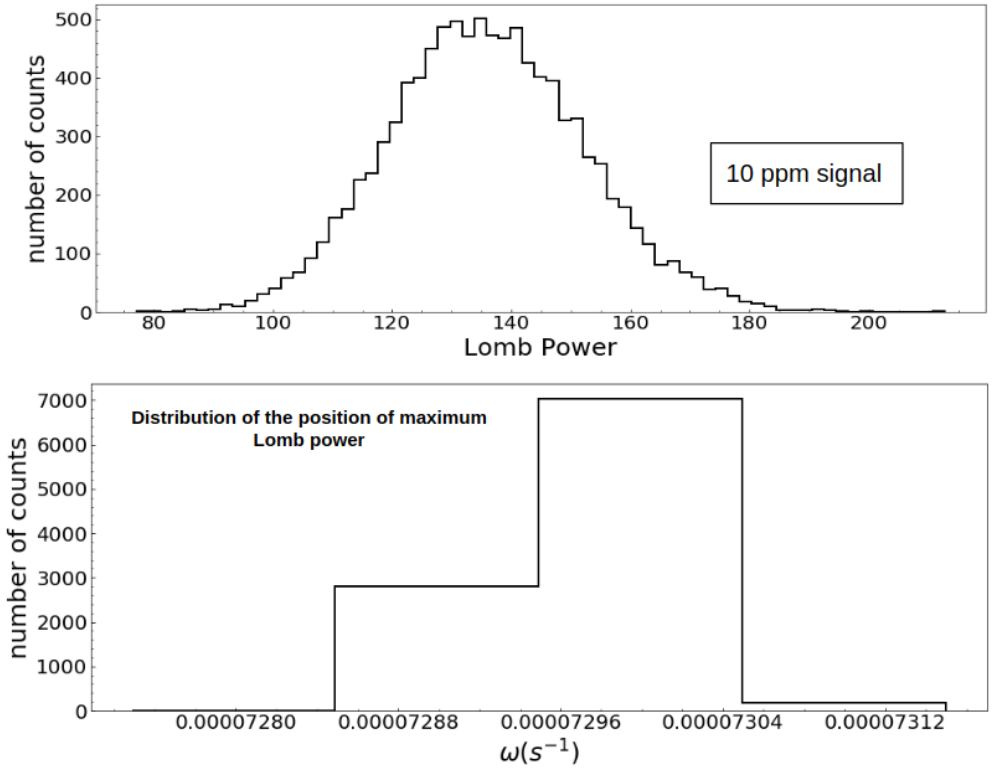
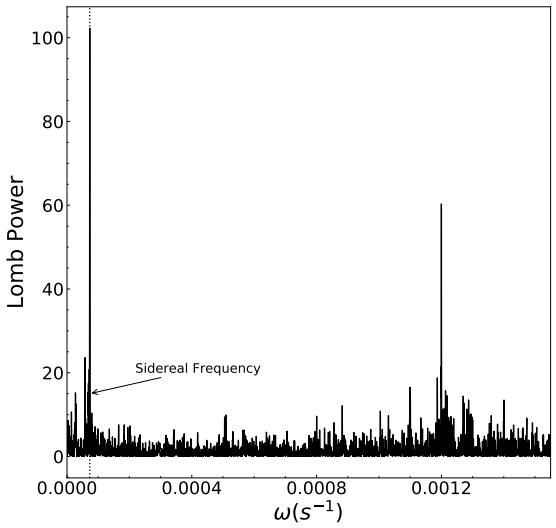


Figure 4.8: The Lomb-Scargle test performed on an ensemble of simulated data with 10 ppm signal added at the sidereal frequency. The distribution of the maximum Lomb power shows that the range of peak heights shifts to the right when there is a significant signal present as compared to the no signal scenario. The frequency positions of the highest peaks are no longer randomly distributed rather the distribution now peaks near the frequency of the input signal confirming that the algorithm is able to detect a significant signal

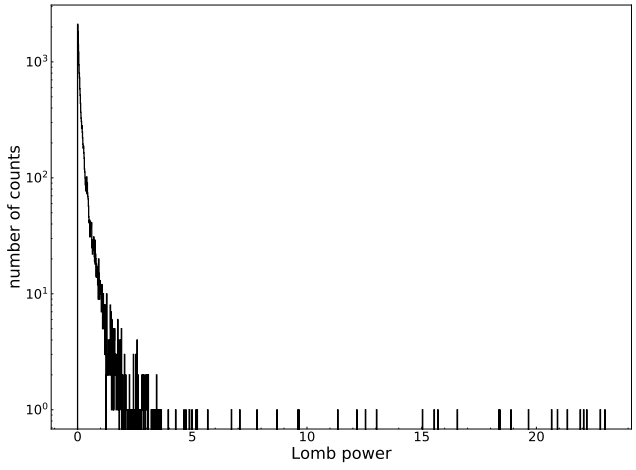
the sidereal frequency for the cases when we added an artificial signal of 10 ppm at the sidereal frequency, as shown in the bottom plot of Fig. 4.8. The position of the peak landing at the same frequency bin depends on the statistical fluctuation of the data as well as how strong the injected artificial signal is. The top plot of Fig. 4.8 shows that the mean of the distribution of the maximum Lomb power shifts to a much higher value when a 10 ppm signal was added to the simulation samples.

Initially several sensitivity studies were done to understand the performance of the algorithm for the given Run 2 data specifications, such as the time range of Run 2 and the individual uncertainties on each data point, which is $\sim$ 10 ppm. The sensitivity studies presented here are done on simulated data to study various effects such as the performance of the algorithm to artificially injected signals, estimating the resolution of the peak positions and comparing the results of different methods.

Lomb-Scargle test is a very sensitive spectral analysis technique. Two 4 ppm signals are added at the sidereal frequency and a randomly chosen frequency of $0.0012s^{-1}$ with the data point uncertainty as that of the real Run 2 data. Fig. 4.9a shows the power spectrum when we ran the analysis on a simulated dataset containing these two signals; the power spectrum shows clear peaks at the expected frequencies. Now if we look at the corresponding Lomb power distribution, as shown in Fig. 4.9b, it clearly does not follow an exponential decay, reinforcing the fact there is a significant oscillation present in the input data. Furthermore, to gauge the behavior of the Lomb-Scargle test we generated simulated datasets with lower uncertainties and studied the performance of the algorithm. Here the simulated data were generated from the normal distribution with the average value of R_μ as before but with individual data point uncertainties scaled by factors of 2, 5 and 10; i.e., we generated the simulated data based on the data point uncertainties δR_μ, $\delta R_\mu/2$, $\delta R_\mu/5$ and $\delta R_\mu/10$ and then used these individual data sets to study the sensitivity of the Lomb-Scargle test. For these uncertainties we injected the same 4 ppm signals at the sidereal frequency and at $0.0012s^{-1}$ as before. From Fig. 4.10a, and Fig. 4.10b it is evident that the sensitivity of the algorithm scales with the individual data point uncertainties. The uncertainties on the data points

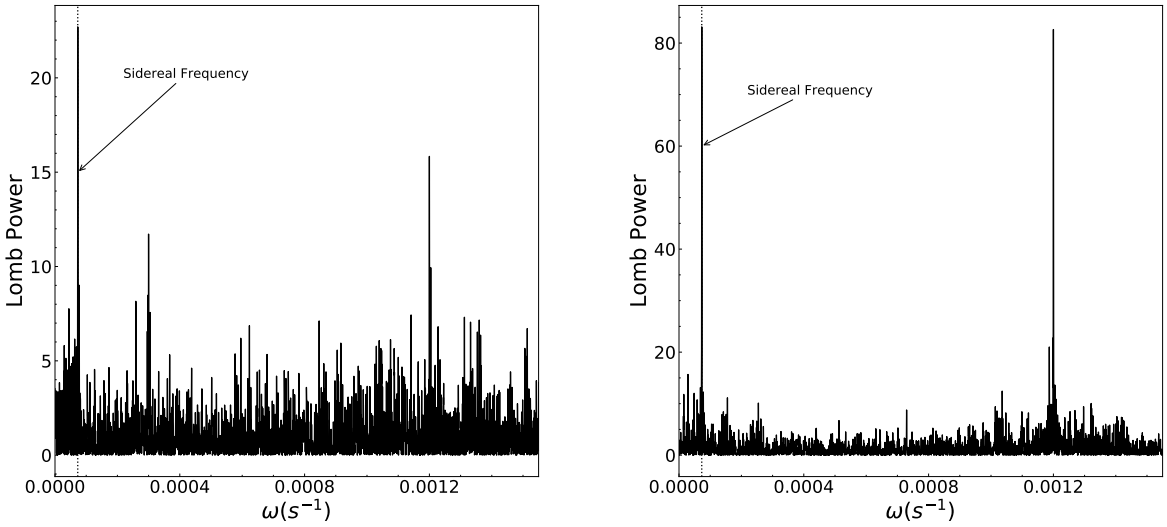


(a)



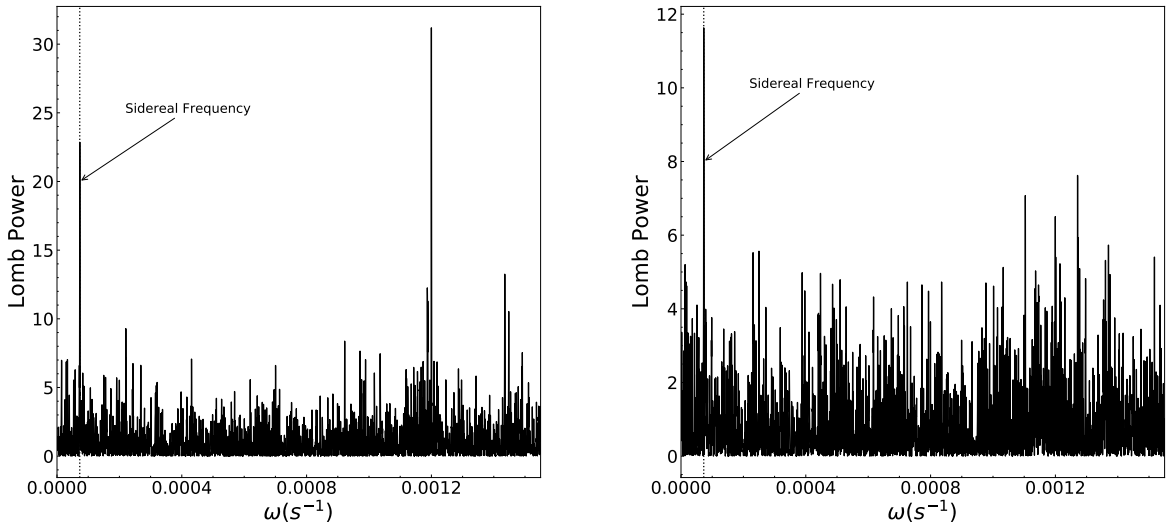
(b)

Figure 4.9: Performance of the Lomb-Scargle test. The left plot shows the power spectrum when we added two 4 ppm signals with the data point uncertainties δR_μ to the average of the data points, hence excluding some of the gaussian noise. The spectral power plot behaves as expected. The right plot shows the corresponding Lomb power distribution, which now deviates completely from an exponential decay, indicating a presence of pure oscillation components in the data. Note that the x-axis is truncated in this plot to emphasize the decay deviating quite a lot from that of an exponential nature.



(a) (b)

Figure 4.10: Sensitivity of Lomb-Scargle test. Left plot: simulated data generated with individual data point uncertainty, and then two signals of amplitude 4 ppm are added simultaneously at the sidereal frequency and at $0.0012s^{-1}$. Right plot: simulated data generated with individual data point uncertainty as $\delta R_\mu/2$, with false signals of 4 ppm injected at the same frequencies as before. The right plot shows clear huge peaks at both the frequencies as the SNR improves quite a lot. We see that the sensitivity of the algorithm scales with the uncertainties on R_μ. The more statistics we accumulate as we move forward with the $g-2$ experiment the smaller the uncertainties on individual data points and hence the more sensitive the algorithm will be.



(a) (b)

Figure 4.11: Lomb-Scargle test on simulated data generated with individual data point uncertainties set to $\delta R_\mu/2$, with two artificial signals added at the sidereal frequency and at a randomly chosen frequency of $0.0012s^{-1}$. The left plot shows the power spectrum when the false signal amplitudes are 2 ppm. The right plot shows the spectrum when two 1 ppm signals are added. The peak amplitudes are much more significant for the 2 ppm signals compared to the 1 ppm case. The peak from the signal injected at $0.0012s^{-1}$ is almost smeared by the noise in the right plot and the spectral leakage is much more prominent in this case.

may wash out a potential signal depending on the size of the signal compared to the uncerntainties. The smaller data point uncertainties correspond to a power spectrum more sensitive to smaller time variations. The signal amplitude must be comparable with the data point uncertainties in order for the algorithm to be able to detect a signal component significantly. The peaks arising from the signal will be smeared in the noise if the uncertainties are relatively large, and the algorithm will not be able to detect the potential signal.

Since we see that the sensitivity of the Lomb-Scargle test strikingly improved with a data point uncertainty of $\delta R_\mu/2$, it should be more sensitive to a smaller amplitude signal with this uncertainty. A simulation study is performed to confirm this; by adding various amplitudes. Adding artificial signals with 2 and 1 ppm amplitude respectively with a data point uncertainty of

$\delta R/2$ results in distinguishable peaks at the input frequencies. Notice that the signal to noise ratio is better in the first case where we added two 2 ppm signals to the simulated data. The spectral leakage to nearby frequency bins is more prominent in the second plot where two 1 ppm signals are added at the frquencies mentioned before, this will be discussed in more detail in Sect. 4.9. The above simulation studies give an estimate on what to expect from the Lomb-Scargle test and how the sensitivity scales with the R_μ uncertainty as well as the potential signal's amplitude. The outcome of these studies heavily depends on the characteristics of the dataset being used. So the sensitivity is may change for Run 3 based on the parameters such as, the length of the observational baseline, the spacing of the data points and the statistical uncertainties on each data point.

4.6.3 Multi Parameter Fit Results

A multi-parameter fit to the data gives us the amplitude of any potential oscillation. In absence of a sidereal oscillation we expect R_μ to be a constant in time, and the amplitude of a potential signal is small compared to the constant part of $R_\mu(t)$. The oscillation amplitude is obtained by performing a least-square fit to the data. Fig. 4.12 shows the Run 2 data fitted to the multi-parameter fit function. The χ^2 of the fit did not change significantly when a multi-parameter fit is performed compared to a constant fit. We fixed the oscillation period at T_S, the sidereal period,

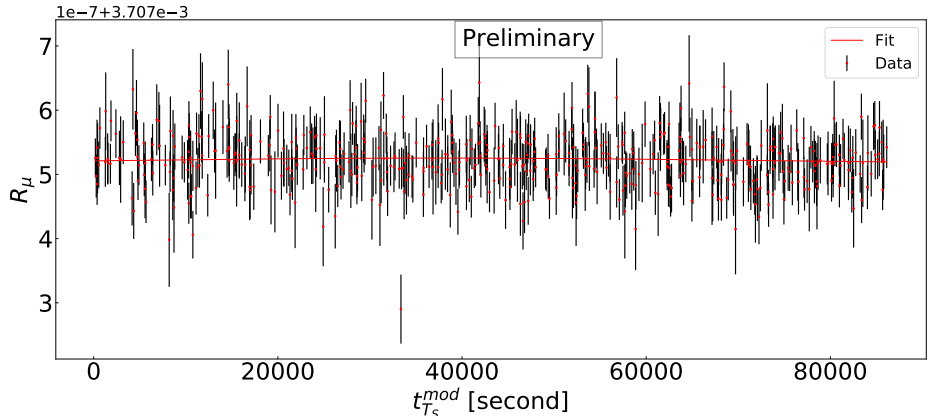


Figure 4.12: Figure shows an oscillation period scan of the 2019 Run 2 data, where we step through A_0 in the fit keeping the rest of the parameters floating. Top plot: Oscillation amplitude A_0 from the MPF fit. Bottom plot: unnormalized χ^2 of the fit. Absence of a global minimum in the bottom plot indicates no signal.

Parameter	Fixed $T = T_S$	Fixed $T = T_D$
C_0	$3.707 \times 10^{-3} \pm 1.65 \times 10^{-9}$	$3.707 \times 10^{-3} \pm 1.65 \times 10^{-9}$
A	0.934 ± 0.63	0.938 ± 0.63
ϕ	1.32 ± 0.66	1.33 ± 0.66
χ^2/ndf	1.02	1.02

Table 4.2: Comparison of the values of the fit parameters for a sidereal oscillation ($T = T_S$) fit and a solar day ($T = T_D$) fit

and set all the other parameters to float, and then set the oscillation period at T_D, the solar day for comparison.

In the 4-parameter fit, a scan on T_0 is done. In this scan we step through different values of T_0 keeping all other parameters fixed. The motivation is to search for any time structure near the sidereal period. Fig. 4.13 shows the oscillation period scan. The absence of a global minima in the χ^2 plot indicates that there is no significant signal present at any of the scanned periods. The broadening of peaks as the scan moves to the right is due to increased correlation of adjacent fit results as the scan moves to period values greater and greater relative to the data point (run) lengths. i.e. high frequency fits can be easily pulled by a few point-by-point random noise fluctuations over ranges on the order of the period fit, but low frequency fits are determined much more by the aggregate pattern over a large fraction of the data and much less affected by the random noise within that aggregate. Neither the sidereal nor the solar day period correspond to a local or global minima. The χ^2 of the fit for a potential oscillation is expected to have a global minimum at that period.

4.6.4 Expressing Lomb Power in terms of an Amplitude of Oscillation

As we know, the Lomb-Scargle test provides information of the frequency of a potential oscillation and the peak height indicates how significant the oscillation is. In order to express the information contained in the peak height in terms of the oscillation amplitude, a dedicated simulation study is performed.

Signals of random amplitude are added to the simulated data at the sidereal frequency; now

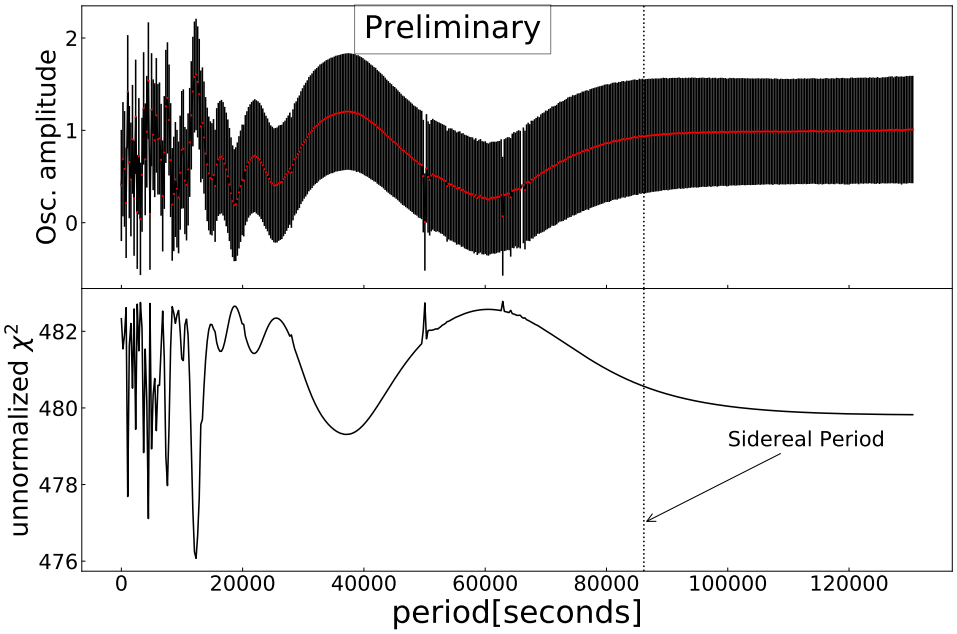


Figure 4.13: Figure shows an oscillation period scan of the 2019 Run 2 data, where we step through A_0 in the fit keeping the rest of the parameters floating. Top plot: Oscillation amplitude A_0 from the MPF fit. Bottom plot: unnormalized χ^2 of the fit. Absence of a global minimum in the bottom plot indicates no signal.

by selecting the amplitudes of the artificial signals that give rise to a Lomb power of 0.86, as seen in the Run 2 data at the sidereal frequency, we end up with a distribution of the amplitudes of a potential signal at the sidereal frequency, as shown in Fig. 4.14. The mean of this distribution is 0.68 with a standard deviation of 0.48. This number agrees quite well with the amplitude of the oscillation predicted by the multi-parameter fit, 0.94 ± 0.63.

4.6.5 Summary of the Run-by-Run results

In order to compare the results from the two methods used for the analysis, a simulation campaign is carried out. We simulate 10000 groups of random data based on the real data average and the individual uncertainties as before. False oscillation signals with different amplitudes are added to the simulated data at the sidereal frequency. The performance of the Lomb-Scargle test as well as the multi-parameter fit are then studied on the same simulated ensemble. We study the

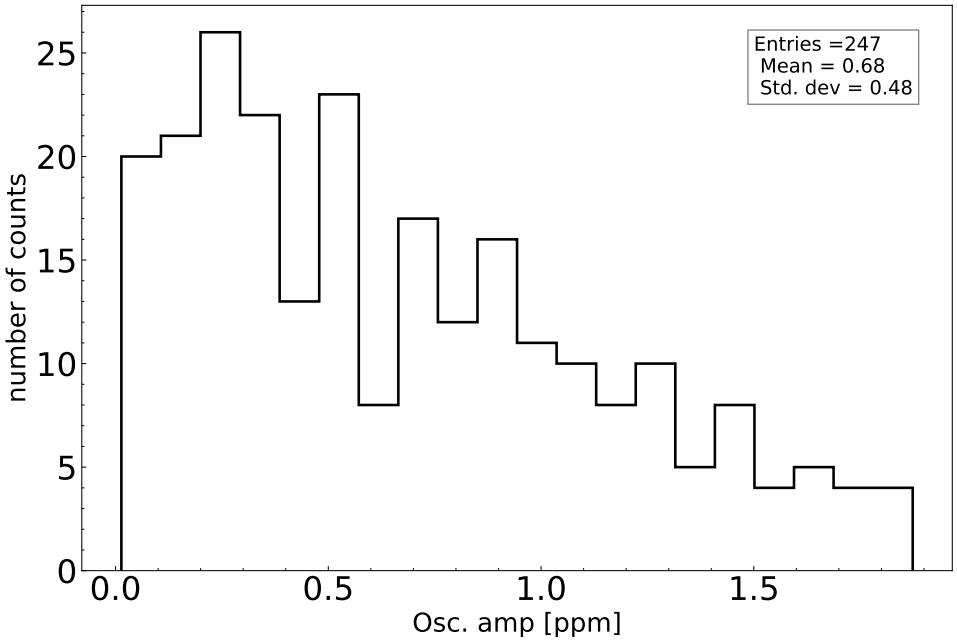


Figure 4.14: Figure depicts the distribution of the amplitude of artificial signals added to simulated data resulting in the same Lomb power at the sidereal frequency as seen from Run 2 data. The artificial signal amplitude from the corresponding Lomb power comes out to be 0.68 ± 0.48 ppm which agrees quite well with the amplitude predicted by the multi-parameter fit results, 0.94 ± 0.63.

Artificial Signal [ppm]	Prob. of having bigger amplitude A_0 (%)	Prob. of having bigger Lomb power (%)
1.0	50.57	54.07
1.6	83.19	84.85
1.9	92.08	93.04
2.0	94.35	94.99

Table 4.3: Table summarizes the results on simulation samples, where two methods; the Lomb-Scargle test and the multi-parameter fit are applied. These two methods agree quite welland set a limit of the potential sidereal oscillation component to be less than 2 ppm with $\sim$ 95% confidence level.

Lomb power at the sidereal frequency from the spectral analysis, and for the multi-parameter fits, we study the distribution of the oscillation amplitude, A_0 while keeping the period fixed at the sidereal frequency. Fig. 4.15 shows the distribution of the Lomb power at the sidereal frequency when we applied the Lomb-Scargle test on each of the 10000 cases. The shaded area in the plots show the cases in which the Lomb power measured at the sidereal frequency is less than that found in the real data, where the dotted vertical line indicates the Lomb power seen from the real data. Note that, at 2 ppm $\sim$ 95% of the time we calculate a higher Lomb power than what we saw in real data. This can be interpreted as the present oscillation signal amplitude at the sidereal frequency being less than 2 ppm with 95% confidence. Fig. 4.16 shows the distributions of oscillation amplitudes, A_0 obtained from the multi-parameter fit. The plots indicate that when the oscillation amplitude is 2 ppm, 95% of the time the fitted amplitude is higher than that from the real data. The results from the two methods agree very well. We applied both the methods on the same simulated data samples, and studied the probability of the Lomb power being greater than that of the real data at the sidereal frequency while for the multi-parameter fit, the probability of the fit parameter A_0 being greater than that of the real data is reported. Table summarizes the limits on the sidereal oscillations for Run 2 data along with the significance. The two analysis techniques are in agreement with each other, and indicate that the limit on the amplitude of a potential oscillation signal is 2 ppm with 95% confidence level.

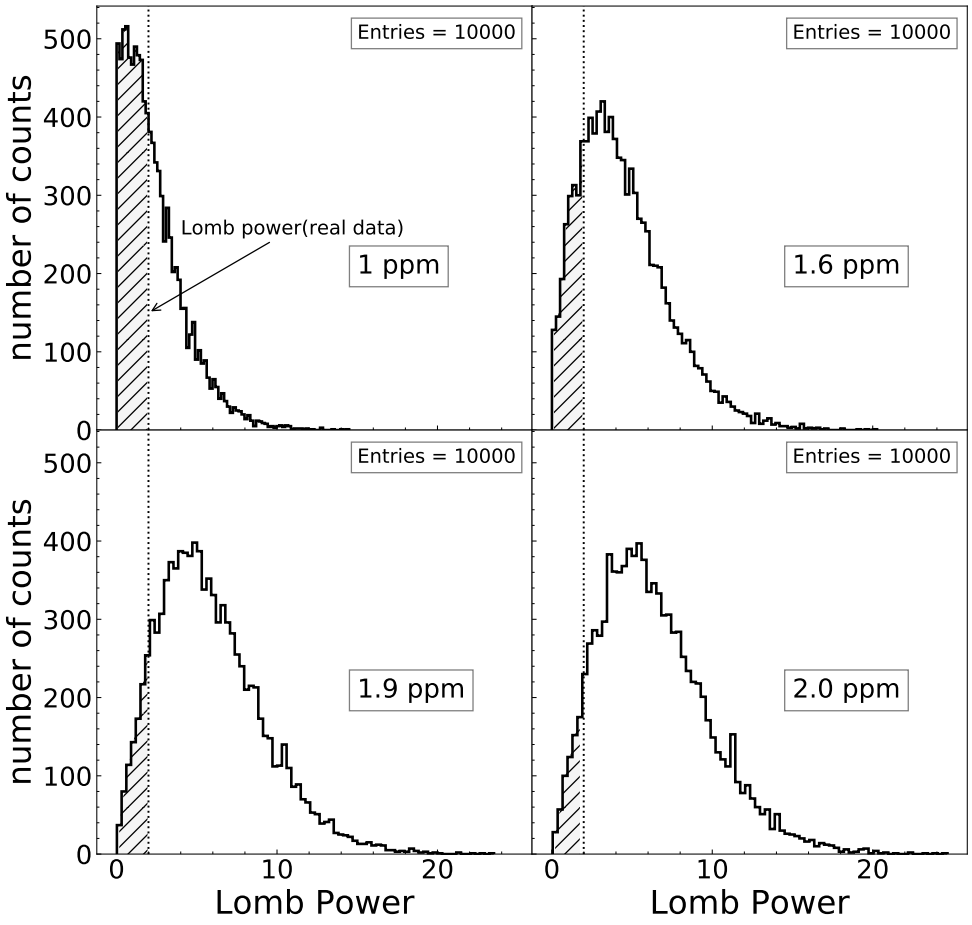


Figure 4.15: Distribution of Lomb power at the sidereal frequency for 10000 simulated data groups.The x-axis is the Lomb power at the sidereal frequency for each data group. We conclude from the above plots that the amplitude of oscillation in the real data is less than 2 ppm with 95% confidence level.

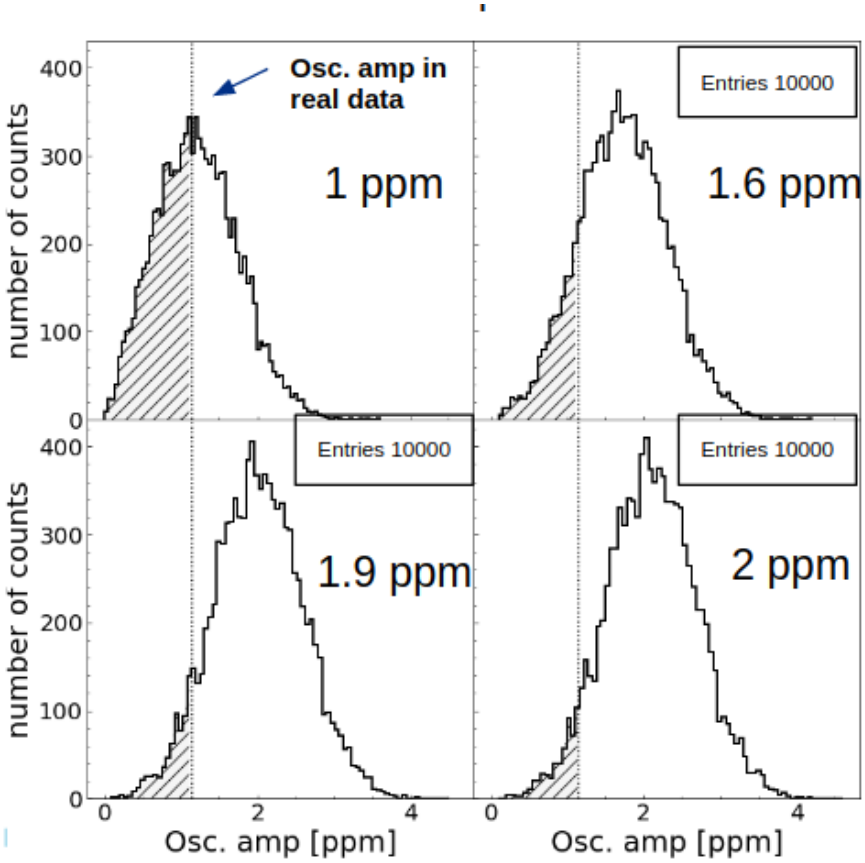


Figure 4.16: Distribution of the oscillation amplitudes at the sidereal frequency for 10000 simulated data groups are shown. The x-axis here is the oscillation amplitude, A_0 obtained from the multi-parameter fit. We conclude from the above plots that the amplitude of oscillation in the real data is less than 1.7 ppm with $\sim$ 95% confidence level.

Window Name(W)	Window Size[seconds]	Bin Width [seconds]
A	W = $4 \times T_S$	1346.31
B	W = $4 \times T_D$	1350.0
C	W = 4×123594	1931.16
D	W = 4×89903	1404.73
E	W = 4×92801	1450.02

Table 4.4: Table shows various window sizes for the data being folded with a time window.

4.7 Folded Data Analysis

For the folded data analysis, we choose the window size to be equal to or more than a sidereal period as we are performing a sidereal search. The window sizes were chosen to be a mulltiple of the sidereal period in order to observe any potential oscillation over more than one period. Five different window sizes were studied, where the two obvious choices are the signal and the background frequency,i.e., the sidereal period and the solar day period. Three other windows were randomly chosen to study the effects of binning the data in a particular way, and therefore study if we in any way biased the analysis by introducing the window sizes as integer multiples of sidereal or solar day period. The table 4.4 summarizes five different windows used as well as the bin widths for each of those cases.

4.7.1 Analysis for Window A

The first window, referred to as Window A from now on, is chosen to be four times the sidereal period. There are 256 bins chosen within the window. Hence, the width of each bin is $\sim$ 22 minutes. In order to fold the data, we first take the unixtime of each positron event modulo the time window, and then the time spectrum of the positrons are filled, resulting in histograms for each of the 256 bins within the window specified above. Now by performing a five parameter fit for each of those histograms corresponding to the bins within a window, a series of ω_a values are extracted. At this point we have a folded time series of ω_a. Now the field measurements are folded by taking the unix timestamps of each subrun modulo the time window. A subrun in the Fermilab experiment refers to $\sim$ 7.2 s of data collection. After folding the field measurements

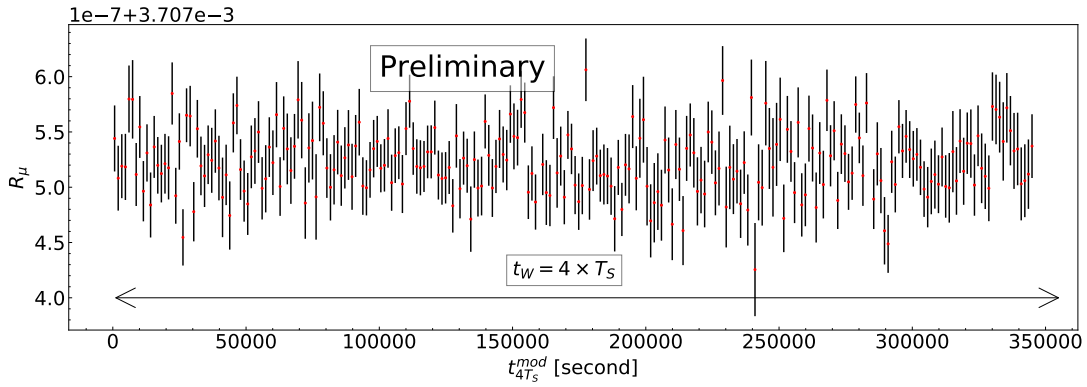


Figure 4.17: The folded time series of R_μ for Run 2. The time window chosen here is four times the sidereal period.

into the window, we took average of the measurements and assigned an uncertainty by taking the quadrature sum of the corresponding measurements in a particular bin. The last step is to take the ratio of these two measurements and construct a time series of folded R_μ.

4.7.2 Lomb Scargle Test on Folded Data With Window A

Since the data are already folded, the time series is no longer unequally spaced. The sophisticated Lomb-Scargle test in this case becomes a classical spectral analysis, and is expressed in terms of the corresponding FFT of the time series. The frequency range otherwise used must be adjusted to avoid redundancy in the power spectral plots. Hence, the frequency range used from now on for the folded data analysis is: $[0, \mathrm{F_c}]$, where $\mathrm{F_c}$ is the nyquist frequency. From Fig. 4.18 we see that the Lomb power at the sidereal frequency is ~ 2 and there is a small peak nearby. Note that the huge peaks at the zero frequency observed from the Run-by-Run analysis is completely washed out here when we folded the data from various parts of the whole time duration of 3.5 months. This confirms that the zero frequency peaks seen in the previous study are due to some artifact present in the data and not because of a potential oscillation component. It is evident that by folding the data into a smaller window we are losing sensitivity to noise arising from effects other than a strong oscillation signal. To investigate the structues in the power spectra we consider different window sizes next.

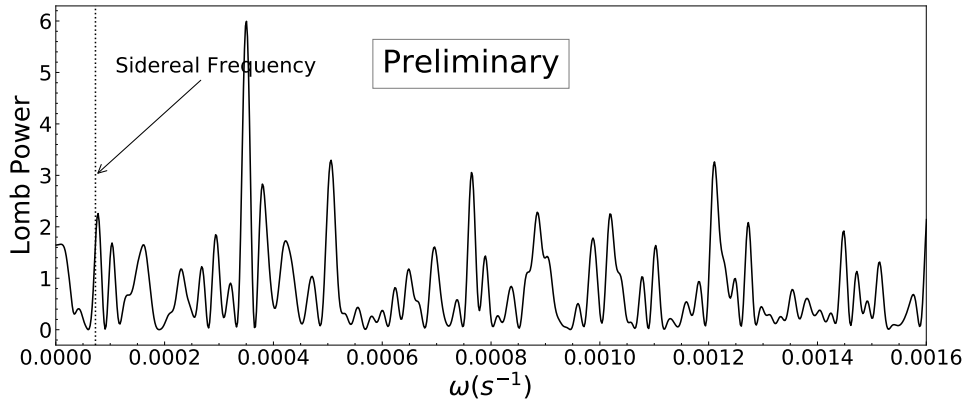


Figure 4.18: The Lomb-Scargle power spectrm for folded time of window A.

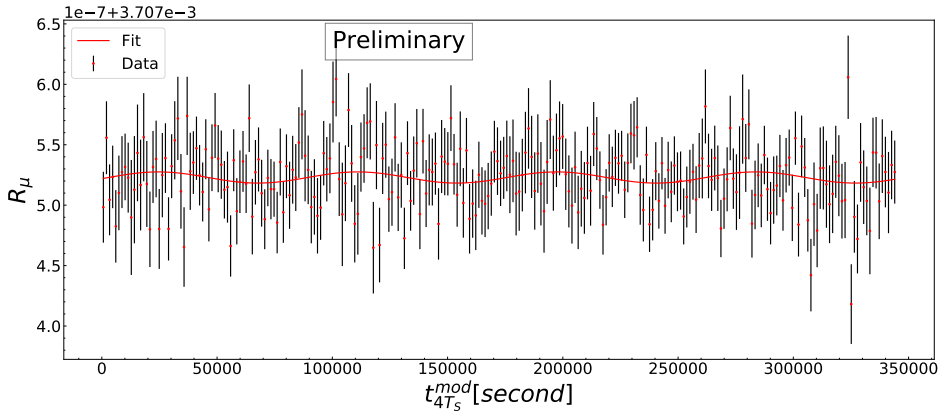


Figure 4.19: The multi-parameter fit for folded time of window A.

4.7.3 Multi-parameter Fit on Folded Data with Window A

The folded data is fit to the multi-parameter fit function as before to obtain the oscillation amplitude. The χ^2 of the multi-parameter fit did not change when compared with a constant fit, which is consistent with the run-by-run results. In order to perform an oscillation period scan, a series of fits are done with fixing the oscillation period to a certain value within the scan range while all the other parameters are free to float. The results of the oscillation period scan is in agreement with the run-by-run analysis. There is no significant signal present in the data analyzed here. The oscillation amplitude from the fit comes out to be 1.2 ppm. The unnormalized χ^2 does not have a global minimum in the scan range confirming the previous claim of the absence of a potential

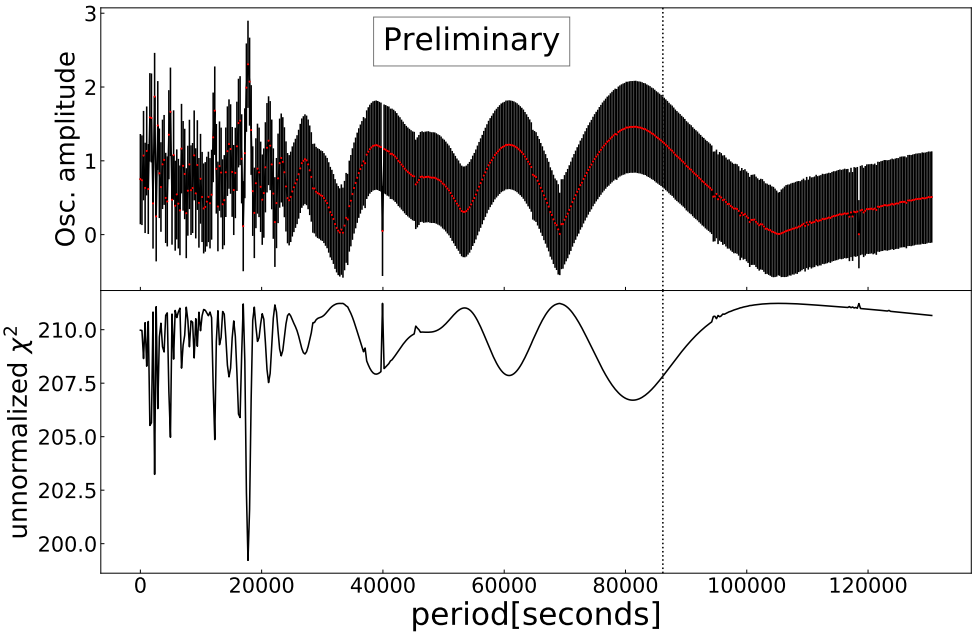


Figure 4.20: Oscillation period scan for folded time of window A.

signal with any of the periods scanned.

4.7.4 Analyzing Five Different Windows

To investigate the appearance and disappearance of peaks due to statistical flustuations, we considered five different window sizes. The Lomb Scargle test was performed on each of these differently binned data. Fig. 4.21 shows the power spectra for all five windows. We see that the position of the highest peak depends on the choice of binning. The fact that the appearance of the small peak at the sidereal frequency depends on window sizes, reinforces that the peak near the sidereal frequency arises due to statistical noise. Presence of any peak due to a significant oscillation signal must not depend on how we choose to bin the data. The multi-parameter fit results on the folded data are summarized in table 4.5. The values of the fit parameter A from the table for various windows are consistent with a prediction of no significant signal at the 2σ level. The consistency of the best-fit parameter values among various windows confirms that there is no significant signal in the data. Fig. 4.22a show the oscillation period scan results from each window.

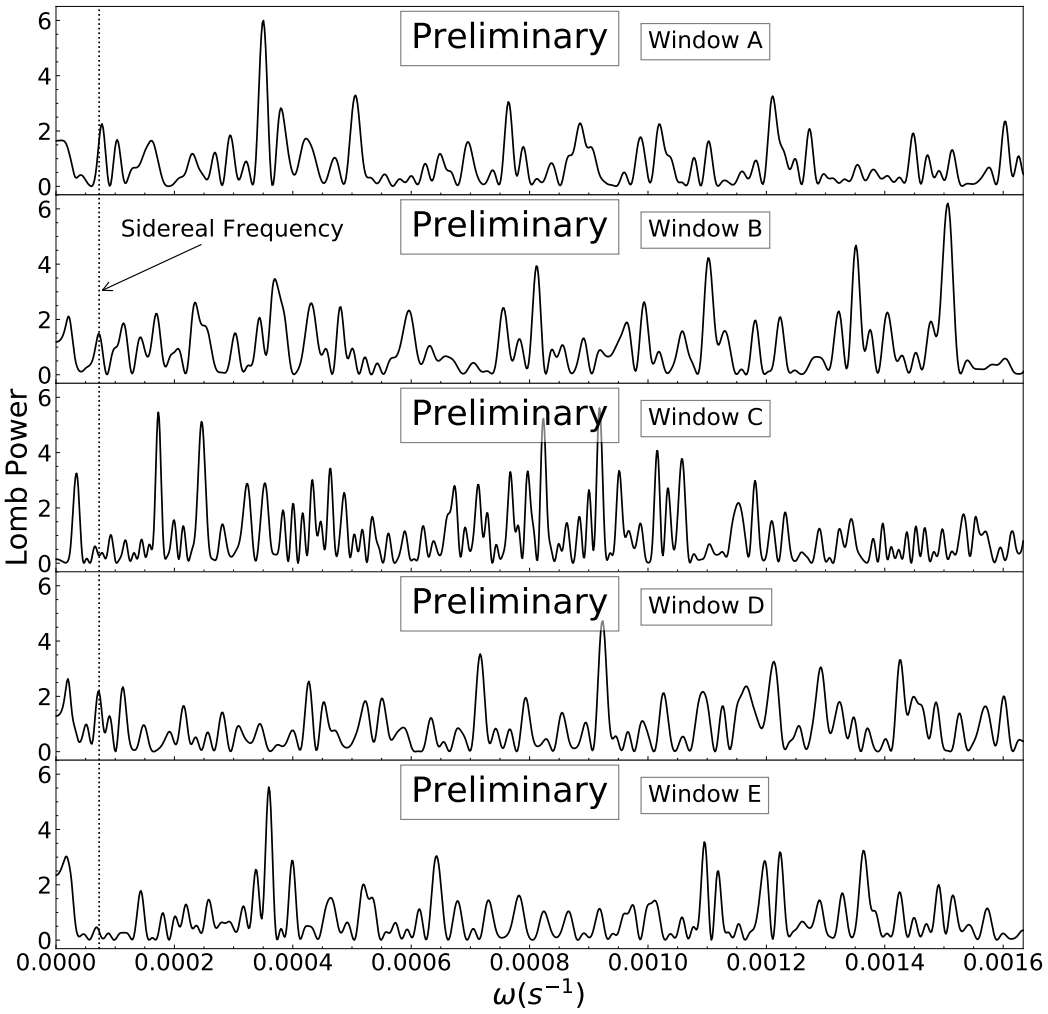


Figure 4.21: The Lomb-Scargle power spectrm for five different windows.

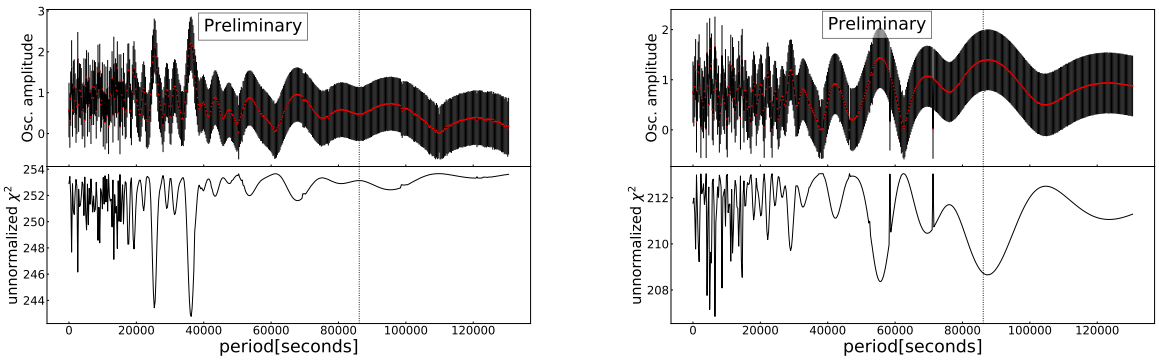
Preliminary	Preliminary	Preliminary
Window size (W)	fix $T = T_S$	fix T = 24h
A (W = $4 \times T_S$)	$\chi^2 = 0.82$ A = -1.21 ± 0.68 $\phi = 1.36$	$\chi^2 = 0.82$ A = -1.23 ± 0.68 $\phi = 1.39$
B (W = $4 \times T_D$)	$\chi^2 = 1.15$ A = 1.03 ± 0.63 $\phi = 0.47$	$\chi^2 = 0.82$ A = 1.03 ± 0.63 $\phi = 0.50$
C (W = $4 \times 123594s$)	$\chi^2 = 1.0$ A = 0.48 ± 0.66 $\phi = 2.88$	$\chi^2 = 1.0$ A = 0.46 ± 0.61 $\phi = 0.47$
D W = 4×89903	$\chi^2 = 0.82$ A = -1.38 ± 0.66 $\phi = 0.46$	$\chi^2 = 0.82$ A = -1.34 ± 0.62 $\phi = 0.46$
E W = 4×92801	$\chi^2 = 0.86$ A = 0.52 ± 0.63 $\phi = 0.32$	$\chi^2 = 0.86$ A = 0.53 ± 0.63 $\phi = 1.15$

Table 4.5: Fit parameters for different window sized folded data. A is expressed in ppm. The windows C, D and E were chosen randomly to verify the binning effects when binned differently from the sidereal period.

The sidereal period does not correspond to a global minimum in any of the oscillation amplitude scans, hence confirming again the absence of a potential signal at the sidereal period.

4.7.5 Summary of the Folded Analysis

Again to compare the results of the Lomb-Scargle test and the multi-paramter fit we generate simulated data for each time bin from a normal distribution with a central value as the average of R_μ and the individual data pointś standard deviation. By studying the behavior of the analysis methods on simulated folded datasets with false signal injected at the sidereal frequency, we can also compare the sensitivity of the folded data and the run-by-run data. There is always a risk of losing sensitivity towards potential oscillations by folding the data in a certain way. Artificial signals of different amplitudes are added to the simulated data and the two analysis methods are then performed on 10000 such simulated samples as before. Fig. 4.23 shows the distribution of oscillation amplitudes, i.e., the best-fit value of A in each of those 10000 cases. The shaded area in the plots represents the best-fit parameter values less than that of the real data at the sidereal



(a) (b)

Figure 4.22: Oscillation period scans on data folded in window C and D respectively. The oscillation amplitude on the y-axis of the top plot actually is the fit parameter A in ppm. The y-axis of the bottom plot is the unnormalized χ^2 of the multi-parameter fit for each value of the oscillation period, T_0. The vertical line corresponds to the sidereal period.

Artificial Signal [ppm]	Prob. of having bigger amplitude A_0 (%)	Prob. of having bigger Lomb power (%)
1.0	50.78	48.02
1.6	82.76	80.64
1.9	92.09	90.51
2.0	94.19	93.04

Table 4.6: Table summarizes the results on simulation samples, where two methods; the Lomb-Scargle test and the multi-parameter fit are applied. These two methods agree quite welland set a limit of the potential sidereal oscillation component to be less than 2 ppm with $\sim$ 94% confidence level.

frequency. From this study, the limit on the oscillation amplitude comes out to be 2 ppm with a confidence level of 94.19%. The spectral analysis results on the same simulated datasets are shown in Fig. 4.24. The Lomb power distribution at the sidereal frequency shows that the peak amplitude is bigger than that of the real data $\sim$ 93% of the time when we added a false signal of 2 ppm. Hence, the prediction from the two methods agree quite well with each other. Table 4.6 summarizes the results from the simulation studies.

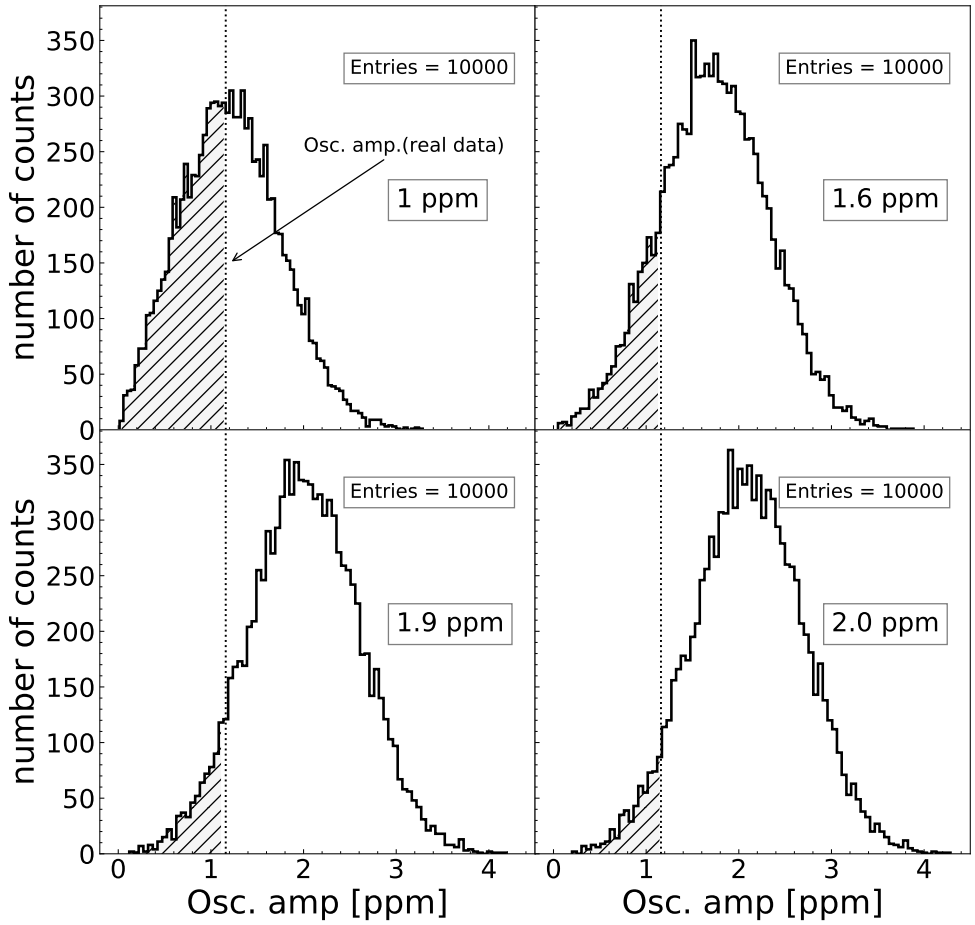


Figure 4.23: Distribution of best-fit values of the fit parameter A_0, the oscillation amplitude on simulated folded data of window size A. The vertical line corresponds to the value of A_0 from real data. The bottom right plot shows that the amplitude of oscillation is bigger than that of the real data $\sim$ 94 % of the time when an artificial signal of amplitude 2 ppm is present. Hence, setting a limit of 2 ppm with confidence 94%.

4.8 Summary: Run-by-Run and Folded Data Analysis

We have implemented two different analysis techniques on Run 2 data, where we binned the data in two different ways. The conclusion from all these combinations of data binnings and analysis techniques agree with each other; there is no significant signal present at the sidereal frequency. The limits on the amplitude of a potential sidereal signal from simulation studies are

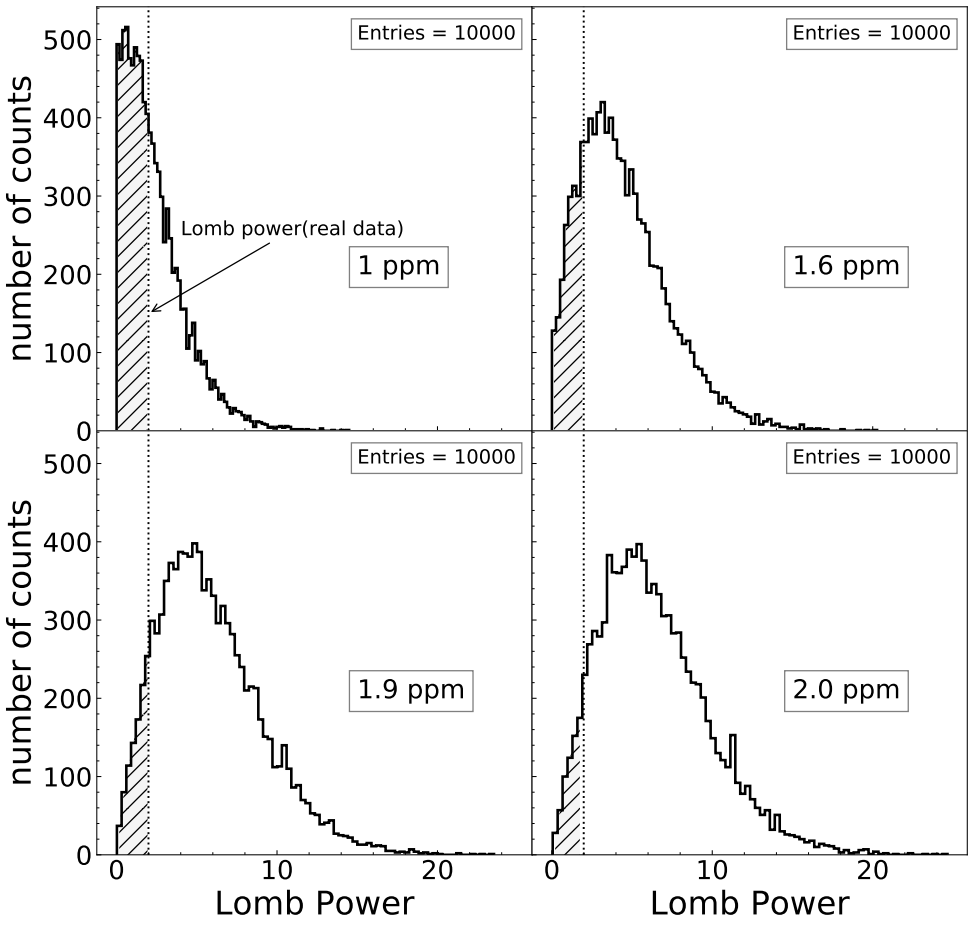


Figure 4.24: Distribution of the Lomb power at the sidereal frequency for simulated folded data of window size A. The vertical line corresponds to Lomb power obtained from real data. The bottom right plot shows that the Lomb power is bigger than that of the real data $\sim$ 93 % of the time when an artificial signal of amplitude 2 ppm is present. Hence, setting a limit of 2 ppm with confidence 93%.

2 ppm with a 95% confidence level from the run-by-run data analysis. The confidence level for the same amplitude of signal slightly differs in the folded data analysis; this is due to the fact that the folded data loses sensitivity towards the whole duration of the measurement period.

4.9 Systematic Concerns

One of the most important systematic effects may arise from the consideration of R_{mu} instead of ω_a. Presence of a potential sidereal signal in $\tilde{\omega}'_p$ could nullify the effect of any signal in ω_a hence making the analysis insensitive to any CPT and LV signals. The magnetic field is measured using NMR techniques in terms of the proton precession frequency, $\tilde{\omega}'_p$. An upper limit at the mHz level is given on the sidereal oscillation of $\tilde{\omega}'_p$ by the atomic clock comparisons. This limit is smaller than the resolution of the magnet's feedback control system. The limits of electron and nucleon local Lorentz violation are predicted from the observations of the stability of the relative frequency of the Hg and Cs magnetometers by Berglund et al. [56]. The limits on the electron and nucleon local Lorentz violation are 10^{-27} GeV, so there is no reason to worry about a potential cancellation. However, there could be experimental apparatus induced oscillations in the field measurements. One of the potential background in this analysis could stem from the day-night temperature variation in the experimental hall affecting the stability of the magnetic field. The solar day (24 hours) is very close to one sidereal day (23 hours 56 minutes). In order to provide the limits on the Run 2 dataset of the $g-2$ experiment, we run the sidereal oscillation search on $\tilde{\omega}'_p$ alone. Fig.4.25 shows the time series of the field measurements for Run 2. From Fig. 4.25 we see that there were field instabilities in Run 2; the value of the magnetic field had jumps as high as 1 ppm, however the field values were measured and monitored extremely precisely during the whole period of data taking. These occasional jumps in the measurement were due to the running conditions in the summer of 2019; the experiment at that time was running for 5 days followed by a 9 day off period synchronized with the Fermilab Accelerator Division's beam supply availability. So the main magnet would be off for 9 days and we faced some challenges while powering the magnet back up. Because of the presence of these instabilities it is not possible to simply generate

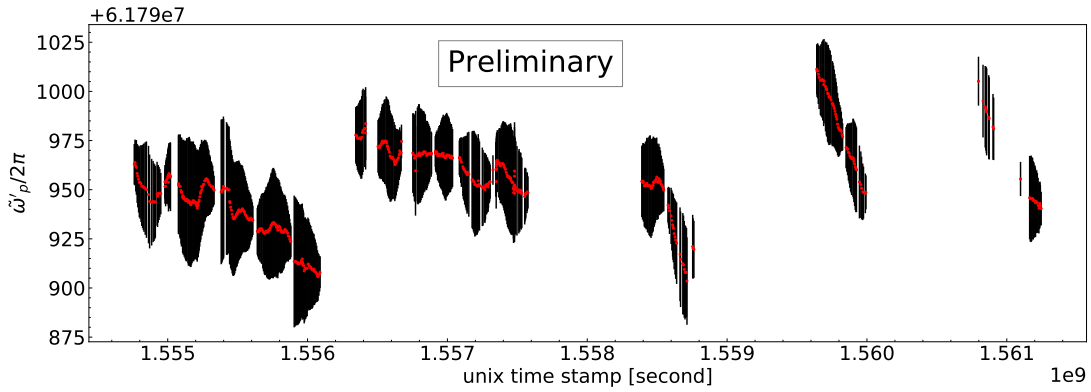


Figure 4.25: The time series of the magnetic field measurements for Run 2.

random numbers based on the average field value for generating huge simulation samples as done for studying the effects on R_μ. Also, for the same reason as explained above we can not fit the field data either to a multi-parameter fit function or a constant fit. The Lomb-Scargle test is still valid for the field data, and can provide the information of any potential oscillation at the sidereal frequency. Note that the field instabilities will definitely give rise to spurious peaks in the power spectrum. Fig. 4.26 shows the power spectrum, where the spectral analysis is performed on the whole Run 2 dataset as well as dividing the data in two pieces to investigate the presence of various peaks in the analysis. A huge peak near zero frequency is present in the top plot, indicating an artifact present in the data. The nearby smaller peaks are caused by the spectral leakage from the highest peak; frequency leakage is a well-known problem in spectral analysis methods. the highest peak also suggests that the period of such an oscillation will be infinite; reinforcing that the peak is caused by instabilities during 5 day beam on-9 day beam off period in later half of Run 2 as well as from large constant offsets that were not taken into account. The power spectrum also shows a small peak near the sidereal frequency for the whole dataset. The significance of this peak is negligible, which is also confirmed by the midlle and the bottom plot where we considered 1st and 2nd half of the data respectively for the analysis. The potential reason for the small peak at the sidereal frequency is the statistical noise present in the data as well as the temperature instabilities during the 5 day beam on-9 day beam off period. This must be studied again in great detail for Run 3 datasets. Note

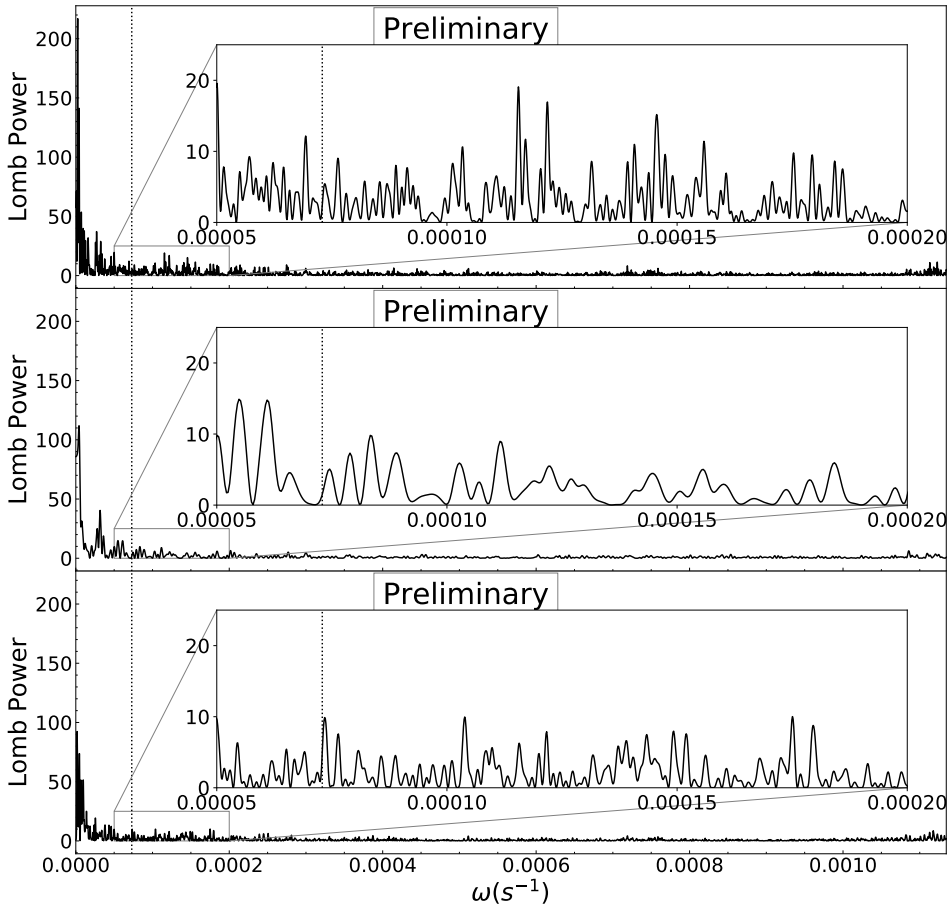


Figure 4.26: Figure shows the spectral analysis performed on the field measurements. The top plot shows the spectral power as a function of frequencies within the search range along with a zoomed in version to focus on the peaks near the sidereal frequency. The middle and bottom plots show the spectral power analysis when only partial data were used for the analysis in order to investigate the presence of various peaks over the search range.

that in general the peak amplitudes are much higher than that from the power spectrum of R_μ. This is due to the smaller uncertainties on the magnetic field data points; the statistical uncertainty is negligible in case of the field measurements and the overall uncertainty is dominated by various systematic effects whereas the ω_a measurements are largely dominated by the statistical uncertainty on each datapoint. Because of the relatively smaller uncertainties the Lomb-Scargle test is much

more sensitive to a slight variation in the field. In other words, the significance is much less for a peak of same height in the field data than the ω_a data. As seen in the previous section, the power spectrum of R_μ is largely dominated by that of ω_a.

For this run, one of the possibilities of setting a limit on the potential sidereal variation amplitude arises from adding artificial signals of various phases to the real data and then perform the spectral analysis. The concept used here is that if we add an artificial signal at the sidereal frequency with an opposite phase then that will cancel any potential signal component already present in the real data and will end up reducing the peak amplitude, on the other hand adding a signal which is in phase with a potential signal component already present in the real data will enhance the oscillation and hence cause a larger peak height at the sidereal frequency in the power spectrum. For instance, if there is a potential oscillation signal with phase ϕ, then adding an artificial signal with phase $\phi+\pi$ will end up minimizing the peak height at a given frequency. A scan over a range of phases were done to confirm this. Once we fix the phase of an artificial signal, we move forward to perform a scan on the amplitudes of the added artificial signal. Fig. **??** shows the result of such a scan. The Lomb power is minimum when the amplitude of the artificial signal is 0.03 ppm. So the limit on the sidereal oscillation amplitude is less than 0.03 ppm for Run 2 dataset. This being negligible compared to the limit of 1.7 ppm on R_μ rules out the possibility of cancellation of a potential signal present in both the numerator and the denominator of $R_\mu(=\omega_a/\tilde{\omega}'_p)$. This study confirms that an accidental or even a real peak in the spectral analysis of $\tilde{\omega}'_p$ will not harm the analysis because of its negligible significance compared to the scale of ω_a. If we consider that there is a sidereal signal present in the field measurements as given by (4.9)

$$\tilde{\omega}'_p(t) = \tilde{\omega}'_{p,const.} + \hat{\tilde{\omega}}'_p \cos(\omega_s t + \phi_p) \tag{4.9}$$

where, $\tilde{\omega}'_{p,const.}$ is the constant term in the time variation and $\hat{\tilde{\omega}}'_p$ represents the amplitude of a

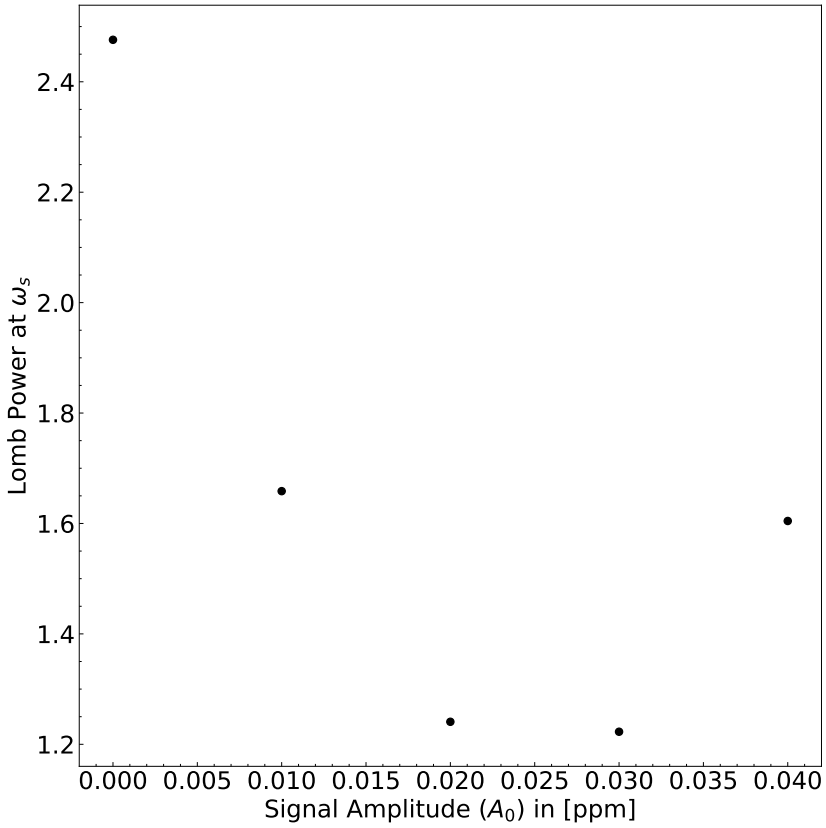


Figure 4.27: Figure shows an oscillation period scan of the 2019 Run 2 data, where we step through A_0 in the fit keeping the rest of the parameters floating. Top plot: Oscillation amplitude A_0 from the MPF fit. Bottom plot: unnormalized χ^2 of the fit. Absence of a global minimum in the bottom plot indicates no signal.

potential signal. Then the ratio can be expressed as

$$\frac{\omega_a}{\tilde{\omega}'_p} = \frac{\omega_a}{\tilde{\omega}'_{p,const.} + \hat{\tilde{\omega}}'_p \cos(\omega_s t + \phi_p)} = \frac{\omega_a}{\tilde{\omega}'_p}(1 - \frac{\hat{\tilde{\omega}}'_p}{\tilde{\omega}'_{p,const.}} \cos(\omega_s t + \phi_p)) \tag{4.10}$$

where we have expressed the ratio in terms of a Taylor series expansion. The ratio $\frac{\hat{\tilde{\omega}}'_p}{\tilde{\omega}'_{p,const.}}$ is at the ppm (10^{-6}) level whereas $\frac{\omega_a}{\tilde{\omega}'_p}$ is at the level of 10^{-3}. This reiterates that a small sidereal signal in the field data data does not introduce a detectable effect in the $g-2$ data.

4.9.1 Benchmarking The Analysis

From the Lomb-Scargle test and the multi-parameter fit methods we reached the conclusion that there is no significant signal present in the $g-2$ Run 2 data; this also depends on the sensitivity of the algorithms used for the search. In order to benchmark the analysis, we studied the performance of the algorithm against the case of a potential background arising from the solar day. If we saw a significant signal, it would be very important to be able to justify the potential signal arising from the sidereal frequency itself and not from the most obvious background. For a sidereal search the potential background comes from the solar day; we study the effects in the spectral analysis when two signals are injected simultaneously at the sidereal frequency as well as the solar day frequency. Fig. 4.28 shows that the algorithm is unable to distinguish between two signals with same amplitude (4 ppm each); one with sidereal frquency and the other one with solar day frequency. These frequencies are so close to each other that they fall within the frequency resolution for the given Run 2 observational baseline. The frequency resolution is determined by the size of the time interval over which the data are sampled, and due to the finite size, $\sim$ 3.5 months in Run 2, the algorithm fails to detect two simultaneous signals with frequency positions in close proximity. To study the peak widths and heights for cases when two signals are injected

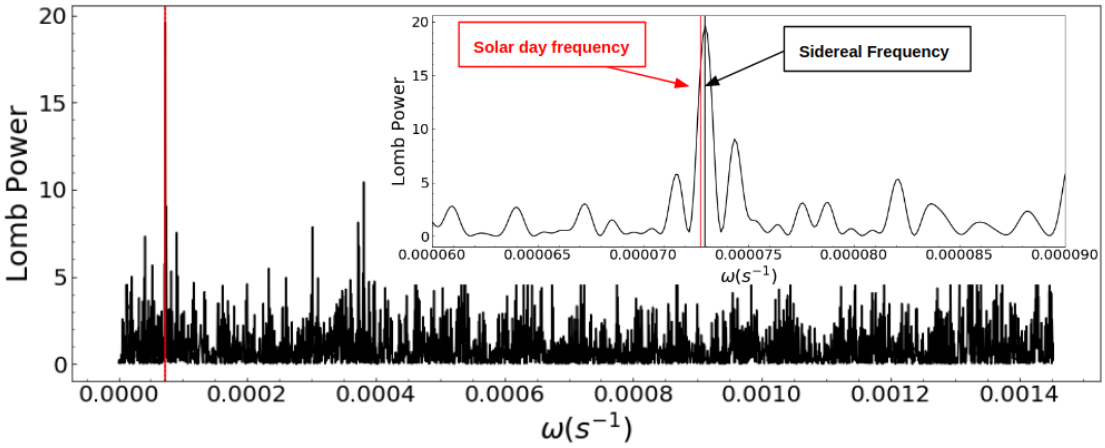


Figure 4.28: The time series of the magnetic field measurements for Run 2.

simultaneously, we generate simulated data using the average value of $R\mu$ and the uncertainties on real data points as done previously. Lomb-Scargle test is performed on 1000 simulated data groups

after adding two artificial signals of amplitudes 1 ppm to 4 ppm, and the position of the highest peak is stored each time along with the peak width in order to characterize the effects coming from the presence of multiple signals. Fig. 4.29 shows the distribution of the highest peak width from

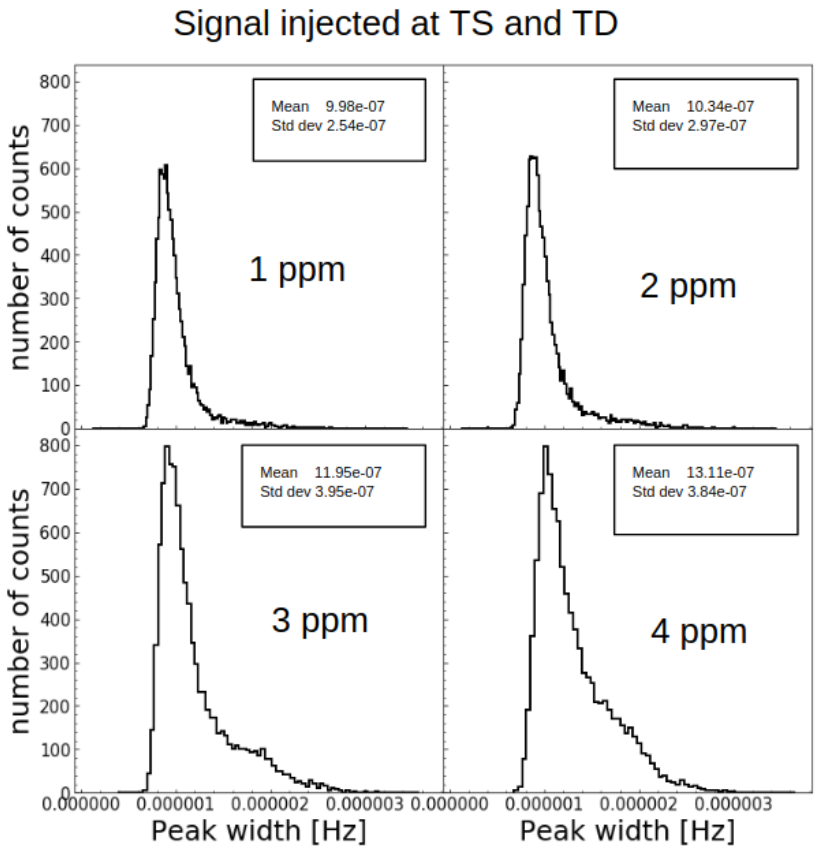


Figure 4.29: Figure shows the distribution of the widths of the highest peak for 1000 simulated data groups with two artificial signals of same amplitude added at the sidereal frequency and the solar day frequency, with 1 ppm to 4 ppm. There is a small shoulder that arises for higher amplitude signals.

the power spectrum on simulated data groups when two signals were added. The distribution starts showing a shoulder on the right as we keep increasing the amplitude of the injected signals. For comparison we also studied the distribution of the peak widths when only an artificial signal is injected at the sidereal frequency. The distribution in this case is shown in Fig. 4.30. The analysis provided an upper limit of 1.7 ppm on the amplitude of the sidereal oscillation in R_μ, and the above study of the peak width distribution in this limit is not sufficient to draw a conclusion about the source of the peak. Furthermore, the distribution of the position of the highest peaks corresponding

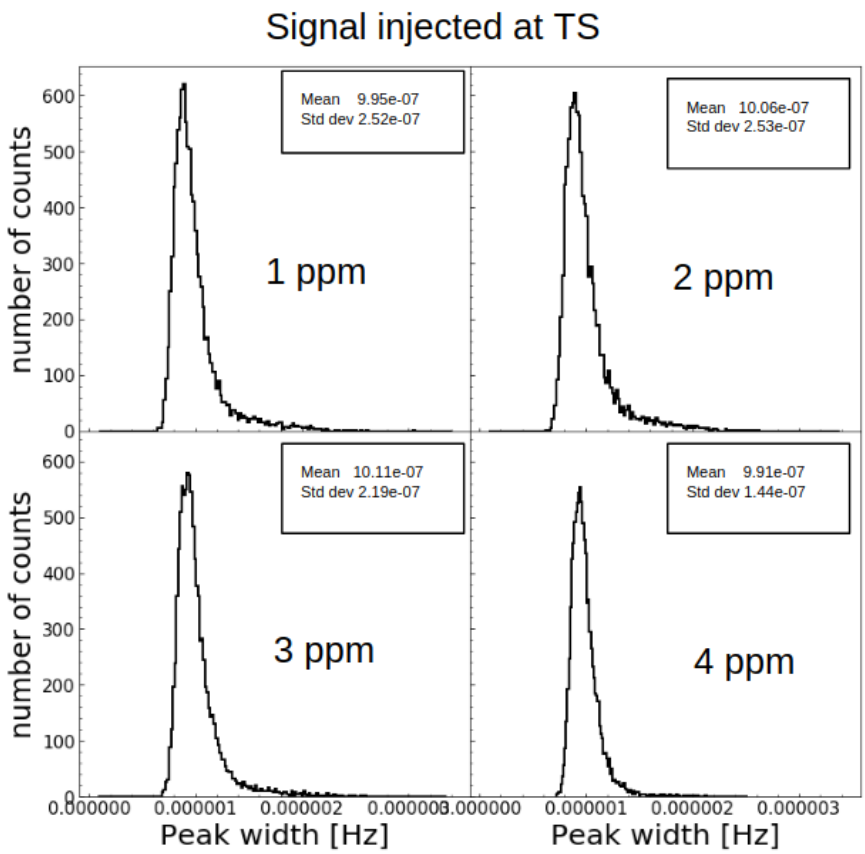


Figure 4.30: Figure shows the distribution of the widths of the highest peak for 1000 simulated data groups with artificial signals of 1 ppm to 4 ppm injected at the sidereal frequency.

to an artificial signal injected at the sidereal frequency were also compared to that in the case of an artificial signal at the solar day frequency. Fig. 4.31 shows the comparison of the two distributions of the positions. This is done by first adding an artificial signal at the sidereal frequency (T_S) to the simulated data groups and then performing the Lomb-Scargle test to see which frequency the highest peak corresponds to; then the same study is repeated but this time with an artificial signal added at the solar day frequency(T_D). This study shows that the possibility of resolving a potential signal at T_S from the background at T_D is very limited, and is proportional with the amplitude of the signals involved. We will collect more data as we move forward with the $g-2$ experiment but the current limit of 1.7 ppm is already below 3 ppm, so it is highly unlikely that we will be able to distinguish between signal and background. This study also gives as an insight to the biases in the algorithm in presence of an oscillation signal. Fig. 4.31 shows that there is a slight frequency bias

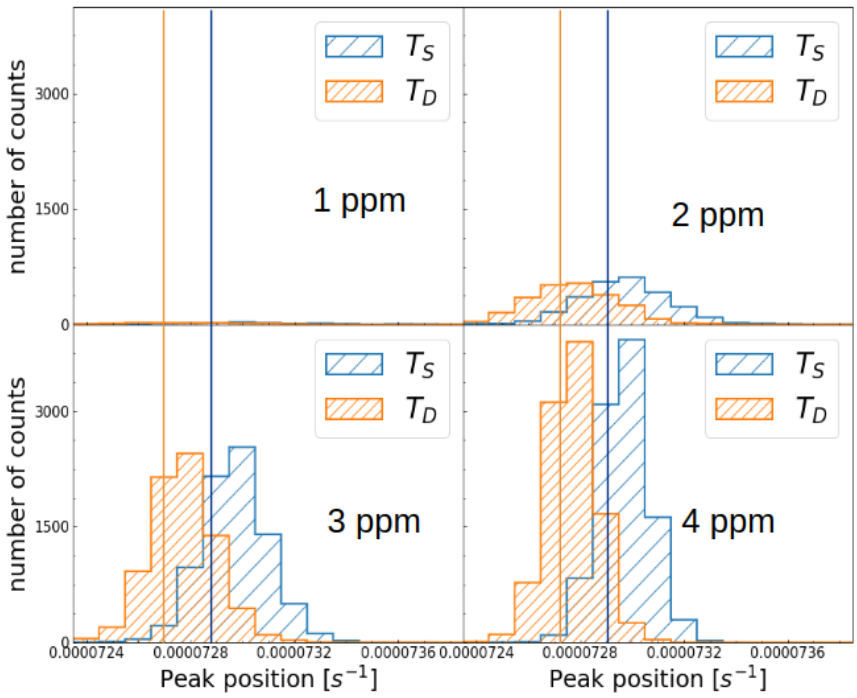


Figure 4.31: Figure shows the comparison of the distribution of the position of the highest peak for 1000 simulated data groups with artificial signals of 1 ppm to 4 ppm injected at the sidereal frequency and that at the solar day frequency.

in the method as both peaks occur in the next highest bin above the bin containing T_S (or T_D). This bias appears to be about half the width of a bin ($0.5 \times 10^{-8} s^{-1}$).

4.10 Conclusion

One of the CPT and LV signatures was tested in this dissertation. The results are based on a preliminary Run-2 dataset and do not represent the final result that will be published in 2022. The results reported in this dissertation are considered as a sensitivity test for the eventually published CPT and LV results.

From the preliminary search we conclude that there is no significant signal present in the Run-2 dataset; the preliminary Run-2 dataset contains $\sim$ 11 billion events. The χ^2 did not not improve in the multi-parameter fit method while adding an oscillation term to a constant. The Lomb-Scargle test results also agree with the findings of the multi-parameter fit. The highest peaks in the spectral power plot at other frequencies within the search range are randomly distributed,

confirming the potential source to be statistical noise. The results from two different data binnings are also in agreement with each other. Based on the simulations in Sect. 4.6.5, we set a limit on the sidereal oscillation amplitude to be less than 2 ppm with 95% confidence level. A 2 ppm signal corresponds to $\check{b}_{\perp}^{\mu^+} = \frac{\hat{\omega}_a^{\mu^\pm}}{2|\sin\chi|} = 1.27 \times 10^{-24}$ GeV, where χ is the colatitude of Fermilab, 48.2°. The limits listed in the Data Tables [33] on $\check{b}_{\perp}^{\mu^+} = 1.4 \times 10^{-24}$ GeV comes from the BNL Muon $g-2$ Experiment.

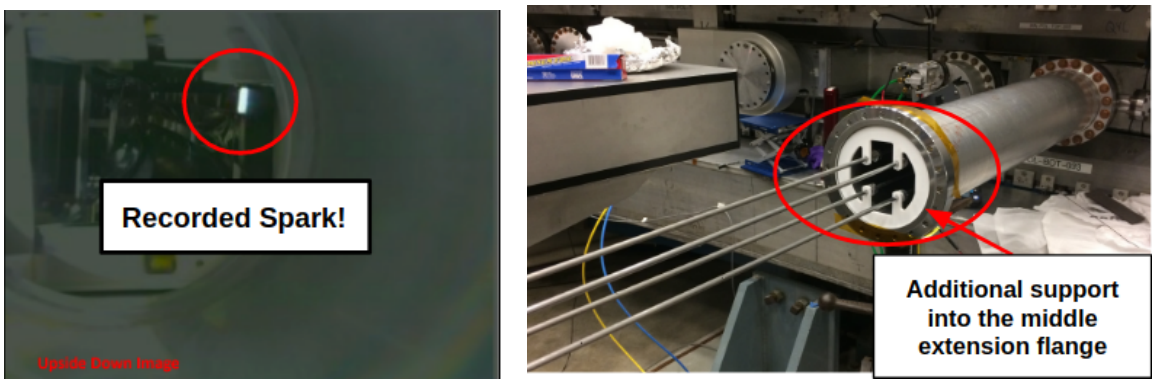
CHAPTER 5

Future Prospect

This dissertation explains the theoretical contributions as well as the technique used for the experimental measurement. The Fermilab Muon $g-2$ experiment published its first result on the Run 1 data, and currently the combined experimental measurement of a_μ is in tension with the theoretical prediction at the level of 4.2σ. This has stirred a lot of excitement in the physics comminuty and could point to the next big breakthrough. The Fermilab experiment confirms the discrepancy reported by the Brookhaven experiment twenty years ago. So far the collaboration has analyzed less than 6% of the data that the experiment plans to collect, and the results are very promising. Combining the results from all five runs will give us even more precise measurement of the muon's precession in the presence of an external magnetic field, which will help us reach the experimental goal of more than 5σ discovery limit. The results on Run 2 and Run 3 data are scheduled to be published in the summer of 2022, with an improvement on not only the statistical uncertainty but also the systematic uncertainties. This publication will be unique in a sense that, the first results of a detailed CPT and Lorentz violation search and the electric dipole moment (EDM) will be published along with the a_μ result.

5.1 $g-2$ Operations

One of the crucial systems for storing the muon beam in the storage ring is the electrostatic quadrupoles, as discussed in chapter 2. During Run 1 the performance of the system was found to be less than 100%, due to frequent voltage breakdowns, also referred to as sparks. Our goal was to tackle challenging operational issues associated with running the high voltage system at 20 kV, which is a requirement for good beam storage. Occurance of electrical sparks in high voltage



(a) High voltage spark (b) adding ceramic support to reduce mechanical vibration

Figure 5.1: The first figure shows a spark at the quadrupoles recorded by a camera. The second figure shows one of the mitigation strategies used in the 2018 summer shutdown.

systems is a known problem, and the design constraints in the $g-2$ experiment makes it even more difficult. To adress this issue many equipments and tools were developed, we used mirrors and cameras to capture the sparks. There are stand-offs that support the four plates against vibrations caused by the pulsed high voltage. One particluar stand-off was found to be causing more sparks, and was replaced in-situ by first uninstalling and then reinstalling the parts that sit outside the vacuum chamber. The high voltage (HV) plates that provide the vertical focusing to the muon beam are connected to resistors by long HV leads; the distance between two HV leads was found to be small, this was solved by fabricating small alignment tools, and adding small 3 deg bends to the leads. In the summer shutdown after Run 1 two of the 32 resistors were found to be damaged and hence causing the beam to move during Run 1 data taking. One of the biggest systematic uncertainties come from this effect in Run 1 result. With the resistors now replaced this systematic effect is expected to be negligible from Run 2 onward, and hence improving the uncertainties.

The second largest systematic uncertainty stems also from the quadrupole systems; during Run 1 it was found that the otherwise stable magnetic field has a time dependent variation in the regions covered by the quadrupoles. A lot of effort went into understanding the cause of this variation; for instance if the effect stems from vibration of the quadrupole plates; more efforts are planned to study this effect in the next shutdown period. The mitigation strategies are quite

Physics	μ^+ data	μ^- data
Overall stats	more statistical precision	2× BNL
μ^- stats	-	4× BNL
Additional Physics	-	$b_{\perp}^{\mu^-}$ b_Z d_{Z0} H_{XY}

Table 5.1: The Table summarizes the physics advantages for an additional one year of running the experiment in case of a positive as well as negative muon beam.

complicated and can not be performed in-situ, and the discussion for pinning down this effect is still ongoing.

5.2 Muon $g-2$ Experiment - Here to Where?

The $g-2$ experiment is on track to collect more data with the positive muon beam, the data analysis is currently underway for Run 2 and Run 3, and we are collecting data for Run 4, and a subsequent Run-5 is scheduled for 2022. It will be interesting to perform the sidereal search using the spectral analysis techniques on a larger observational baseline, which can be done by combining the Run 2 and Run 3 datasets. The power spectrum and the analysis results of Run 2 can then be verified. Combining the two runs will result in a larger duration of data taking compared to ~ 3.5 month duration of Run 2, hence the algorithm will be more sensitive towards smaller frequencies. One of the future possibilities is to run the experiment with a negative muon beam. In order for a complete understanding, the most straight forward test is to repeat the measurement with negative muon beam. The strong motivation behind a negative muon run stems from the fact that this would be the world's best measurement for the negative muons as there are no other experiments designed in the coming decade; the Muon $g-2$ experiment at JPARC can only collect μ^+ data. Besides this, measurement of a_{μ^-} provide a whole suite of measurements for the CPT and Lorentz violation parameters, summarized in 5.1 The negative muon run will enable us to measure the direct CPT signature and will be sensitive to the b_Z parameters discussed in chapter 1

All the magnet polarities are needed to be inverted for a negative muon run; beam line, main magnet, inflector and kicker magnets must be inverted for a μ^- run. This can be done in ~ 1 month.

The Fermilab experiment will perfom the first search for annual variation in R_μ; this advantage comes from the fact that the Fermilab experiment runs for a longer duration compared to three month running period of the BNL experiment over a year.

A recent work by Janish and Ramani [57] suggests that the $g-2$ experiment can be repurposed to probe ultralight dark matter signals that couple to muons. Various signatures of dark matter perturbations can be probed by studying the effects on the precession frequency. The nature of the perturbation will depend on the dark matter candidate that we are looking at. The spectral analysis techniques used so far for the sidereal search can be applied for the ultralight dark matter search as well; in this case the frequency of DM signal will depend on the mass of the DM we are looking for. The dark matter mass in general spans over 90 order of magnitude. So, in order to search for a potential ultralight DM signal we will need to consider statistical methods such as, look else where effect, widely used in Higgs analysis.

LIST OF REFERENCES

[1] P. Dirac, *The quantum theory of the electron* (Royal Society of London Series A, 1928).

[2] M. Schwartz, *Quantum Field Theory and the Standard Model* (Cambridge University Press, 2014).

[3] J. Schwinger, On quantum-electrodynamics and the magnetic moment of the electron, Phys. Rev. Lett. **109**, 207202 (1948).

[4] H. M. Foley and P. Kusch, On the intrinsic moment of the electron, Phys. Rev. **73**, 412–412 (1948).

[5] P. Kusch and H. M. Foley, The magnetic moment of the electron, Phys. Rev. **74**, 250–263 (1948).

[6] T. Aoyama, N. Asmussen, M. Benayoun, J. Bijnens, T. Blum, M. Bruno, I. Caprini, C. Carloni Calame, M. Cè, G. Colangelo, and et al., The anomalous magnetic moment of the muon in the standard model, Physics Reports **887**, 1–166 (2020).

[7] T. Aoyama, M. Hayakawa, T. Kinoshita, and M. Nio, Complete tenth-order qed contribution to the muon $g-2$, Phys. Rev. Lett. **109**, 111808 (2012).

[8] T. Aoyama, T. Kinoshita, and M. Nio, Revised and improved value of the qed tenth-order electron anomalous magnetic moment, Physical Review D **97**, 10.1103/physrevd.97.036001 (2018).

[9] T. Ishikawa, N. Nakazawa, and Y. Yasui, Numerical calculation of the full two-loop electroweak corrections to muon $(g-2)$, Phys. Rev. D **99**, 073004 (2019).

[10] M. Davier, A. Hoecker, B. Malaescu, and Z. Zhang, Reevaluation of the hadronic vacuum polarisation contributions to the Standard Model predictions of the muon g-2 and {α (m_Z$\hat{2}$)} using newest hadronic cross-section data, European Physical Journal C **77**, 827 (2017), arXiv:1706.09436 [hep-ph] .

[11] M. Davier, A. Hoecker, B. Malaescu, and Z. Zhang, A new evaluation of the hadronic vacuum polarisation contributions to the muon anomalous magnetic moment and to α ($m_Z{}^2$), European Physical Journal C **80**, 241 (2020), arXiv:1908.00921 [hep-ph] .

[12] T. Blum, P. A. Boyle, V. Gülpers, T. Izubuchi, L. Jin, C. Jung, A. Jüttner, C. Lehner, A. Portelli, and J. T. Tsang (RBC and UKQCD Collaborations), Calculation of the hadronic vacuum polarization contribution to the muon anomalous magnetic moment, Phys. Rev. Lett. **121**, 022003 (2018).

[13] A. Keshavarzi, D. Nomura, and T. Teubner, $g-2$ of charged leptons, $\alpha(M_Z^2)$, and the hyperfine splitting of muonium, Phys. Rev. D **101**, 014029 (2020).

[14] A. Keshavarzi, D. Nomura, and T. Teubner, Muon $g-2$ and $\alpha(M_Z^2)$: A new data-based analysis, Phys. Rev. D **97**, 114025 (2018).

[15] J. Prades, E. de Rafael, and A. Vainshtein, The hadronic light-by-light scattering contribution to the muon and electron anomalous magnetic moments, Advanced Series on Directions in High Energy Physics , 303–317 (2009).

[16] M. Hoferichter, B.-L. Hoid, B. Kubis, S. Leupold, and S. P. Schneider, Pion-pole contribution to hadronic light-by-light scattering in the anomalous magnetic moment of the muon, Phys. Rev. Lett. **121**, 112002 (2018).

[17] P. Masjuan and P. Sanchez-Puertas, Pseudoscalar-pole contribution to the $(g_\mu - 2)$: A rational approach, Phys. Rev. D **95**, 054026 (2017).

[18] M. Hoferichter, B.-L. Hoid, B. Kubis, S. Leupold, and S. P. Schneider, Dispersion relation for hadronic light-by-light scattering: pion pole, Journal of High Energy Physics **2018**, 10.1007/jhep10(2018)141 (2018).

[19] G. Colangelo, M. Hoferichter, M. Procura, and P. Stoffer, Rescattering effects in the hadronic-light-by-light contribution to the anomalous magnetic moment of the muon, Phys. Rev. Lett. **118**, 232001 (2017).

[20] G. Colangelo, F. Hagelstein, M. Hoferichter, L. Laub, and P. Stoffer, Short-distance constraints on hadronic light-by-light scattering in the anomalous magnetic moment of the muon, Physical Review D **101**, 10.1103/physrevd.101.051501 (2020).

[21] T. Blum, N. Christ, M. Hayakawa, T. Izubuchi, L. Jin, C. Jung, and C. Lehner, Hadronic light-by-light scattering contribution to the muon anomalous magnetic moment from lattice qcd, Physical Review Letters **124**, 10.1103/physrevlett.124.132002 (2020).

[22] N. Asmussen, E.-H. Chao, A. Gérardin, J. R. Green, R. J. Hudspith, H. B. Meyer, and A. Nyffeler, Developments in the position-space approach to the hlbl contribution to the muon $g-2$ on the lattice (2019), arXiv:1911.05573 [hep-lat] .

[23] B. e. a. Abi (Muon $g-2$ Collaboration), Measurement of the positive muon anomalous magnetic moment to 0.46 ppm, Phys. Rev. Lett. **126**, 141801 (2021).

[24] K. Hagiwara, K. Ma, and S. Mukhopadhyay, Closing in on the chargino contribution to the muon $g-2$ in the mssm: Current lhc constraints, Phys. Rev. D **97**, 055035 (2018).

[25] D. Hanneke, S. Fogwell, and G. Gabrielse, New measurement of the electron magnetic moment and the fine structure constant, Phys. Rev. Lett. **100**, 120801 (2008).

[26] M. e. a. Abe, A new approach for measuring the muon anomalous magnetic moment and electric dipole moment, Progress of Theoretical and Experimental Physics **2019**, 10.1093/ptep/ptz030 (2019), 053C02, https://academic.oup.com/ptep/article-pdf/2019/5/053C02/28746337/ptz030.pdf .

[27] E. C. Leskow, G. D'Ambrosio, A. Crivellin, and D. Müller, $(g-2)_\mu$, lepton flavor violation, and z decays with leptoquarks: Correlations and future prospects, Phys. Rev. D **95**, 055018 (2017).

[28] A. Crivellin, M. Hoferichter, and P. Schmidt-Wellenburg, Combined explanations of $(g-2)_{\mu,e}$ and implications for a large muon edm, Phys. Rev. D **98**, 113002 (2018).

[29] A. Czarnecki and W. J. Marciano, Muon anomalous magnetic moment: A harbinger for "new physics", Phys. Rev. D **64**, 013014 (2001).

[30] M. A. et al., Dark photon search in the mass range between 1.5 and 3.4 gev/c2, Physics Letters B **774**, 252–257 (2017).

[31] A. H. Gomes, V. A. Kostelecký, and A. J. Vargas, Laboratory tests of lorentz andcptsymmetry with muons, Physical Review D **90**, 10.1103/physrevd.90.076009 (2014).

[32] R. Bluhm, V. A. Kostelecký, and C. D. Lane, Cptand lorentz tests with muons, Physical Review Letters **84**, 1098–1101 (2000).

[33] V. A. Kostelecký and N. Russell, Data tables for lorentz andcptviolation, Reviews of Modern Physics **83**, 11–31 (2011).

[34] V. A. Kostelecký and M. Mewes, Fermions with lorentz-violating operators of arbitrary dimension, Physical Review D **88**, 10.1103/physrevd.88.096006 (2013).

[35] R. Bluhm, V. A. Kostelecký, and C. D. Lane, *CPT* and lorentz tests with muons, Phys. Rev. Lett. **84**, 1098–1101 (2000).

[36] J. G. et al., Muon (g-2) technical design report (2018), arXiv:1501.06858 [physics.ins-det] .

[37] J. D. Jackson, *Classical electrodynamics*, 3rd ed. (Wiley, New York, NY, 1999).

[38] D. Hanneke, S. Fogwell Hoogerheide, and G. Gabrielse, Cavity control of a single-electron quantum cyclotron: Measuring the electron magnetic moment, Phys. Rev. A **83**, 052122 (2011).

[39] W. D. Phillips, W. E. Cooke, and D. Kleppner, Magnetic moment of the proton in h2o in bohr magnetons, Metrologia **13**, 179–195 (1977).

[40] P. J. Mohr, D. B. Newell, and B. N. Taylor, Codata recommended values of the fundamental physical constants: 2014, Rev. Mod. Phys. **88**, 035009 (2016).

[41] W. Liu, M. G. Boshier, S. Dhawan, O. van Dyck, P. Egan, X. Fei, M. Grosse Perdekamp, V. W. Hughes, M. Janousch, K. Jungmann, D. Kawall, F. G. Mariam, C. Pillai, R. Prigl, G. zu Putlitz, I. Reinhard, W. Schwarz, P. A. Thompson, and K. A. Woodle, High precision measurements of the ground state hyperfine structure interval of muonium and of the muon magnetic moment, Phys. Rev. Lett. **82**, 711–714 (1999).

[42] D. Stratakis, M. E. Convery, C. Johnstone, J. Johnstone, J. P. Morgan, D. Still, J. D. Crnkovic, V. Tishchenko, W. M. Morse, and M. J. Syphers, Accelerator performance analysis of the fermilab muon campus, Phys. Rev. Accel. Beams **20**, 111003 (2017).

[43] T. e. a. Albahri (The Muon $g-2$ Collaboration), Magnetic-field measurement and analysis for the muon $g-2$ experiment at fermilab, Phys. Rev. A **103**, 042208 (2021).

[44] B. MacCoy, Ibms update, muon $g-2$; docdb 10944.

[45] F. Gray, Fiber harp beam monitor, muon $g-2$; docdb 8366.

[46] J. K. et al., Design and performance of SiPM-based readout of PbF2 crystals for high-rate, precision timing applications, Journal of Instrumentation **12** (01), P01009–P01009.

[47] A. F. et al., Studies of an array of pbf2 cherenkov crystals with large-area sipm readout, Nuclear Instruments and Methods in Physics Research Section A: Accelerators, Spectrometers, Detectors and Associated Equipment **783**, 12–21 (2015).

[48] R. Brun and F. Rademakers, ROOT: An object oriented data analysis framework, Nucl. Instrum. Meth. A **389**, 81–86 (1997).

[49] C. Green, J. Kowalkowski, M. Paterno, M. Fischler, L. Garren, and Q. Lu, The Art Framework, J. Phys. Conf. Ser. **396**, 022020 (2012).

[50] Eliminating pileup from the $g-2$ data;bnl $g-2$ note no. 365.

[51] Estimation of error in differential pileup subtracted data;bnl $g-2$ note no. 377.

[52] G. W. Bennett, B. Bousquet, H. N. Brown, G. Bunce, R. M. Carey, P. Cushman, G. T. Danby, P. T. Debevec, M. Deile, H. Deng, and et al., Search for lorentz andcptviolation effects in muon spin precession, Physical Review Letters **100**, 10.1103/physrevlett.100.091602 (2008).

[53] K. Labe., E989 clock system manual, muon $g-2$ docdb cornell university.

[54] J. D. Scargle, Studies in astronomical time series analysis. II. Statistical aspects of spectral analysis of unevenly spaced data., Ap. J. **263**, 835–853 (1982).

[55] Leroy, B., Fast calculation of the lomb-scargle periodogram using nonequispaced fast fourier transforms, A&A **545**, A50 (2012).

[56] C. J. Berglund, L. R. Hunter, D. Krause, Jr., E. O. Prigge, M. S. Ronfeldt, and S. K. Lamoreaux, New limits on local lorentz invariance from hg and cs magnetometers, Phys. Rev. Lett. **75**, 1879–1882 (1995).

[57] R. Janish and H. Ramani, Muon g-2 and edm experiments as muonic dark matter detectors, Physical Review D **102**, 10.1103/physrevd.102.115018 (2020).

[58] E. Parzen, Stochastic processes,holden-day, san francisco, 1962.

[59] A. Papoulis, Probability, random variables and stochastic processes,mcgraw- hill, new york, 1965.

APPENDICES

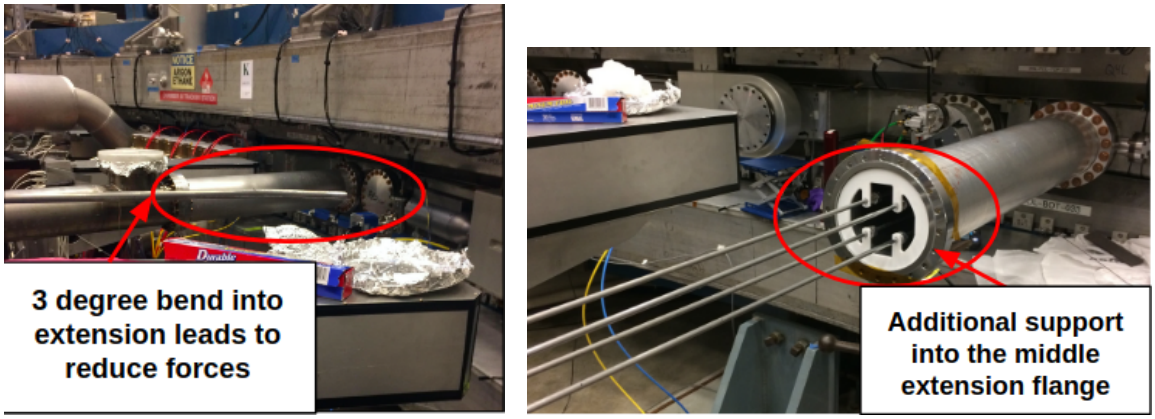
APPENDIX A

Electrostatic Quadrupole Systems

A.1 Upgrades of the EQS in Summer Shutdown 2018

We encountered many operational issues during Run-1, which caused the performance of the quadrupoles to be less than 100%. The quadrupoles suffered from high voltage breakdowns, which are also known as sparks. A spark occurs due to trapped electrons ionizing the residual gas and eventually producing an avalanche. The electron trapping occurs because of the presence of the electric and the magnetic field, causing a $E \times B$ field. The source of the free electrons is the quad plates at very high voltage themselves.

The installation of the quadrupole system at an early stage faced challenges such as, space limitations. One of the hardware deficiencies that were found to increase the spark rate, was the mechanical vibration of high voltage leads through which the quadrupole plates are connected to the high voltage resistors. More ceramic plates were added to support these leads during the shutdown period. Furthermore, small 3 deg bends were added in the end of these leads where they are connected to the quadrupole plates in order to increase spacing between them. Fig. **??** shows both the mitigation strategies discussed above. From the mirrors and cameras that were installed to capture the sparks, it was observed that one particular stand-off continuously was causing sparks; the stand-offs are used to hold the quadrupole plates in place. This particular stand-off was damaged in an accident and was replaced in-situ by uninstalling and re-installing the extension that sits outside



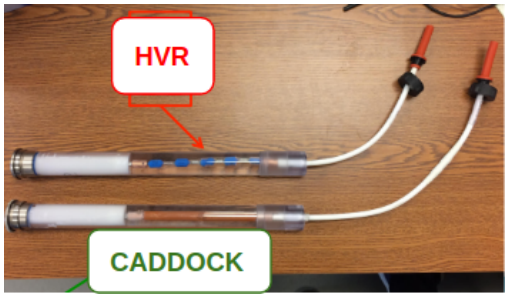
(a) Adding small bends to high voltage leads (b) Adding ceramic support to reduce mechanical vibration

Figure A.1: The first figure shows small bends introduced in the shutdown period for mitigating the high spark rates. The second figure shows another mitigation strategy of adding ceramic plates, known as "batman" to reduce vibration of long leads.

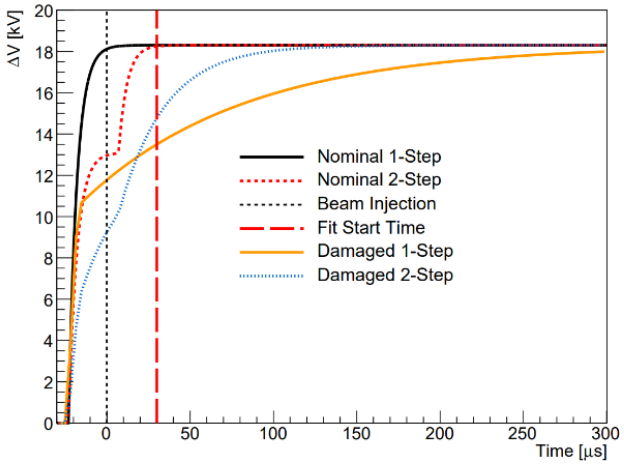
the vacuum.

One of the challenges we faced in Run-1 is that two of the thirty-two high voltage resistors were damaged. These high voltage resistors along with the quad plate capacitance sets the RC time constant to be around $5\mu s$. For the damaged ones it became $\sim 100\mu s$, which caused the muon beam to be unstable in the measurement period. The presence of these damaged resistors enhanced one of systematic effects. We used two kinds of resistors; CADDOCK and HVR. HVR resistors were found to be causing the above mentioned issues, and in the summer shutdown of 2018 we replaced all of the HVR resistors by CADDOCK. In order to make sure that the RC time constant is $\sim 5\mu s$, we check resistors as well as the capacitance of the quad plates occasionally.

In 2019, it was found that the magnetic field had a time dependent variation in the regions covered by the quads. Special NMR probes were designed to measure this effect within the storage region as the fixed probes that sit above and below the storage region would suffer from a skin depth effect from the aluminum surrounding. Models suggest that the variation in the magnetic field comes from the vibration of the quad plates and hence altering the flux within an external magnetic field. In January 2020, we measured the plate vibrations using laser reflection techniques



(a) HVR and CADDOCK high voltage resistors that were used in the quadrupole system during Run-1



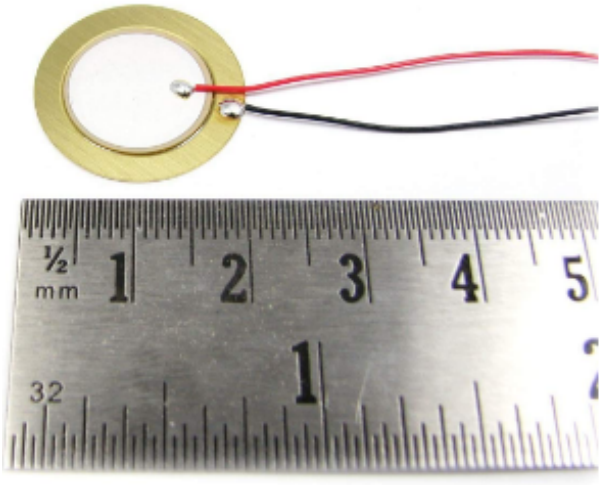
(b) The RC time constant much higher for the damaged resistors

Figure A.2: The first figure shows the two kinds of high voltage resistors that were used. The HVR resistors were found to have a resistance of $2M\Omega$ whereas the requirement was $\sim 39k\Omega$. The second plot shows that the quad plates with the damaged HVR resistors take $\sim 100\mu s$ to reach full voltage and hence affects the ω_a data

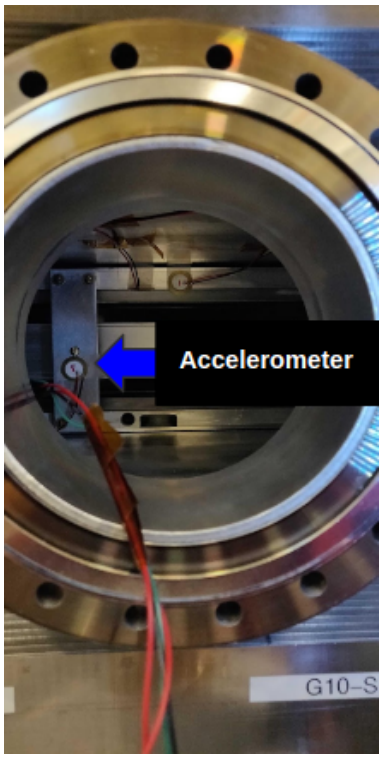
and piezoelectric accelerometers in order to determine the cause of the time dependence of the magnetic field. We attached the accelerometers to the stand-offs and places inside the storage region where laser could not reach. The accelerometer setup is shown in Fig. **??**. The quads were then pulsed with 100 Hz frequency and the vibration was recorded and analyzed by looking at the FFT. A schematic of the laser setup is shown in Fig. A.4. The laser was shot on the mirrors attached with the quad plates and the displacement of the laser was recorded in a photodiode. The results from this week long study was not conclusive enough to pin down the cause of the magnetic field variation with a huge magnitude.

A.2 RF Systems Installation and Testing for Reduction of ω_a Systematic Effects

In chapter 2 we discussed about the electrostatic quadrupole systems, which are used to confine the muon beam vertically. Before the arrival of the beam, the quadrupole plates are charged in order to maintain a beam focusing potential for the next $700\mu s$, over many turns around the storage ring. Another key component for beam storage are the kicker magnets also discussed the



(a) Accelerometer used to measure vibrations



(b) The setup when attached to a stand-off in one of the eight quad sections

Figure A.3: The piezoelectric accelerometer was used to measure the quad plate vibrations.

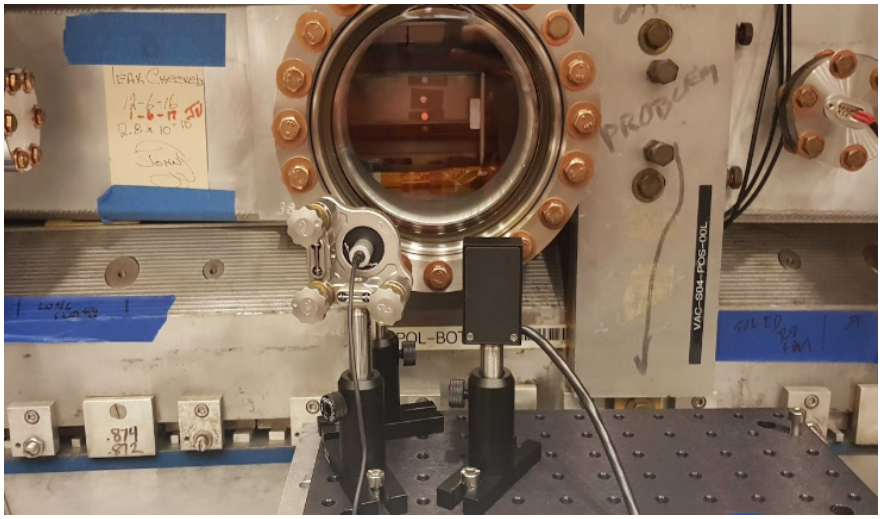


Figure A.4: The laser setup used to measure the quad plate vibrations by capturing the reflected laser from a mirror attached to the quad plates by a photo diode.

chapter 2. In Run-1, the kicker magnets were found to be underperforming, as a result the beam was not fully centered. Hence the beam dynamics effects, such as cohenrent betatron oscillation (CBO) is enhanced. An old technique using radio frequency can be used in order to manipulate the beam and hence the phase space distribution. The idea is to apply a RF electric field at the CBO frequency in the transverse direction. An oscillating dipole electric field with a phase difference of 180 deg relative to the CBO is applied in the radial direction to minimize the beam motion. The RF field will be applied to the side quadrupole plates. The RF system is installed as an extension to the existing quadrupole system, and the RF field is superposed additionally to the vertical focusing field. There has been a substantial amount of effort to install and test the system. The experiment currently does not run in RF configuration but there are plans to implement this in Run 5. The tests are ongoing in Run 4 and there will be dedicated datasets with RF configuration running. The installation and testing of the RF system was performed opportunistically in various shutdown periods since 2018. Fig. A.5 shows the schematics that was installed to the existing quadrupole system. The RF box was assembled in the experimental hall and was attached as an extension, within which resides the transformers. Fig. A.6 shows the extension box after it was assembled. The performance of the transformers were checked for each quad plate and accordingly the configurations were chosen that

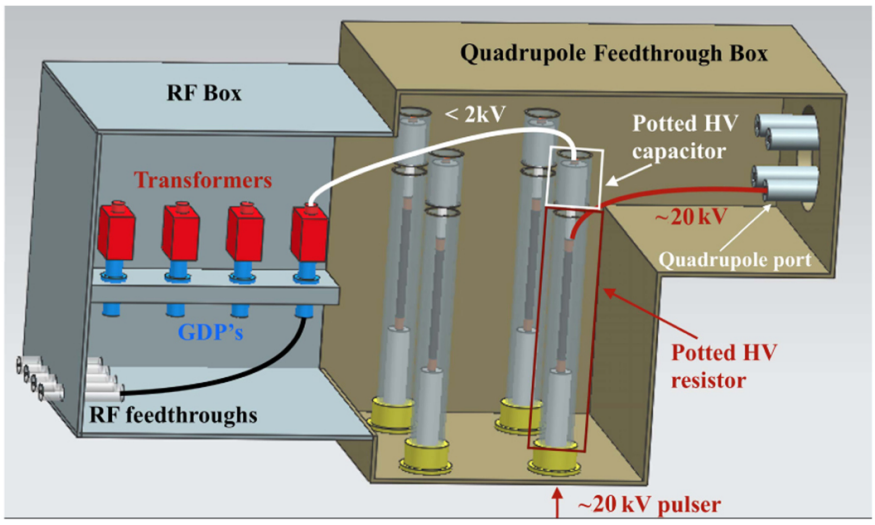


Figure A.5: Figure shows a schematic of the interface that is currently used between the RF electronics and the quadrupoles.

is now installed.



Figure A.6: RF extension boxes once assembled at MC-1



Figure A.7: Potted RF resistors that are now installed in all of the eight quadrupole systems

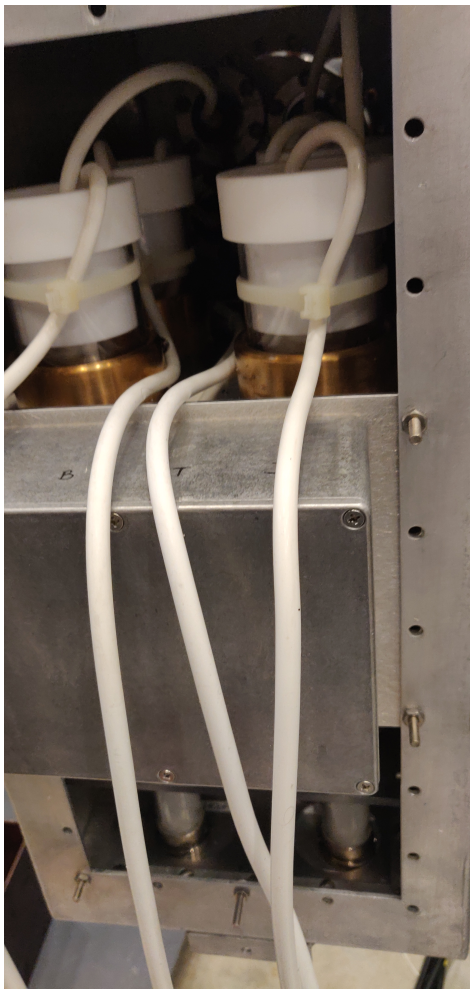


Figure A.8: Potted RF resistors after being installed in all of the eight quadrupole systems, the white cables connect the resistors to the transformers that are used to provide more power and hence more CBO reduction

APPENDIX B

Lomb-Scargle Method

As discussed in chapter 4, we used the Lomb-Scargle technique to search for CPT and Lorentz violating signals. This is a spectral analysis technique specifically designed for unevenly spaced data samples. If the data were evenly spaced then we could have used discrete fourier transform in order to go from the time domain to the frequency domain. We tried various implementations of the algorithm and the one used to generate all the results in this dissertation is based on the nFFT library as this was found to be faster than the other implementations.

B.1 Spectral Analysis Techniques

A commonly used tool in spectral analysis is calculating power spectral density using discrete fourier transforms. For a set of evenly spaced measurements $Y(t_j)$, the fourier transform can be written as

$$\mathrm{P} = \frac{1}{N_0}|\mathrm{FT}(\omega)|^2 \tag{B.1}$$

where

$$\mathrm{FT}(\omega) = \Sigma_j Y(t_j) e^{-i\omega t} \tag{B.2}$$

. The power spectral density can further be expressed in terms of sine and cosines.

$$\begin{aligned} \mathrm{P} &= \frac{1}{N_0} \mid \Sigma_j Y(t_j) e^{-i\omega t} \mid^2 \\ &= \frac{1}{N_0}\left[\left(\Sigma_j Y_j \cos(\omega t_j)\right)^2 + \left(\Sigma_j Y_j \sin(\omega t_j)^2\right)\right] \end{aligned} \tag{B.3}$$

The advantage of using the spectral power density to look for a signal in the data can be seen from eq. B.3. If there is a signal at frequency ω_0 then the power will have a maximum at ω_0 as the $Y(t_j)$ and the $e^{-i\omega t}$ will be in phase. Hence, the power spectral density directly provides the information about the frequency of a significant signal present in the data by indicating the maximum power at that frequency. The power at other frequencies will come from the sums of randomly positive and negative terms and hence not as huge as the previous contribution.

The difficulties that any spectral analysis with finite sampled data inherits are the statistical noise issues and the spectral leakage to adjacent frequencies. For a periodic signal at a particular frequency, ω_0, if the power due to the signal bleeds in to the adjacent frequencies then we refer to that as a spectral leakage problem. Leakage to adjacent frequencies occurs due to a finite size of the observational baseline. Leakage can spread to distant frequencies as well due to the sample size being finite. Smoothing techniques can be exploited to solve the leakage problem, such as multiplying by a function that is zero at the extremes of the sampling interval. The drawback of introducing a smoothing function is that the statistical properties of the algorithm is no longer straight forward as the spectral values at different frequencies will be correlated.

The statistical noise is another issue that occurs due to finite sample size. The spectral power itself is very noisy as it scales with the square of the noise present in the data.

$$Y(t_j) = Y_0 \cos(\omega_0 t + \phi) + R(t_j) \tag{B.4}$$

where $j = 1, ..., N_0$, and $R(t_j)$ represents the noise in the data. For such a dataset the power at ω_0 is given by

$$\mathrm{P}_Y(\omega_0) = N_0 \left(\frac{Y_0}{2}\right)^2 \tag{B.5}$$

and the contribution from the noise floor is given by

$$\mathrm{P}_R = \langle R^2 \rangle = \sigma_0^2 \tag{B.6}$$

Hence the signal to noise ratio (SNR) becomes

$$\frac{\mathrm{P}_Y}{\mathrm{P}_R} = N_0 \left(\frac{Y_0}{2\sigma_0} \right)^2 \tag{B.7}$$

From eq. B.7 it is evident that the SNR is proportional to the number of data points within the dataset. Although the noise level remains the same but the SNR improves with an increased sample size. These issues become less significant when the signal present in the data is strictly periodic.

B.2 Lomb-Scargle Test

For the data analysis in this dissertation, a slightly modified spectral analysis technique was used. The spectral power is given by [54]

$$P_N(\omega) \equiv \frac{1}{2\sigma^2} \left\{ \frac{[\sum_j Y_j \cos\omega(t_j - \tau)]]^2}{\sum_j \cos^2[\omega(t_j - \tau)]} + \frac{[\sum_j Y_j \sin\omega(t_j - \tau)]]^2}{\sum_j \sin^2[\omega(t_j - \tau)]} \right\} \tag{B.8}$$

The advantage of writing the spectral power in the above form is that the statistical behavior is straight-forward, and its form is expressed in such a way that one could employ least square fitting methods to obtain the power. Another attractive feature of the modified expression for the spectral power is the time translation invariance for even sampling.

B.2.1 Statistical Properties

Using eq. B.1, the spectral power can be written as

$$P_Y = \frac{A^2}{2} \left[\sum_j Y(t_j) \cos\omega t_j \right]^2 + \frac{B^2}{2} \left[\sum_j Y(t_j) \sin\omega t_j \right]^2 \tag{B.9}$$

where $A = B = \sqrt{\frac{2}{N_0}}$. Additional conditions are imposed to determine the coefficients, A and B. These conditions are imposed in such a way that the statistical properties remain widely unchanged from that of the even sampling scenario. Consider the case where Y consists of pure gaussian noise,

with standard deviation σ_0. Now if we define $C(\omega)$ and $S(\omega)$ as [58]

$$C(\omega) = A \sum_j Y(t_j) \cos(\omega t_j) \tag{B.10}$$

and

$$S(\omega) = A \sum_j Y(t_j) \sin(\omega t_j) \tag{B.11}$$

Hence, P_Y can be written as

$$P_Y = \frac{1}{2} \left[C^2(\omega) + S^2(\omega) \right] \tag{B.12}$$

where P_Y is expressed in terms of a sum of two normal distributions of random variables. We consider the sum of two random variables in order to study the statistical property of P_Y.

Consider two random variables, X and Y with zero mean and standard deviations to be σ_1 and σ_2 respectively. Then another random variable $Z = X^2 + Y^2$ will have a distribution given by [59]

$$P_z(z) = \frac{e^{-\frac{z}{2\sigma_2^2}}}{2\sigma_1\sigma_2} G[\frac{z}{4}(\frac{1}{\sigma_1^2} - \frac{1}{\sigma_2^2})] \tag{B.13}$$

where $G(z)$ is represented in terms of modified Bessel functions, $G(z) = e^{-z} I_0(z)$. For a special case of $\sigma_1 = \sigma_2$, the expression becomes

$$P_z(z) = \frac{1}{2\sigma^2} e^{-\frac{z}{2\sigma^2}} \tag{B.14}$$

Now revisiting Eq. B.12, the expression for the spectral power becomes [59]

$$P_Y(\omega) = \frac{1}{2} \left[\frac{(\sum_j Y_j \cos \omega t_j)^2}{\sum_j \cos^2 \omega t_j} + \frac{(\sum_j Y_j \sin \omega t_j)^2}{\sum_j \sin^2 \omega t_j} \right] \tag{B.15}$$

and has an exponential distribution.

The probability distribution function for Z in $z < Z < z + dz$ can be written as

$$p_Z(Z) = e^{-z}dz \tag{B.16}$$

The corresponding cumulative distribution function (CDF) has the form

$$F_Z(z) = 1 - e^{-z} \tag{B.17}$$

B.2.2 Independent Frequencies

The freuquency range used in this dissertation for the Lomb-Scargle test is $[0, 5F_c]$, where F_c is the average nyquist frequency. Now, not all of the frequencies within this range are independent. The number of independent frequencies depends on the frequency grid, the number of data points within the observational baseline and the spacing of the data points. The number of independent frequencies can be determined by performing a Monte carlo simulation to generate artificial data using the real data information, and find the maximum spectral power for each simulated dataset. The distribution of the maximum spectral power basically represents the probability distribution funtion of the underlying random variable. So, by fitting the distribution to $Pr(Z_{max} > z) = 1 - (1 - e^{-z})^N$ one can determine the number of independent frequencies that then can be used for calculating the confidence level.

VITA

Meghna Bhattacharya

Education

University of Mississippi

Ph.D. in Physics *August 2016 - Present*

Advisor: Prof. Breese Quinn

Thesis: Search for CPT and Lorentz Violation effects in the Muon g-2 Experiment at Fermilab

Indian Institute of Technology, Madras, India *June 2016*

M.Sc in Physics

Thesis: Reconstruction of muons using INO (India-based Neutrino Observatory) ICAL Detector.

Supervisor: Dr Prafulla Behera

St. Xavier's College, Kolkata, India *May 2014*

B.Sc in Physics